Predictive Modeling of Architected Solids across Scales

Thesis by
Ziran Zhou

In Partial Fulfillment of the Requirements for the
Degree of
Doctorate of Philosophy in Mechanical Engineering

CALIFORNIA INSTITUTE OF TECHNOLOGY
Pasadena, California

2025
Defended January 21, 2025

Ziran Zhou
ORCID: 0009-0008-9327-3505

ACKNOWLEDGEMENTS

First, I want to express my appreciation to my advisor, Prof. José Andrade, for his insightful guidance, inspiring mentorship, and exemplary leadership. His philosophy of life has profoundly shaped my approach to research and my perspective on navigating life's challenges.

I am also very thankful to my committee, Prof. Xiaojing Fu, Prof. Chiara Daraio, and Prof. Guruswami Ravichandran. I have had the privilege of collaborating with all of them and deeply appreciate their invaluable advice, insightful feedback, and unwavering support throughout my projects.

Next, I am deeply thankful for the wonderful members of the COSYMO and Fu groups. I want to thank Dr. Jacinto Ulloa for his invaluable advice and guidance on projects, as well as for being a supportive friend throughout my journey. To Dr. Robert Buarque de Macedo, Dr. Rigoberto Moncada, and Dr. John Harmon, I am grateful for the vital discussions and code exchanges that greatly enriched my work. I'd like to thank current and former members of the groups, Prof. Bo Zhou, Dr. Siavash Monfrad, Dr. Anna Gorgogianni, Dr. Liuchi Li, and Dr. Adrian Moure for their inspiring project discussions. Finally, I want to acknowledge the rest of the Fu group for their continued support and camaraderie.

I would also like to express my sincere thanks to my undergraduate advisors, Dr. Michael Cai Wang and Dr. SungWoo Nam. Their guidance was instrumental in shaping my academic path, and I am especially grateful to Dr. Wang for his unwavering support and mentorship during the challenging and formative years of my undergraduate journey.

Lastly, I'd like to express my heartfelt gratitude to my family and friends who have supported me throughout my studies. To my friends at Caltech, thank you for the shared late-night homework sessions, qualifying exam preparations, and unforgettable adventures. I'd like to acknowledge my cats, Beibei and Cece, for their companionship. Most importantly, I am deeply grateful to my family for their unwavering support throughout my journey in the U.S.. Without them, none of this would have been possible.

ABSTRACT

Architected solids, comprising discrete or continuous materials and structures, are purposefully designed to achieve specific functional objectives, such as tailored mechanical properties or enhanced performance. The integration of architectural features and material science has revolutionized design and functionality across multiple length scales. However, experimental exploration of architected solids is often constrained by physical, financial, or technological limitations. To address these challenges, this study leverages computational models as powerful tools for validating and probing the behaviors of architected solids through three distinct case studies spanning different length scales.

The first case study focuses on capturing the seismic performance of multiblock concrete structures at CERN for radiation shielding. The Level Set Discrete Element Method (LS-DEM), combined with Monte Carlo sampling of material properties, is employed to benchmark the displacement profiles of four concrete configurations against experimental data. In the second case study, a bonded LS-DEM model is utilized to investigate the bending response of a woven topological interlocking material (TIM). After validation against experimental results, the model is employed to explore how friction and contact area influence the bending resistance of the TIM system. The third case study introduces a 3D translational tensegrity structure modeled using the Finite Element Method (FEM). This model captures the deformation responses of single cells, monolayers, and multicellular spheroids under various loading conditions. Additionally, a data-driven (DD) framework with multiscale analysis is implemented, offering accurate results with enhanced computational efficiency. Through these three case studies, this research illustrates the evolution of computational models from tools for validating known behaviors to frameworks for exploring new phenomena.

PUBLISHED CONTENT AND CONTRIBUTIONS

(* denotes equal contribution)

[1] Z. Zhou, M. Andreini, L. Sironi, P. Lestuzzi, E. Andò, F. Dubois, D. Bolognini, F. Dacarro, and J. E. Andrade. Discrete structural systems modeling: Benchmarking of LS-DEM and LMGC90 with seismic experiments. *Journal of Engineering Mechanics*, 149(12):04023097, 2023. doi: 10.1061/JENMDT.EMENG-7036.
Z.Z participated in the conception of the project, built the numerical model, processed and analyzed the data, wrote the manuscript, and participated in the manuscript revision.

[2] T. Lu*, Z. Zhou*, P. Bordeenithikasem, N. Chung, D. F. Franco, J. E. Andrade, and C. Daraio. Role of friction and geometry in tuning the bending stiffness of topologically interlocking materials. *Extreme Mechanics Letters*, 71:102212, 2024. doi: 10.1016/j.eml.2024.102212.
Z.Z participated in the conception of the project, built the numerical model, processed and analyzed the data, wrote the manuscript, and participated in the manuscript revision.

[3] Z. Zhou, J. Ulloa, G. Ravichandran, and J. E. Andrade. Tensegrity structures and data-driven analysis for 3D cell mechanics. Submitted to: *Computer Methods in Applied Mechanics and Engineering*.
Z.Z participated in the conception of the project, built the numerical model, processed and analyzed the data, and wrote the manuscript.

TABLE OF CONTENTS

LIST OF ILLUSTRATIONS

LIST OF TABLES

NOMENCLATURE

CD. Contact Dynamics.

CERN. The European Organization for Nuclear Research.

CSK. Cytoskeleton.

DD. Data-driven.

DEM. Discrete Element Method.

FEM. Finite Element Method.

LMGC90. Logiciel de Mécanique Gérant le Contact.

LS-DEM. Level Set Discrete Element Method.

MAGR. Monumental Articulated Ancient Greek and Roman.

MCS. Multicellular spheroid.

NN. Neural network.

NSCD. Non Smooth Contact Dynamics.

RVE. Representative volume element.

TI. Topological interlocking.

TIM. Topological interlocking material.

VAE. Variational Autoencoder.

Chapter 1

INTRODUCTION

1.1 Research Objective

Architected solids are collections of materials or structures that are purposefully designed and constructed to achieve specific functional objectives, such as tailored mechanical properties or enhanced performances. The integration of architectural features and material science has revolutionized design and functionality across multiple length scales [51], from large-scale deployable structures [92, 164], high-performance reinforcement materials [113, 115], to mechanical/electrochemical actuators [65, 174] and nanophotonic devices [71, 109]. However, despite their vast potential, designing, understanding and optimizing architected solids across varying length scales present significant challenges, especially when experimental exploration is often constrained by physical, financial, or technological limitations.

By definition, the design process requires iterative exploration of possibilities to refine and optimize outcomes. However, physical experimentation for iteration is often prohibitively costly in terms of time, money, and labor. Computational modeling offers a compelling alternative, providing significant time and financial efficiencies while uncovering critical insights that experiments alone cannot reveal. This necessitates the development of reliable computational tools that combine speed and accuracy, enabling full-scale and reduced-scale models with applicable scaling laws, as well as multiscale models to comprehensively study the systems.

On the other hand, certain complex systems, such as biological structures, are too intricate to be fully understood even with advanced computational models. In these cases, engineering analogies play a crucial role. By developing appropriate models as analogs, researchers can probe and better understand the behaviors of these systems, shedding light on phenomena that would otherwise remain inaccessible.

This thesis leverages efficient computational models to predict and analyze the mechanical responses of architected solids. Specifically, the objectives of this thesis are:

- Develop and benchmark efficient computational models for architected solids at various length scales.

- Explore the role of design parameters, such as assembly configuration, constituent geometry, material property, and prestress, in determining system behaviors.
- Employ the validated computational models to explore and better understand complex systems.

1.2 Approach

We develop accurate and efficient numerical models to investigate the physics and mechanics of architected solids across three distinct case studies, each at a different length scale (Figure 1.1). The first two case studies examine discrete, contact-driven systems where component interactions dominate. We model these systems using discrete methods. The third case study focuses on pin-connected cable-truss structures, for which we employ 1D Finite Element Method (FEM) to capture their responses.

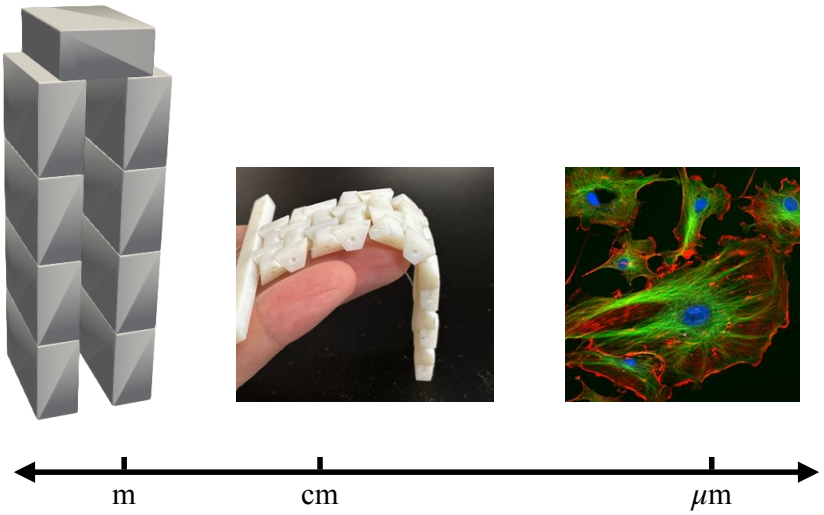

Figure 1.1: Architected structures across scales. (a) Multiblock structure at CERN [180]; (b) Woven topological interlocking materials [97]; (c) Cytoskeleton [10].

We begin this investigation at the meter scale, employing a macroscopic approach to study a discrete system governed by contact-driven behaviors. The first case study focuses on the seismic performance of meter-scale multiblock structures. The European Organization for Nuclear Research (CERN) uses concrete multiblock structures for radiation shielding from particle colliders. Due to the impracticality of testing every possible structural configuration on a shake table, especially given that

some of these structures span hundreds of meters, we instead conduct a numerical study benchmarked by shake table tests on four simplified structures. The resulting kinematic profiles from these tests are used to validate computational models, with the goal of using these models to predict the seismic response of larger, more complex block assemblies that are beyond the reach of experimental testing. Due to the discrete nature of the multiblock structures, we employ and compare two different discrete models to capture the contact-driven behaviors of the blocks. The first model is the Level Set Discrete Element Method (LS-DEM), which is a variant of the traditional Discrete Element Method (DEM) that accounts for arbitrary block shapes. The second model is the Logiciel de Mécanique Gérant le Contact (LMGC90), which uses nonsmooth implicit contact scheme. Theories of the two models are thoroughly explained and compared, followed by model calibration and benchmark against the kinematic profile obtained in the shake table tests using material properties prepared by Monte Carlo sampling.

Next, we transition from a fully discrete system to a partially connected discrete system at the centimeter scale. The second case study focuses on the bending response of centimeter-scale topological interlocking materials (TIMs) with adjustable external confinement. The mentioned TIM system is comprised of truncated tetrahedral particles interconnected via tensioned wires. The fabrication process involves weaving nylon wires through 3D printed truncated tetrahedrons that have longitudinal and latitudinal through-holes. By varying the tension applied to the wires, one can systematically control the overall bending stiffness of the TIM system. We change the surface friction and the contact angle between adjacent particles at a fixed wire tension, to study experimentally how they affect the system's bending response. We further inform experiments with LS-DEM simulations, to correlate surface friction and contact area with the system's bending modulus.

The tensile wires and compressive blocks in the TIM system are reminiscent of the tension-compression interactions in the tensegrity structure. In the third case study, we further downscale the application, focusing on the tensegrity structure and its role in modeling micrometer-scale cell mechanics. The cytoskeleton (CSK) plays an important role in many cell functions. Given the similarities between the mechanical behavior of tensegrity structures and the CSK, many studies have proposed different tensegrity-based models for simulating cell mechanics. However, the low symmetry of most tensegrity units has hindered the analysis of realistic 3D structures. As a result, tensegrity-based modeling in cell mechanics has been mainly focused on

single cells or monolayers. In this study, we propose a 3D tensegrity model based on FEM for simulating 3D cell mechanics. We use the proposed model to capture the responses of a single cell in indentation test, a monolayer in stretch test, and a multicellular spheroid (MCS) under osmotic pressure. Furthermore, we implement a multiscale data-driven (DD) framework to optimize the computation.

In these three case studies, efficient computational models are developed and validated against experiments, yet their roles differ across scales. In the first two case studies, computational models complement experiments by extrapolating behaviors to other configurations or constituent designs within the same physical context. In the third case study, the model goes beyond complementing experiments — it serves as an exploratory tool, bridging the gap between observable experimental results and the underlying, unobservable mechanics.

Through these case studies, our focus shifts from benchmarking computational models against experimental results, to bridging micro-scale mechanics to macro-scale responses, and ultimately, to using models as biophysical analogies to investigate and understand the complex behaviors in biological systems. This shift mirrors a progression in both physical scale, from meter-scale multiblock structures to micrometer-scale cellular systems, and conceptual focus, from validation of known behaviors to exploration of new phenomenon.

1.3 Thesis Structure

This thesis is organized as follows:

- Chapter 2 reviews the background information relevant to the mentioned topics of architected solids and their previous modeling efforts, followed by a general overview of the numerical method used in each case study.
- Chapter 3 investigates the seismic response of multiblock structures at CERN, through calibrating and benchmarking LS-DEM and LMGC90 using experiment data obtained from four specific concrete block structures. Theories of the two models are first compared. A review of experiments is conducted. Random material properties are generated using Monte Carlo sampling. Finally, two models are calibrated and benchmarked, followed by a discussion of principle results and the significance of this benchmark study.
- Chapter 4 explores the mechanics of a specific TIM design made of truncated tetrahedral particles connected by tensioned nylon wires. Experiments are

complemented by LS-DEM simulations, which help identify how surface friction and contact area affect the overall bending modulus.

- Chapter 5 develops a 3D tensegrity structure to study the mechanics of the CSK. The modeling framework is first presented. The model is then used to simulate cell responses in various loading conditions. Finally, a multiscale data-driven framework is implemented for simulations at small-deformation scale to address computational efficiency.

- Chapter 6 concludes this thesis and provides a future outlook.

Chapter 2

BACKGROUND

We categorize the three topics of architected solids into two groups: discrete contact-driven systems and pin-connected cable-truss systems. Within each category, we first provide a general overview of the topics and their previous modeling approaches. We then introduce our modeling framework along with the necessary background review.

2.1 Discrete Contact-Driven Systems

Rigid Body Structures

Thousands of years ago, ancient Greeks and Romans constructed structures made of stone, brick and concrete for civil, political and religious purposes. Some of these structures are composed of rigid members without mortar, exhibiting exceptional engineering performance such that they remain standing today [145]. In recent years, the idea of rigid bodies standing upright with only gravity and friction has found new applications in modern engineering, such as gravity energy storage [3] and radiation shielding in physics laboratories [139].

In energy storage applications, the concept involves constructing towers using discrete blocks to store energy as gravitational potential energy. As part of a comprehensive effort combining experimental and numerical characterization to study the seismic performance of these tower structures, researchers constructed two reduced-scale physical models and their corresponding numerical models using the Level Set Discrete Element Method (LS-DEM) [3, 53, 126]. By applying a scaling law [127], they successfully benchmarked the physical and numerical results, demonstrating the robustness of the developed scaling law and the effectiveness of rigid block-based discrete modeling in simulating the seismic response of multiblock structures.

At CERN, stacked concrete blocks are employed as shieldings to protect against radiation produced during the operation of particle accelerators. Sironi et al. [139] tested four full-scale concrete block configurations on shake tables to understand their seismic response. Their experiments provide critical kinematic profiles that inform and validate computational models, which can later be used to analyze larger, more complex block assemblies.

Various analytical models have been proposed in the literature to predict the dynamic response of individual rigid blocks or simple piles during earthquakes [4, 5, 25, 64, 91, 136, 138, 142, 147, 154]. However, these models are typically developed under simplified settings, limiting their applicability to more complex configurations. Analyzing large, complex block assemblies necessitates the use of numerical models.

There are mainly two popular methods — the continuous model where all element interfaces are smeared out in a homogeneous continuum, and the block-based discontinuous model [95, 131]. The former assumes all elements are perfectly connected as a continuous deformable body subject to appropriate constitutive laws [9, 96, 118], allowing analysis of detailed in-plane structural responses. The latter simulates the motion of each distinct block using the Finite Element Method (FEM) or Discrete Element Method (DEM) for deformable or rigid bodies accordingly [85, 111, 112, 141]. This discontinuous approach makes possible to study out-of-plane behaviors when the blocks disengage.

Topological Interlocking Materials

Segmentation into constituents with diverse shapes and morphologies enables high flexibility, adaptability, and multifunctionality [38]. Building on this concept, topological interlocking (TI) is a design strategy where specially shaped elements (blocks) are arranged such that the entire structure is stabilized by a global peripheral constraint, while local stability is achieved through kinematic constraints imposed by the shape and mutual arrangement of the neighboring elements [31, 33, 34]. Segmentation facilitates the design of hybrid materials by combining blocks made from different materials to achieve desired functionalities. TI designs also provide enhanced structural stability. The ability of individual blocks to undergo small internal movements within the limits of kinematic constraints allows for energy dissipation, thereby improving vibration resistance. Cracks that form within an individual block are arrested at its interfaces with neighboring blocks, thus confining local failures and preserving the structure's overall integrity [32]. Numerous studies have demonstrated that topological interlocking materials (TIMs) outperform their monolithic counterparts in mechanical performance, including enhanced strength and toughness [43, 78, 104], bendability [84], failure resistance [8], and sound absorption [14].

TIMs are typically constructed from two main families of building block geometries [39, 40]. The first family consists of Platonic solids (tetrahedrons, cubes,

octahedrons, etc.) and their truncated variants [33]. The second family includes osteomorphic blocks, which are non-Platonic geometries with matching concavo-convex contact surfaces [26, 32].

While some TI patterns have been identified, the design space for block geometries and their possible assemblies is effectively infinite. Structure–property relationships for TIMs remain poorly understood. This gap in knowledge makes it challenging to predict how a given TI design will perform mechanically across the vast space of possible configurations.

To address this challenge, researchers have adopted computational modeling to simulate and analyze the mechanical behavior of TIMs. FEM has been widely used to compute detailed stress and deformation fields of each element under external loads, yielding good agreement with experimental and analytical results [80, 124, 130, 172]. However, FEM modeling of TIMs with a large number of blocks can be computationally expensive [23].

An alternative approach is the DEM, which naturally accommodates the discrete, non-adhesive nature of the TI blocks [11, 12, 30]. Its extended version, LS-DEM, provides greater geometric versatility, enabling the modeling of arbitrarily shaped blocks. LS-DEM has been used to study various TIM designs and investigate their structural responses [41, 75, 170].

LS-DEM and its Variant

For the discrete, contact-driven systems in the first two case studies, we adopt element-based discrete approaches. In the first case study, we employ and compare two different discrete modeling methods, LS-DEM and LMGC90 (Logiciel de Mécanique Gérant le Contact), to simulate the seismic performance of multiblock structures. In the second case study, we use a variant of LS-DEM, the bonded LS-DEM, to study the system. For a detailed description of the LMGC90 method, readers are encouraged to refer to [29].

The Level-Set Discrete Element Method (LS-DEM) is a variant of the traditional Discrete Element Method (DEM) capable of capturing arbitrary shapes [76]. LS-DEM has been applied to similar multiblock structures as in the energy storage towers. Harmon et al. demonstrated that, with appropriate scaling of ground motion input, LS-DEM can produce accurate yet computationally efficient results when compared to reduced-scale physical models [53]. The efficiency of LS-DEM stems from its rigid body assumption, which simplifies contact and motion

calculations while maintaining accuracy.

In LS-DEM, each particle (block) is characterized by a level set function, ϕ, which represents the absolute distance from any given point to the nearest particle surface. By convention, ϕ is negative inside the particle and positive outside, with the particle surface defined by $\phi = 0$.

Each particle is also assigned a set of uniformly distributed surface nodes. Contact detection is performed by evaluating the level set value of one particle at the location of a surface node from another particle. A negative level set value indicates contact and also quantifies penetration depth. Normal forces are then computed using Hooke's law, while shear forces are calculated incrementally due to history dependence and capped via a selected friction law such as the Coulomb's friction law. The system's kinematics are updated using the Newton-Euler equations of motion within an explicit time-stepping scheme.

For multiblock structures composed of discrete concrete blocks without direct connections, LS-DEM is a well-suited approach. Its rigid body assumption enables efficient modeling, making it particularly advantageous for simulating both a large number of concrete assemblies and those with many interacting blocks. This computational efficiency is also desirable when simulating TIMs. In a previous study using a block-based FEM method, Dalaq et al. limited the number of blocks in simulations to five due to the high computational cost of larger quantities [23]. However, for the specific TIM design proposed in Chapter 4, each block has nylon wires woven through it. Since LS-DEM is inherently formulated for completely discrete elements, it requires adaptation to account for the effects of these connecting elements.

As a result, we construct a bonded LS-DEM model with springs connecting neighboring blocks, as illustrated in Figure 4.2c. The neutral positions of the springs are established once the blocks are equilibrated by the boundary forces. These springs can only sustain tensile forces, effectively mimicking the role of nylon wires in resisting block separation.

The detailed formulations of LS-DEM and its variant method are provided in Chapter 3.2 and Chapter 4.6.

2.2 Pin-Connected Cable-Truss Systems

Tensegrity Structures

The term tensegrity (tensional integrity), introduced by B. Fuller, refers to "an assembly of tension and compression components arranged in a discontinuous compression system" [48]. Tensegrity is a self-stable statically indeterminate assembly consisting of continuous tensile elements (tendons) and discontinuous compressive elements (bars). Tendons and bars are pin-connected in force equilibrium, setting the tensegrity structure in a tensile prestressed state.

Tensegrity structures are widely recognized for their deployability and tunability, making them valuable in civil engineering applications[49]. The introduction of prestress can potentially enhance the structural stiffness, enabling better load resistance with fewer materials [177]. Practical applications include tensegrity domes [44, 86, 121], tensegrity robots [13, 94, 119], and deployable structures [152, 162].

Beyond engineering, tensegrity principles have also inspired developments in bioengineering. Researchers have noted striking similarities between tensegrity structures and the CSK in cells. Ingber and others have provided extensive evidence of these similarities and proposed tensegrity-based models for cellular mechanics [17, 62, 63, 128, 167].

Traditional approaches in modeling tensegrity structures often rely on simplified assumptions, such as treating bars as linear elastic members that carry either tensile or compressive loads [140]. For large deformation static/dynamic analysis, more sophisticated approaches such as FEM-based Lagrangian [99] or co-rotational [178] formulations have been developed to address these cases. Additionally, discrete reduced-order models that explicitly account for the deformation of individual tensegrity members have been proposed as a computationally efficient alternative to FEM-based approaches [125].

1D Finite Element Analysis

To model the tensegrity structures, we adapt from the framework by Ma et al. [99]. We assume that all structural elements are axially loaded and pin-connected without rotation. Upon external loading, we assume the structure behaves quasi-statically.

The equilibrium of the structure is governed by the force balance at each node. The prestress in the structure is determined by solving a self-equilibrated force system, ensuring mechanical stability before external loads are applied.

The numerical implementation follows an incremental loading approach, where the external force is discretized into small increments. After each increment, the internal forces and nodal displacements are iteratively updated until equilibrium is reached. This iterative procedure accounts for nonlinearities arising from large deformations and geometric changes.

The detailed formulations of this approach are provided in Chapter 5.2.

Data-Driven Framework with Multiscale Analysis

If we represent a single tensegrity unit as a fundamental structural cell, simulating large-scale biological structures would require assembling millions of such units. This approach is computationally prohibitive, even when using 1D FEM. To overcome this challenge, we adopt a data-driven (DD) framework.

In the classical FEM approach, stress and strain are determined by satisfying equilibrium and compatibility equations, with constitutive laws providing a closure relation between the stress and strain. However, in the DD framework, instead of relying on an empirical closure relation, the problem is reformulated as a minimum-distance search. The algorithm identifies the material (training) data points that best satisfy the equilibrium and compatibility constraints, avoiding the need for an explicit constitutive model.

The DD framework has been successfully applied in various contexts, including dynamics [82], fracture mechanics [15], finite deformations [114], and micromorphic continua [159]. Its multiscale capabilities have been demonstrated in modeling history-dependent materials [74] and breakage mechanics [158], yielding results that closely match physics-based models. Additionally, DD methods have been used to compute the mechanical response of the human brain based on *in situ* and *in vivo* imaging data [129].

To construct the material dataset for our study, we sample representative volume elements (RVEs) of tensegrity structures. A full description of the DD framework and its implementation is provided in Chapter 5.4.

Chapter 3

DISCRETE STRUCTURAL SYSTEMS MODELING: BENCHMARKING OF LS-DEM AND LMGC90 WITH SEISMIC EXPERIMENTS

Z. Zhou, M. Andreini, L. Sironi, P. Lestuzzi, E. Andò, F. Dubois, D. Bolognini, F. Dacarro, and J. E. Andrade. Discrete structural systems modeling: Benchmarking of LS-DEM and LMGC90 with seismic experiments. *Journal of Engineering Mechanics*, 149(12):04023097, 2023. doi: 10.1061/JENMDT.EMENG-7036.

3.1 Introduction

The European Organization for Nuclear Research, abbreviated CERN, operates the world's largest particle physics lab. Their everyday operation, including the use of particle accelerators etc., produces radiation, from which personnel and high-tech equipment need to be shielded. The most usual approach is to use concrete structures of significant mass [70]. CERN uses assemblies of large independent concrete blocks that allow rapid re-configuring for different implementations. However, structures formed from those blocks do not have any joint connecting systems or other protective metal braces between blocks to resist the lateral forces that might be induced in case of earthquakes. Therefore, on top of radiation shielding, CERN needs to guarantee the structural safety of all concrete configurations.

Researches on seismic analysis of rigid bodies without connections date back to decades ago. Monumental Articulated Ancient Greek and Roman (MAGR) structures consist of members excellently fitting each other without mortar and standing upright only because of gravity and friction. For safety and restoration purposes of those MAGR structures, various researchers have provided valuable insights into the motions of single or multiple rigid bodies under ground excitation and established highly nonlinear governing equation of motions [83, 137]. However, those equations are not only derived with overly idealized assumptions, but are also limited to specific rigid body configurations and ground excitation patterns. Furthermore, the equation of motion can be made complicated considering energy dissipation happening at the impacting surfaces. Many have shown that the presence of friction may lead to different impact dynamics, as sticking and reverse slipping can happen [61, 148]. Therefore, for this study, reliable numerical models with simplified con-

tact mechanics are needed in order to assess the seismic performance of CERN's many concrete structures.

While analytical solution is undesirable, and it is impossible to bring every large complicated CERN configuration onto a shake table for seismic analysis, simple concrete configurations can be tested for benchmarking purposes against numerical models. With calibrated numerical models in hand, CERN can confidently simulate current or future concrete-block configurations with various ground excitations and material parameters to probe their seismic performance. With this purpose in mind, in 2019, CERN conducted a test campaign at Eucentre Foundation, Italy. The dynamic response of four different concrete-block configurations was investigated through seismic tests [139]. In this chapter, experimental results from the test campaign have been used to calibrate the two discrete-system-model: LS-DEM & LMGC90.

Cundall and Strack [22] introduced the 3D DEM in 1988, and since then this method has been used extensively for simulations of discrete particles. Traditionally, DEM deals with spherical shaped particles, hence making it inappropriate for applications with non-spherical particles. In 2016, Kawamoto et al. [76] introduced a variant of DEM, referred to as the Level Set Discrete Element Method (LS-DEM), and successfully pushed the boundary of the traditional DEM by making LS-DEM suitable for simulations of any arbitrary shaped particles. So far, LS-DEM has been used extensively in simulating the mechanics of granular media [72, 77, 100], metamaterials [170], and seismic performance analysis [3]. In [3], LS-DEM was used to assess the seismic stability of multiblock structures and the results were compared to shake table tests. This was the first attempt ever to use LS-DEM for seismic analysis.

Jean-Jacques Moreau introduced the Contact Dynamics (CD) method in 1984 [110]. The method uses a formulation of unilateral contact, shock laws, Coulomb's friction, inspired by Convex Analysis. These laws account roughly for the main features of contact and friction, and are relevant in multi-body collections where sophisticated laws cannot be captured exactly. This method was extended to deformable bodies by Michel Jean [66] and entitled Non Smooth Contact Dynamics (NSCD). See [29] for more advanced discussions on this method.

In this chapter, we present the benchmarking (including calibration) of the above state-of-the-art discrete-system-models, LS-DEM and LMGC90, with experiments. The structure of this chapter is as follows: First, we will explain and compare the

theories of both models. Then the test campaign conducted in Eucentre will be briefly described. Finally, results from the two calibrated models will be presented and compared with experiments, followed by discussions of similarities and differences. We show that the two models after calibration show remarkable resemblance to the experiments, indicating that both models are suitable for future simulations of large complicated concrete structures that cannot be tested on shake tables.

3.2 Model Methods and Comparison

LS-DEM

LS-DEM is a variant of the traditional DEM capable of simulating the kinematics and mechanics of a system of particles with arbitrary shapes, made possible by the usage of level set functions as a geometric basis [76]. For any random-shaped particles, a level set function, $\phi(\boldsymbol{x})$, calculates the distance, d, between an arbitrary point, $\boldsymbol{x}$, in the space to the nearest surface of the particle (Figure 3.1 left).

$$\phi(\boldsymbol{x}) = \pm d\,. \tag{3.1}$$

If this point is taken inside the particle, the level set value would be negative. Vice versa, the value would be positive. The surface of the particle can simply be reconstructed using $\phi(\boldsymbol{x}) = 0$. In this chapter, all particles are blocks of same size with a chamfer of 2 cm along the edges.

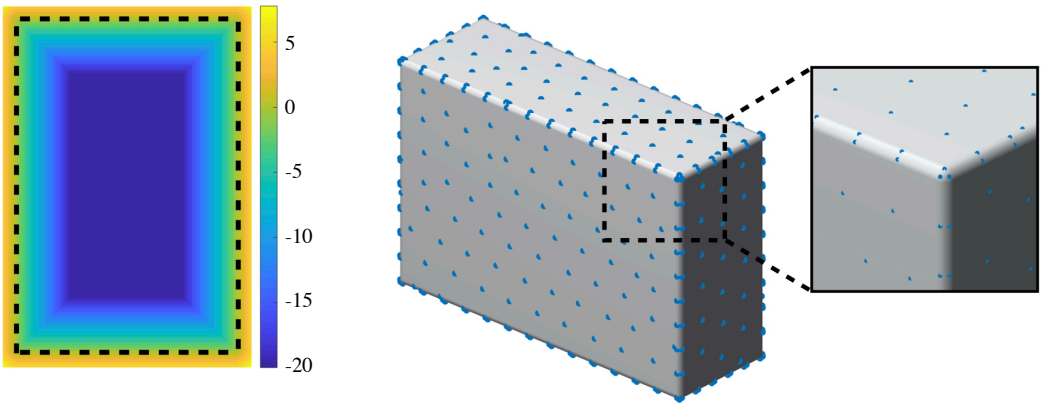

Figure 3.1: The left picture shows the level set representation of a slice of the block, with $\phi(\boldsymbol{x}) = 0$ being highlighted using a black dashed contour. The right picture shows a 3D representation of the block's $\phi(\boldsymbol{x}) = 0$ surface and the surface nodes, with a zoom on the chamfer.

Together with the level set values, a set of surface point discretization is made to

detect particle-to-particle contact (Figure 3.1 right). In this study, the level set grid had an equal spacing of 0.02 m. The surface node had a spacing of roughly 0.2 m.

All surface points $\boldsymbol{p}$ of a particle is checked against the level set values of the other particle. If a point $\boldsymbol{p}_i$ has contact, force in normal direction is subsequently calculated using

$$\boldsymbol{F}_{\mathrm{n}} = \phi(\boldsymbol{p}_i) k_{\mathrm{n}} \hat{\boldsymbol{n}} - \gamma_{\mathrm{n}} (\boldsymbol{v}^{\mathrm{rel}} \cdot \hat{\boldsymbol{n}}) \hat{\boldsymbol{n}} \quad (\text{if } \phi(\boldsymbol{p}_i) < 0) \,, \tag{3.2}$$

where k_{n} is the normal stiffness of the block, $\hat{\boldsymbol{n}}$ is the surface normal calculated at $\boldsymbol{p}_i$, γ_{n} is the critical normal damping coefficient calculated from the coefficient of restitution C_{res} at the contacting surface point [53], and $\boldsymbol{v}^{\mathrm{rel}}$ is the relative velocity of this particle with respect to the other particle.

Many researchers have proposed different formulas in applying damping to contacting points. For example, Chatzis and Smyth adopted a method in relating damping coefficient to the modulus and density of the contacting medium [16]. LS-DEM uses a formula initially proposed by Tsuji el al., incorporating coefficient of restitution directly into a critically damped mass-spring system [155] by

$$\gamma_{\mathrm{n}} = 2\sqrt{m k_{\mathrm{n}}} \frac{-\ln C_{\mathrm{res}}}{\sqrt{\pi^2 + \ln {C_{\mathrm{res}}}^2}} \,, \tag{3.3}$$

where m is the mass of the colliding object.

Due to history dependence, shear force is calculated incrementally using

$$\Delta \boldsymbol{F}_{\mathrm{s}} = k_{\mathrm{s}} \Delta t (\boldsymbol{v}^{\mathrm{rel}} - \boldsymbol{v}_{\mathrm{n}}^{\mathrm{rel}}) \,, \tag{3.4}$$

where k_{s} is the shear stiffness of the block and Δt is the integrating time step. The ultimate shear force is updated by the smaller value between the build up of incremental shearing force and the critical limit for sliding as proposed by the selection of friction law. In this version of LS-DEM, Coulomb friction law is implemented. Hence, the critical limit for sliding to happen is a fraction of the normal force. The calculation of the updated shearing force at each time step can be represented using the below equation,

$$||\boldsymbol{F}_{\mathrm{s}}^{\mathrm{updated}}|| = \min(\mu ||\boldsymbol{F}_{\mathrm{n}}||, ||\boldsymbol{F}_{\mathrm{s}}||) \,. \tag{3.5}$$

Both the shear force and the normal force contribute to the moment of the block by crossing with the relative distance with respect to the center of mass of the block, $\boldsymbol{x}_{\mathrm{cm}}$,

$$\boldsymbol{M} = (\boldsymbol{p}_i - \boldsymbol{x}_{\mathrm{cm}}) \times (\boldsymbol{F}_{\mathrm{n}} + \boldsymbol{F}_{\mathrm{s}}) \,. \tag{3.6}$$

With all forces and moments calculated, particles are then updated using Newton-Euler equations in explicit scheme with a constant time step that guarantees stability [156]. In this study, the time step of LS-DEM was 0.00001 s.

LMGC90

In Non Smooth Contact Dynamics (NSCD), the contact laws are managed as non-differentiable steep laws using a nonsmooth dynamics formalism. They are integrated with an implicit scheme, leading to a non-linear system which is solved using a Non-Linear Gauss–Seidel algorithm (NLGS) at each time step. The method uses large time steps (larger than smooth DEM), but each time step is computationally involved due to integration scheme. So in contrast to the above smooth and explicit DEM, the CD method is a nonsmooth and implicit method. Since "rigid" contacts are used, no damping has to be introduced. Note that implicit methods enable the correct computation of equilibrium states, which is not always the case with explicit methods. NSCD can also conserve, with a suitable choice of parameters, the total energy of the system in discrete time.

Concerning the modelling of structures made of regular blocks, several approaches are possible. One can consider rigid blocks with frictional contact [19], or deformable blocks with cohesive frictional contact [161], or any mix of bulk and contacting models. From a technical point of view, depending on the bulk model, the contact conditions are not treated in the same way. For rigid blocks, a common plane approach is used [22], leading to a maximum of 4 contact points (marked by red in Figure 3.2). Contact surfaces between blocks (marked by green in Figure 3.2), delimited by the four contact points, are shrunk to introduce a kind of safety coefficient. Rigid convex objects are described by a surface mesh. The contact detection algorithm is independent of the mesh as the algorithm looks for overlapping parts of surfaces. For deformable or rigid non convex objects, additional surface nodes are added to the skin mesh to detect contact with other objects in a way similar to LS-DEM. Contact conditions are verified at those surface nodes.

In this study, LMGC90 simulations were done both with rigid and deformable (elastic and visco-elastic) blocks with frictional contact and no restitution. The mesh size was 0.2 m. The time step chosen was 0.001 s.

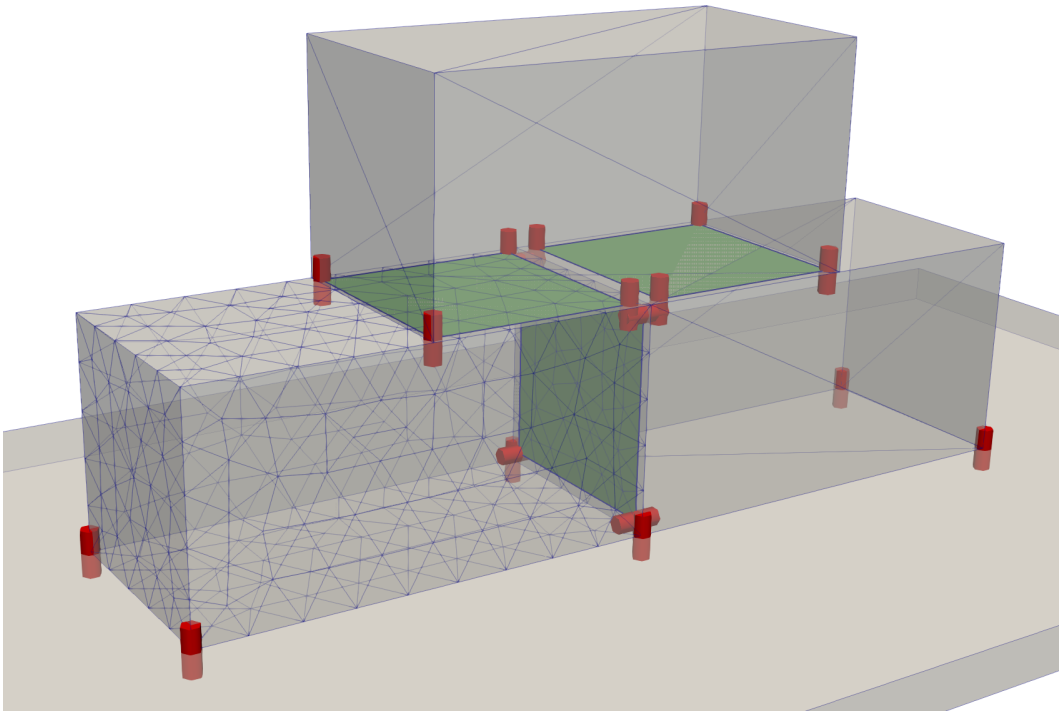

Figure 3.2: Stack of 3 polyhedra on a rigid foundation. Contact surfaces between polyhedra (denoted by green color), as delimited by contact points (denoted by red color), are shown as an example. Three polyhedra are shown in surface mesh of different density, yet the area of contact surfaces between them is the same, showing that contact detection is independent of the mesh.

Comparison

Both aforementioned models solve Newton-Euler equations. LS-DEM uses a smooth explicit time integration scheme with a fixed time step. Due to the presence of interpenetration in cases of collision, penalty terms like normal stiffness k_n and shear stiffness k_s are required. The normal force F_n is a function of the interpenetration distance d_n. When the distance is positive, normal force is zero; when the distance is negative, indicating there is a contact, F_n is a linear function of the normal stiffness k_n with respect to $|d_\mathrm{n}|$. The Coulomb's friction law adopted in LS-DEM has finite steepness. In case of static friction, i.e., $k_\mathrm{s}d_\mathrm{s} < \mu F_\mathrm{n}$, F_s is a linear function of k_s and d_s. Figure 3.3 shows a graphical representation of the calculation of F_n and F_s.

Since the current version of LS-DEM models rigid-body motions, for a fair comparison, only the dynamics of rigid bodies of LMGC90 will be discussed. LMGC90

Figure 3.3: Normal and shear contact force calculations in LS-DEM.

Figure 3.4: Comparison of normal and shear contact force calculations in rigid-body LMGC90.

uses nonsmooth implicit scheme with the equations of motions expressed in differential inclusions [28]. Unlike LS-DEM, no elastic modulus is required. The term "nonsmoothness" is an accurate representation of the infinite steepness presented by the inelastic shock law and Coulomb's law, as in Figure 3.4. When d_n is positive, the normal force F_n is zero. What's different from LS-DEM is that when $d_n \leq 0$, the Signorini condition ensures that F_n is positive or null. Similarly, the graph of Coulomb friction law exhibits an infinite steep around $d_s = 0$. Because LMGC90 uses implicit scheme, the choice of time step can be large. At each time step, NLGS is run until convergence, hence each time step can be very time consuming. As a benefit of the implicit scheme, often times energy conservation and numeric stability can be achieved without the use of damping.

3.3 Case Study: Rocking Tests

The dynamic response and the stability of four different configurations of stacked concrete blocks were investigated within an experimental campaign consisting of seismic tests. Four different specimens, whose height varied from 4.8 m to about 7.6 m, consisted of a maximum of 9 blocks were constructed (Figure 3.5). A wall of three and four stacked blocks, respectively, characterized the first and the second configuration. The third and the fourth one is consisted of two walls of four stacked blocks, with a block at the top; in the fourth specimen, a extra system of steel beams supported the top block.

The specimens were assembled on the steel platform of an unidirectional shake table at the Eucentre Foundation (Pavia, Italy). A base concrete slab, whose translation was restrained by two steel profiles fixed to the platform of the shaking table, simply supported the specimens. Steel stoppers at the base and retaining steel systems provided along the height of the specimens were used to prevent unsafe effects due to unexpected large displacements or rotations. Both the stoppers and the retaining systems were designed not to interfere with the test results.

(a) (b) (c) (d)

Figure 3.5: Different configurations of stacked blocks tested on the shake table. (a) Configuration 1: 4.8 m-height three-blocks specimen; (b) Configuration 2: 6.4 m-height four-blocks specimen; (c) Configuration 3: 7.2 m-height nine-blocks two-walls specimen; (d) Configuration 4: 7.4 m-height nine-blocks two-walls specimen with the top block supported by steel beams.

Accelerations were applied at the base of the specimens. Two different acceleration time-histories, each called Alkion and Basso Tirreno [2], were used. They were chosen because they represent an upper bound for a standard acceleration time-history representing the Geneva Area, according to the SIA norms [150]. The

acceleration time-histories and their characteristics can be found in Figure 3.6 and Table 3.1.

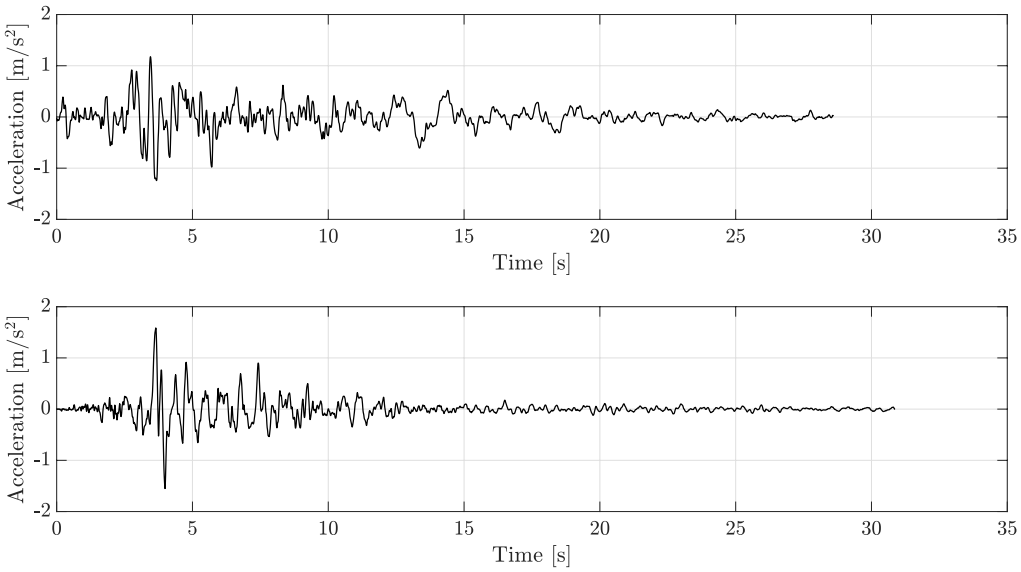

Figure 3.6: Acceleration time-histories: Alkion (top) and Basso Tirreno (bottom).

Table 3.1: Characteristics of the ground motions.

Earthquake	Date	Magnitude [Mw]	Distance [km]	PGA [m/s^2]
Alkion	Feb 25, 1981	6.3	25	1.176
Basso Tirreno	April 15, 1978	6	18	1.585

For each specimen, the first test was performed at a scaled acceleration intensity of 50%. Then a series of successive tests with acceleration amplitude increment of about 25% were performed, until a potential occurrence of structural collapse. At each intensity level, the relative position of each block was checked and, in case of large misalignment, the specimen was restored to its initial configuration. Additional low-intensity constant-amplitude tests with sinusoidal waves were performed at the beginning of the campaign or between two tests with the aim of assessing the dynamic properties and the state of damage of the specimens.

The assessment of the dynamic properties and of the seismic response of the specimens were based on the spatial components of accelerations and displacements measured at different levels along the height of the specimens. The specimens were equipped with up to 21 acceleration transducers, 4 displacement transducers and 101 retro-reflective optical markers, belonging to two different acquisition systems.

Further data regarding force, accelerations, velocities and displacements of the shaking table was obtainable from the control system. The measurement frequencies were 512 Hz and 200 Hz for accelerations and displacements, respectively. The acceleration signals were later filtered with a 50 Hz low-pass filter. An example of the layout of the instrumentation is depicted in Figures 3.7 and 3.8 for Configuration 3. For more details of the experiments, please refer to [139].

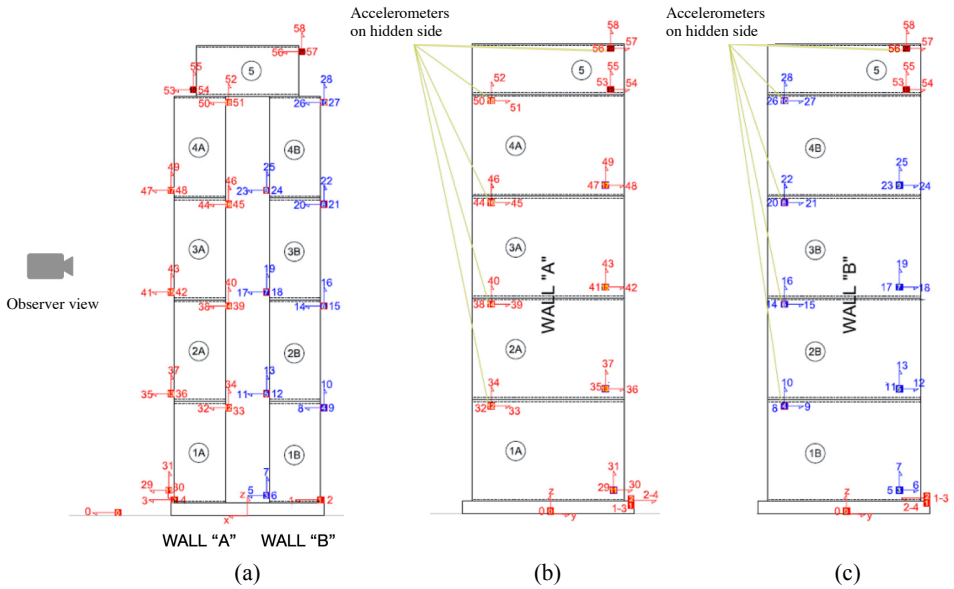

Figure 3.7: Layout of the accelerometers of Configuration 3. (a) Front view of the two walls; (b) Wall "A" from the observer view; (c) Wall "B" from the observer view.

3.4 Results and Discussion

Model Calibration

To calibrate both models with respect to experiment results of Eucentre's test campaign, mechanical properties of concrete and steel are required. While most of the distribution parameters of these properties (e.g., mean, standard deviation, or coefficient of variation) can be found in literature, concrete-to-concrete friction coefficient could not be determined due to its large variation present in literature. Therefore, a semi-probabilistic approach using Monte Carlo sampling was adopted.

With most of the distribution parameters of concrete and steel properties taken from literature [67, 68], the mean of concrete-to-concrete friction coefficient was randomly sampled from 0.3 to 0.8. Log-normal distributions were then created for each of the material properties and were later inputted into a procedure based on correlation controlled Latin Hypercube Sampling (LHS) technique, developed

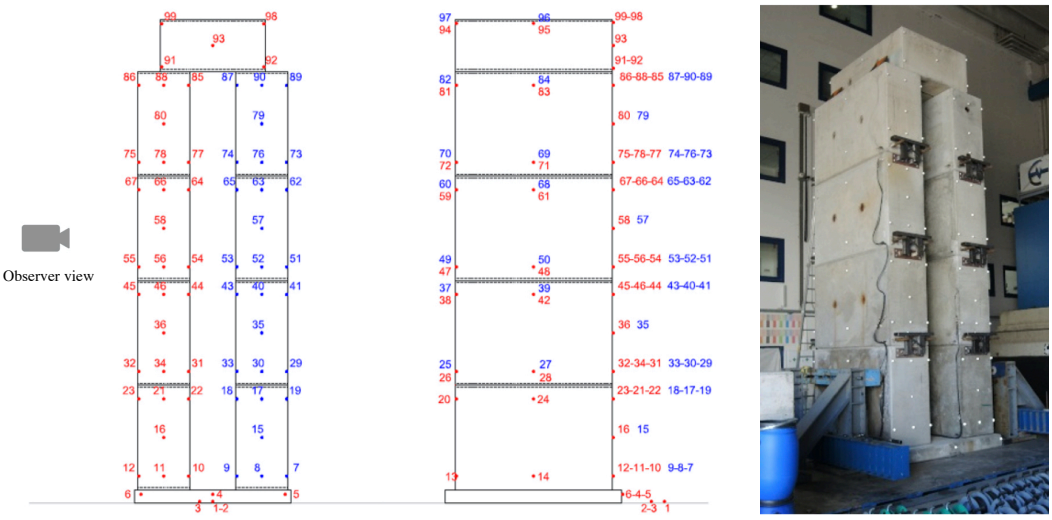

Figure 3.8: Layout of the retro-reflective markers of Configuration 3. (a) Front view of the two walls; (b) Layout from the observer view; (c) Image of the specimen taken at Eucentre.

by Vořechovský and Novák [163], to sample from multivariate distributions. This method is efficient for small sample sizes and can lead to accurate estimates of real behaviors with low variability. In total of 50 sample vectors were produced from this procedure, with each of the sample vectors assembled by sampled properties of concrete and steel (e.g., friction coefficients, density, and modulus of elasticity). Then, 50 sets of simulations (one for each sample vector) were performed in both LS-DEM and LMGC90 in order to determine whether the displacement envelope created by all samples contain the actual experiment data. This process was repeated multiple times to obtain the most optimal value of the mean of concrete-to-concrete friction coefficient. Eventually, a final set of distribution parameters was chosen to be used for future simulations for seismic risk assessment of concrete configurations at CERN.

The optimal values for the distribution parameters of concrete and steel properties are reported in Table 3.2. For each variable, the histogram of the samples obtained by the LHS technique is presented in Figure 3.9.

While variables like friction coefficient μ and density ρ are straight forward and universal, there are a couple of parameters that need to be translated or calibrated uniquely in LS-DEM. Normal stiffness k_{n} and shear stiffness k_{s} are penalty parameters unique to the DEM. Methods like the Hertzian Contact Theory directly

Table 3.2: Distribution models and parameters used in the simulations.

Variable	Distribution Model	Mean	SD	C.o.V.
Friction Concrete/Concrete [-]	Log-normal	0.75	0.075	0.1
Friction Concrete/Foundation [-]	Log-normal	0.75	0.075	0.1
Friction Steel/Concrete [-]	Log-normal	0.3	0.03	0.1
Concrete Density [kg/m3]	Log-normal	2400	96	0.04
Concrete Young's Modulus [Pa]	Log-normal	3.45E+10	5.175E+09	0.15
Concrete Viscous Modulus [Pa]	Log-normal	1.5E+08	2.25E+07	0.15
Steel Density [kg/m3]	Log-normal	7700	77	0.01
Steel Young's Modulus [Pa]	Log-normal	0.21E+12	6.3E+09	0.03
Steel Viscous Modulus [Pa]	Log-normal	0.21E+10	6.3E+07	0.03

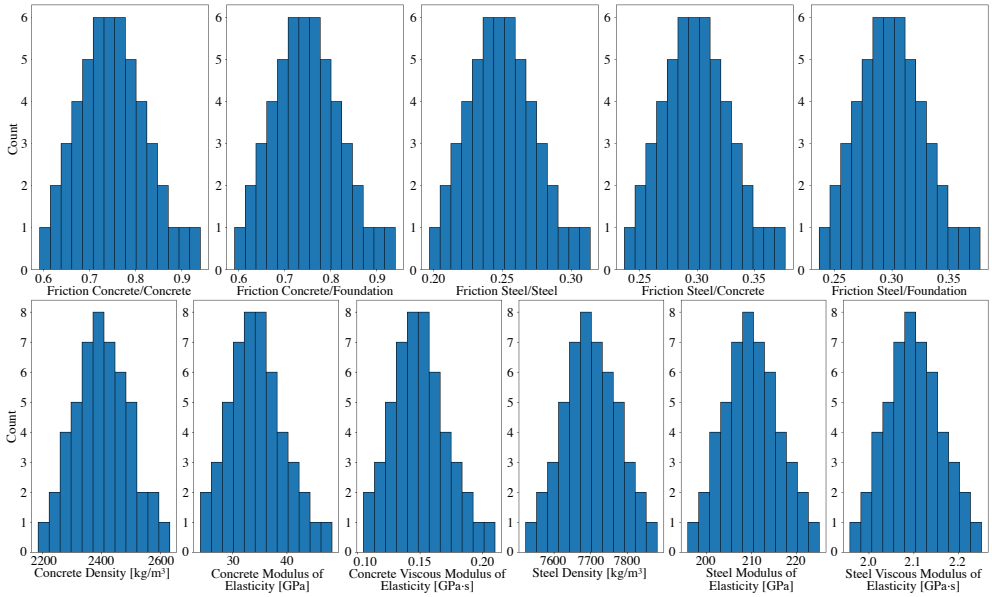

Figure 3.9: Histograms of the samples obtained by the LHS technique.

correlates the elastic modulus of a material to the stiffnesses required in the DEM. However, the Hertzian Contact model does not apply for contacts between blocks. Therefore, a different method has to be developed in order to approximate stiffness from real material properties like modulus of elasticity.

Harmon et al. [53] presented a novel way of determining k_n and k_s. In reality, when a stack of concrete block assembly is excited by ground acceleration, the motion of blocks is set off via the propagation of stress waves. There is no way to model stress waves in LS-DEM, yet delayed responses of higher blocks are observed due to the presence of contact elasticity. As a result, normal stiffness and shear stiffness can be tuned such that the speed of propagation of motion, referred to as the "effective

wave speed," in the simulation is the same as the speed of stress wave propagation in reality.

The speed of stress waves can be calculated as

$$c_{\mathrm{p}} = \sqrt{E/\rho} \tag{3.7}$$

for pressure waves and

$$c_{\mathrm{s}} = \sqrt{G/\rho} \tag{3.8}$$

for shear waves, where E is the Young's modulus of the material, G is the shear modulus and ρ is the density. To match with above speeds, a tower of stacked concrete blocks is set up in the simulation. A unit step of velocity is then given to the ground in LS-DEM in both horizontal and vertical direction, respectively. The resulted displacement of the blocks is plotted against time, as shown in Figure 3.10. The effective wave speed is calculated after all the blocks have reached a similar velocity, which is indicated by a near-identical slope in Figure 3.10. The effective wave speed can then be obtained by $\Delta h/\Delta t$.

By calculating the effective wave speed and matching it to the actual stress wave propagation speed in Eq. 3.7 and 3.8, one can approximate k_{n} and k_{s}. The resulting histograms of such parameters are shown in Figure 3.11. We see that the distributions of k_{n} and k_{s} not necessarily follow those of E and G because the effective wave speed is also affected by block mass. With heavier blocks, larger stiffness is required for the contact to overcome the inertial force and respond to the ground excitation.

Other than the variables listed in Table 3.2, LS-DEM is taking the coefficient of restitution C_{res} into the calculation of normal forces (Eq. 3.2). After tuning the model, it is found that a moderate amount of normal damping with $C_{\mathrm{res}} = 0.5$ is needed in order to compensate for the large k_{n} obtained due to the significant mass of the blocks. The coefficient of restitution adopted in this chapter is within the range reported from [53].

In order to examine both methods' abilities to capture the seismic performance of the concrete structures, tests with the largest ground accelerations were chosen among all the experiments. Displacement readings were taken from the optical marker located at the face center of the side of the base concrete slab. Velocities were then calculated from the displacements and fed into the program as ground input.

Results are shown in Figures 3.12–3.15. In these figures, the displacement time-history of mass center of the concrete block is plotted against optical readings taken

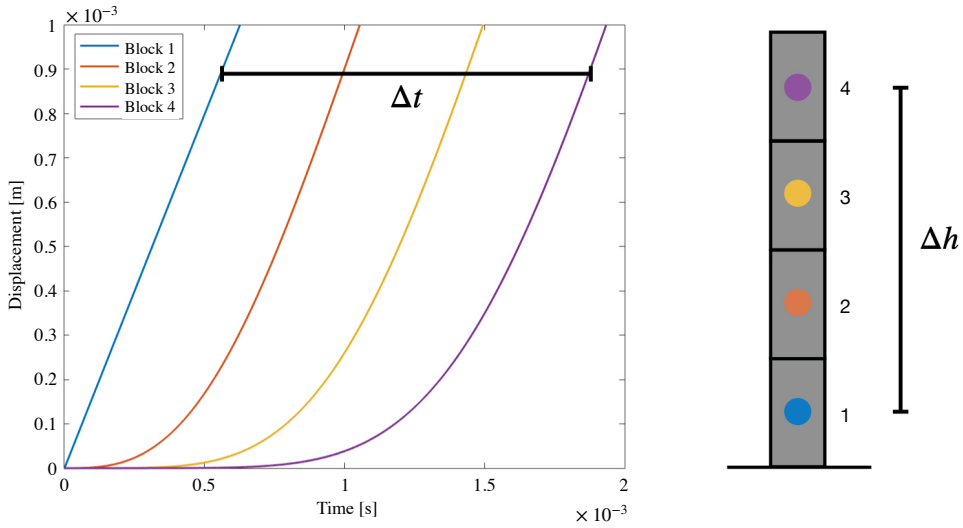

Figure 3.10: Displacement time-histories of the blocks after the unit step velocity (left) and the tower of four concrete blocks (right). After all the blocks have reached a similar velocity, the effective wave speed can then be obtained.

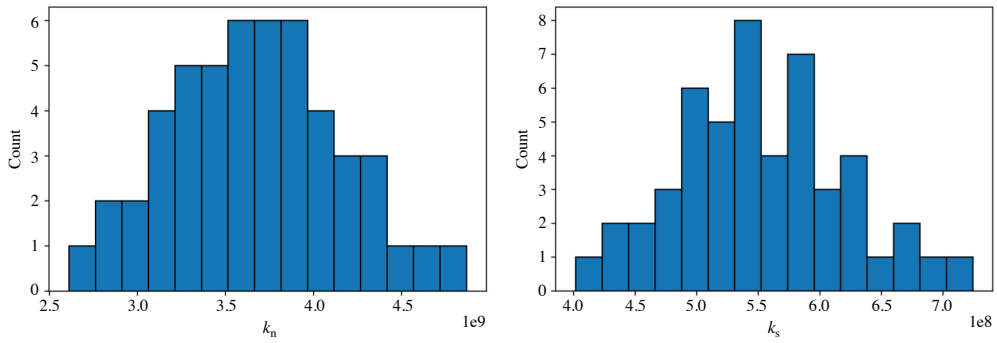

Figure 3.11: Histograms of normal stiffness k_{n} (left) and shear stiffness k_{s} (right) approximated using method described.

from the face center on the side of the same specimen. The grey shaded area is the overlapping of the lines representing the displacement time-histories of all 50 sample sets, with the red line highlighting the maximum and minimum values along the time axis. The black dashed lines indicate the actual experiment results taken from Eucentre.

LS-DEM Results

In Configurations 2, 3, and 4, the displacement envelope of the top block is thicker compared to that of Configuration 1. This is inevitable as a result of different model parameters tested. Since kinematics of higher blocks are calculated based on that of the lower ones, as the number of blocks increases, the displacement envelope naturally propagates upward and becomes thicker. Moreover, the onset of rocking or slide-rocking is related to the height-to-width ratio of the assembly [134]. Since Configuration 1 has the least number of concrete blocks and shortest height, the occurrences of rocking and/or slide-rocking is the fewest among all configurations tested. Configurations 3 and 4 are higher in levels and also are more complicated in structures, so naturally, rocking and/or slide-rocking behavior is more likely to be observed. As those dynamic events happen, the behavior of the blocks can heavily depend on parameters like friction coefficient, density and stiffnesses, thus giving explanation to thicker envelopes for Configurations 2, 3, and 4. Similarly, as seen in the LS-DEM result from Figure 3.15, the displacement envelope is thicker for the top block compared to that of Configuration 3, potentially due to the inclusion of four supporting steel beams.

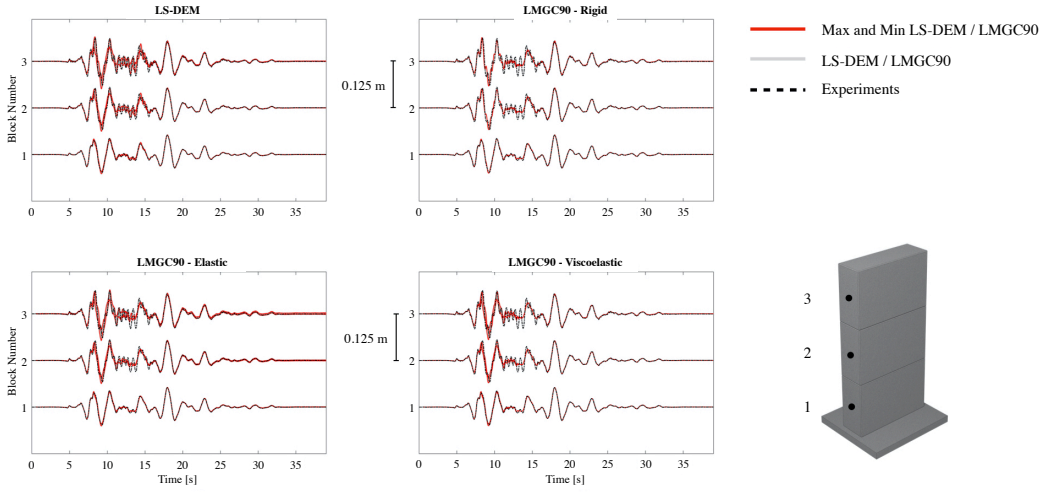

Figure 3.12: Displacement time-histories for Configuration 1.

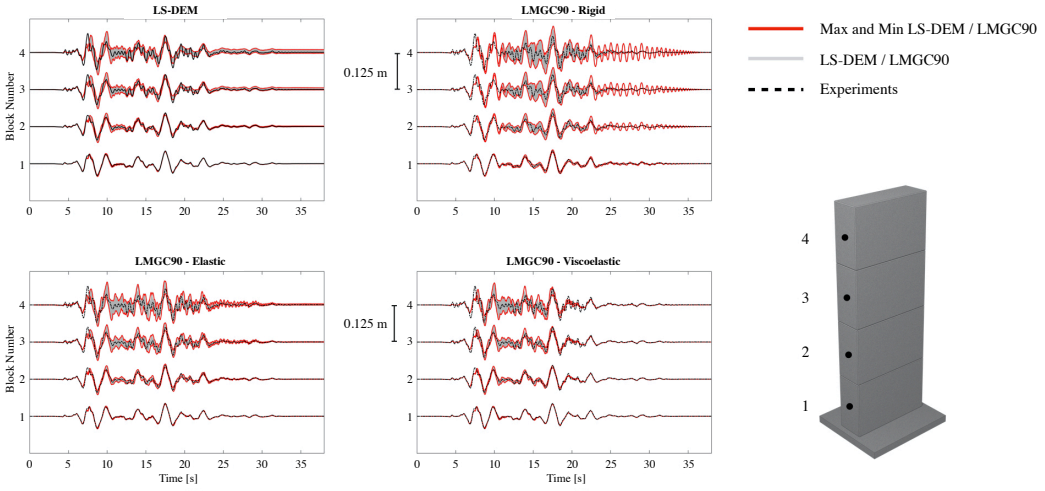

Figure 3.13: Displacement time-histories for Configuration 2.

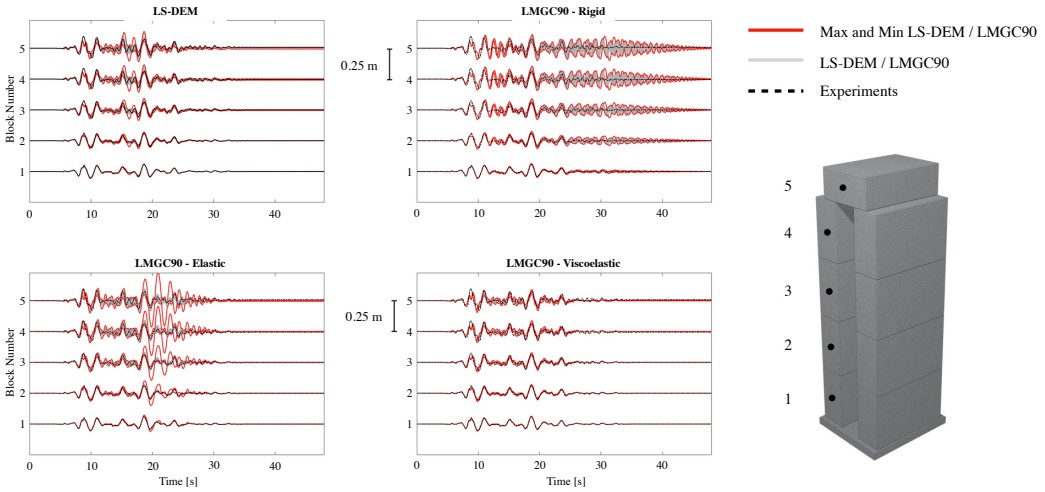

Figure 3.14: Displacement time-histories for Configuration 3.

LMGC90 Results

In LMGC90, three different mechanical behaviors have been analyzed: rigid, elastic, and visco-elastic. The visco-elastic block model described the real seismic behavior of the four configurations the best. The elastic block model described the real

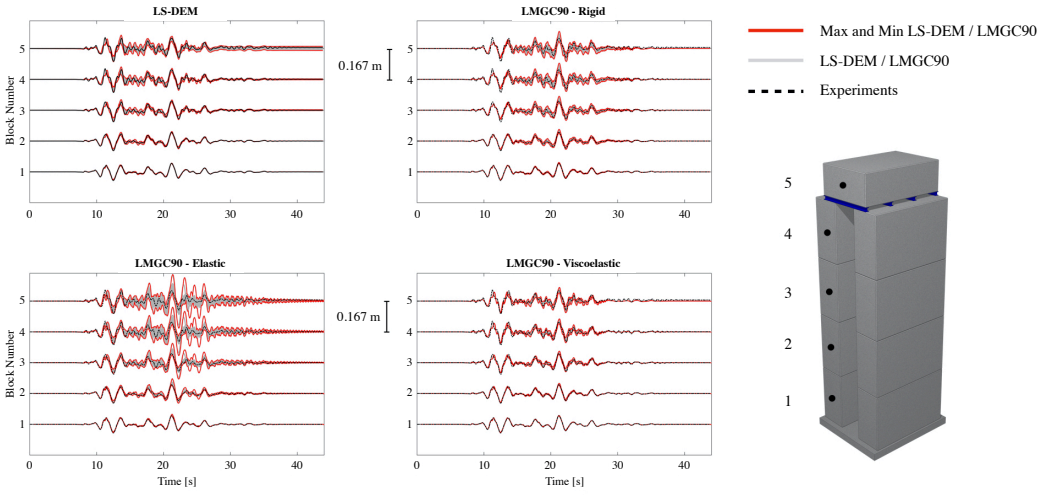

Figure 3.15: Displacement time-histories for Configuration 4.

behavior in a satisfactory way for Configurations 1 and 2. For Configurations 3 and 4, the simulated results are not ideal and is showing large deviations between tests due to more complicated concrete structures. The rigid block model behaved satisfactory for all four configurations. Within the same model (rigid, elastic, and visco-elastic), similar responses from LS-DEM were observed: more oscillations and thicker envelope towards more complicated concrete structures.

Comparison and Discussion

Given that the blocks in LS-DEM do not deform, it is natural to compare LS-DEM model with the rigid model of LMGC90. Since the contact surfaces in LS-DEM are visco-elastic due to the presence of springs and dampers, we also included the elastic and visco-elastic behaviors from LMGC90 for references.

From both models, the resemblance between simulation results and experiments is remarkable. Some oscillations and variations in residual displacements can still be observed from certain simulations. However, since the exact values of the input variables from reality are unknown, the experiment data can only be taken as a reference. The stochastic nature of the system is accounted for in the simulations, but the experiment is only one realization of a stochastic system itself. Indeed, the experiments only provided one set of data for each configuration at each earthquake intensity level, while the adopted LHS technique, as any Monte Carlo method, leads

to provide multiple realizations for each model at each intensity level.

Given that only absolute displacements are compared, it would be ideal to benchmark the rotational behaviors of the blocks as well. Although such data can be easily extracted from the simulations, rotation angles cannot be easily extracted from the experimental data due to the presence of noise given small block rotations.

3.5 Conclusion

The main objective of this study is to validate and benchmark two discrete-system-models (i.e., LS-DEM and LMGC90) against experiments done in Eucentre. After analyzing simulation results from both LS-DEM and LMGC90 calibrated models, we can conclude that the seismic performance coming from LS-DEM is similar to that from LMGC90, and both show remarkable resemblance to the actual experimental result obtained in Eucentre. Given that discrete objects in LS-DEM are rigid with visco-elastic contact, results from rigid model and visco-elastic model of LMGC90 are used for comparison. More rocking and/or sliding is observed from the models for complicated configurations like Configurations 3 and 4. Larger deviation in residual displacements is also observed, especially for Configuration 4 due to the inclusion of four supporting steel bars. It is important to point out that one experimental result is merely a single realization of a stochastic system. Due to time, resource constraints and the almost impossibility of recreating identical initial samples, it is impractical to repeat the experiments as many times as in the simulations. On the other hand, using numerical models as virtual experiments, a large number of realizations can be obtained (using multiple random parameters), generating a wealth of data and deeper insights that are difficult or impossible to obtain experimentally (e.g., force distribution, damage, kinematic fields, etc.). It is apparent that numerical virtual experiments offer a window into stochastic systems such as those studied herein.

Additionally, the study clearly shows that both numerical models can independently reproduce the experimental results. This finding gives us confidence that, since the experimental results at Eucentre can be replicated accurately, other perhaps more complex configurations can be reproduced. Indeed, the concrete specimens tested in experiments are simplified configurations utilized for benchmarking purposes only. The actual concrete configurations used at CERN for radiation shielding are more complex and involve a much larger number of blocks. Such complex and large systems are impractical for physical modeling. Instead, validated numerical models

can and should be deployed to investigate the seismic performance of such complex and large structural systems. Perhaps even more importantly, one can use such validated numerical models to design more seismic resistant concrete assemblies for a variety of purposes.

With the method proposed in [163], one can run Monte Carlo type simulations on discrete systems efficiently to obtain stable estimates with low variability. This study presented a detailed procedure for tuning the two discrete-system-models for simulating the dynamic response of radiation shielding concrete configurations. However, the same procedure can be replicated for any discrete systems, given user-defined margins and correlation structures. This study merely presented one family of numerical models for discrete concrete structures, yet the approach is amenable to any other numerical model, thereby proposing a new framework for modeling discrete structural systems.

Chapter 4

ROLE OF FRICTION AND GEOMETRY IN TUNING THE BENDING STIFFNESS OF TOPOLOGICALLY INTERLOCKING MATERIALS

T. Lu*, Z. Zhou*, P. Bordeenithikasem, N. Chung, D. F. Franco, J. E. Andrade, and C. Daraio. Role of friction and geometry in tuning the bending stiffness of topologically interlocking materials. *Extreme Mechanics Letters*, 71:102212, 2024. doi: 10.1016/j.eml.2024.102212.

4.1 Introduction

The demand for materials with adjustable physical properties and the ability to respond rapidly to environmental stimuli has been growing [146]. In particular, fabrics with adaptable or tunable stiffness are applicable for use in soft robotics, shape morphing structures, and wearable devices [107, 133, 170]. For example, tunable fabrics can find use in wearable medical devices, like exoskeletons, haptic systems, and reconfigurable medical supports [101, 123, 175]. At larger scales, applications of tunable fabrics include transportable and reconfigurable architectures, which transition from a compact and flexible state to a deployed and rigid state [1, 116].

Incorporating interlocking particles in fabrics opens up the possibility to incorporate added structural support and adjustable mechanical properties [6, 31, 40, 79]. The mechanical behavior of such structured fabrics or topologically interlocking materials (TIMs) is determined by the characteristics of their constituents and the topology of their arrangement [40, 105, 135**?**]. In most architected materials and woven fabrics, these mechanical behaviors are determined during the design process and remain fixed after the components are fabricated. However, in some realizations, the fabric properties can be adjusted through actuation [79, 106]. Wang, et al. demonstrated architected fabrics consisting of chain mail layers with interconnected particles, which demonstrate the ability to reversibly and gradually switch between soft and rigid states [106, 135, 170]. The control of the fabrics' stiffness is achieved by applying pressure at the boundary that jams the particles via vacuum suction, in a system similar to other structured fabrics [116, 133, 170]. While this example demonstrates the ability to create architected fabrics with tunable properties, the use

of vacuum actuation is not practical, because it requires bulky and energy intensive pumping systems. Using tensioned fibers or artificial muscles could be a more compact and power-efficient solution [166].

In this chapter, we study the response of a particular TIM system, consisting of truncated tetrahedral particles connected by woven tension wires [79, 135**?**]. Unlike the TIM system that is held solely by geometric interlocking and external in-plane constraint, which exhibits a softening stage before the TIM collapses [79], our fabric-TIM system shows a stiffening response during the indentation tests due to the gradual increment of anti-separation forces provided by the wires. The connecting wires facilitate the tunability of the bending modulus in response to adjustable applied tension, as demonstrated in Figures 4.1c–d [106, 135]. Additionally, they enable the formation of various flexible shapes while keeping the TIM structure intact. To better understand the fundamental mechanisms governing the tunability of the TIM system's apparent bending stiffness, we explore the role of contact angle and contact friction at a fixed applied wire tension, using experiments and numerical simulations.

4.2 Design and Fabrication of the Topologically Interlocking Materials

There are various designs of TIMs. Dyskin et al. [31] used tetrahedral solids to form layer-like structures that are interlocked topologically. Molotnikov et al. [106] constructed TIM systems made of osteomorphic blocks embedded with shape memory alloy wires that can alter the TIM's flexural stiffness when activated. Siegmund et al. [135] created TIM systems using truncated tetrahedron blocks integrated with internal constraint fibers or woven tow material, demonstrating interlocking systems confined by passive elements.

Tetrahedrons are the simplest platonic solid, and all platonic solids can be arranged into layer-like structures in which they are interlocked topologically [33]. Additionally, trapezoidal particles are known for their substantial contact surfaces [6] and have extensive applications in architected materials to enhance mechanical performance [171]. Drawing inspiration from the previous references, we study a classic system of a TIM assembled with truncated tetrahedron particles as the basic building blocks (Figure 4.1a). Using truncated tetrahedrons, as opposed to osteomorphic blocks, allows us to systematically change a single parameter, such as dihedral angle, to dictate the amount of interlocking. Moreover, since truncated tetrahedrons do not completely fit into each other, the relaxed state is more flexible and similar to a

fabric. Inspired by Siegmund et al. [135], we design the particles with longitudinal and latitudinal through-holes. We use nylon wires to weave through each discrete particle and interconnect them, as depicted in Figure 4.1b. To actuate the fabrics, we apply different levels of tension to the wires and thereby jam the particles with their neighbors to form an interlocked state (Figures 4.1c–d). The combined outer surface of the truncated tetrahedrons upon post-tensioning is a flat plane. The resulting assemblies possess geometric contact and interlocking periodicity.

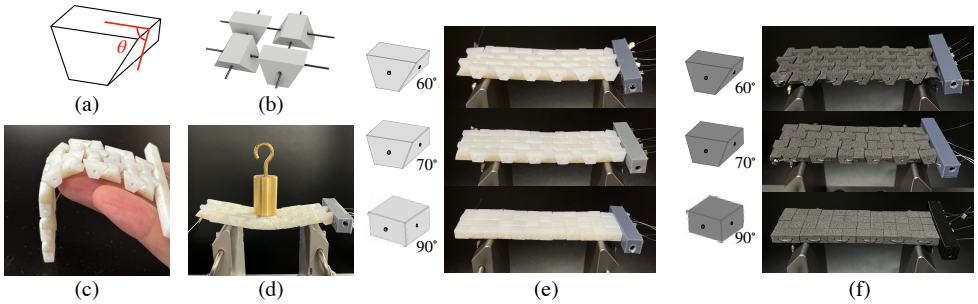

Figure 4.1: Schematic and physical samples of the TIMs. (a) Schematic of a basic building block (particle) in the shape of a truncated tetrahedron [31], with dihedral angle, θ, between the truncating surface and the side surface of particle; (b) Schematic of particles inter-connected by post-tensioned wires; (c) Unactuated, soft state of the sample; (d) Actuated, stiff state of the sample; (e-f) Samples made by particles with $\theta = 60°$, $70°$ and $90°$; Samples shown in (e) are made by Vero White, with a measured friction coefficient of 0.2; samples shown in (f) are made by Nylon Polyamide 12, with a measured friction coefficient of 0.6.

A series of TIMs were produced by varying two different particle parameters: the particle's dihedral angles, θ (Figure 4.1a) and their surface friction. The particles were fabricated with three different dihedral angles, 60°, 70°, and 90°, where the latter is simply a prism geometry with no geometric interlocking. To vary the surface friction, we 3D-printed the particles using two different materials of similar stiffness: Vero White (VW) using an Objet Stratasys Connex 500, and Nylon Polyamide 12 (PA12) using a Sintratec SLS 3D printer. Particles were cleaned by removing the outer support material. The Vero White particles were additionally cleaned in a 2 percent aqueous solution of NaOH to remove the remaining support material. The coefficients of friction were determined experimentally after the particles had been cleaned, using sliding friction tests. The resulting surface friction coefficients were measured to be 0.2 and 0.6, respectively. The particles were then woven together with 0.3 mm diameter nylon wire. The system is subsequently actuated with a

small motor (28BYJ-48 Stepper Motor) that controls the amount of wire tension and therefore jamming the particles. A custom-designed fixture was 3D-printed for the motor housing and tensioning mechanism with sufficient clearance space for the tension meter (Checkline ETB-2000). The tension should attain the predetermined threshold, ensuring that the wire remains within the elastic range during the testing phase. The tension meter was used to gauge the tension and determine whether to incrementally increase the tension by spinning the motor. Once the desired average tension was achieved in the wires, the tension was secured with clamp beads to hold the wire in place. Then the woven sample was removed from the fixture with the motor.

4.3 Simulations

For a more systematic analysis of the TIM fabrics' behavior as a function of particle's geometry and constituent material properties, a reliable and validated numerical model is necessary. Level Set Discrete Element Method (LS-DEM) is used to model the physical experiment. LS-DEM is a variant of the traditional DEM allowing arbitrary object shapes. Originally developed for granular applications [76, 100], LS-DEM has recently been adapted to study the structural behaviors of multi-block structures [53, 180], and the structural analysis of TIM, showing satisfactory results in capturing the slip-governed failure [41, 42] and the deflection limit [157] of the slab-like TIM. LS-DEM uses level set functions as the geometric basis, which calculates the signed distance ϕ from any arbitrary point in the space to the nearest surface of the grain. For example, in this work, a cross-sectional slice of a basic building block, which is the shape of a truncated tetrahedron, is a trapezoid in 2D, as shown in Figure 4.2a. The surface of the building block, or particle, can be reconstructed by $\phi = 0$. We impose a set of surface nodes with uniform discretization size onto each particle (Figure 4.2b). When checking potential particle contact, we take the position of each surface node $\boldsymbol{x}$ of one particle and check the corresponding level set value from another neighboring particle. If $\phi(\boldsymbol{x}) \leq 0$, then contact exists between this pair of particles.

Given the discrete nature of the woven-connected particles, LS-DEM is capable of extracting particle-scale information at micro-mechanical level, thus providing insight into how friction and contacts between particles affect the macroscopic property such as sample bending stiffness. Furthermore, the use of level set function provides flexibility in particle shape control, allowing us to easily simulate different particle shapes and investigate the combined geometric shape effects to the sample's

overall behavior. The use of LS-DEM is also computationally efficient compared to other simulation methods such as FEM for potential simulations of large ensembles of particles [23].

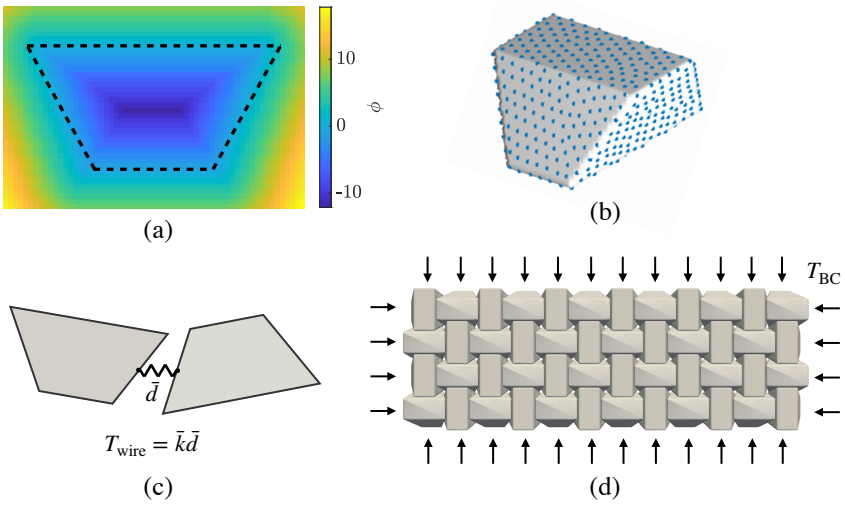

Figure 4.2: Numerical model setup. (a) Illustration of the level set matrix of a slice of the truncated tetrahedron; (b) The particle is reconstructed by surfaces with $\phi = 0$; the imposed surface nodes are shown in blue dots; (c) Illustration of a pair of neighboring particles, connected by a massless spring with stiffness $\bar{k}$ and elongation $\bar{d}$; (d) Illustration of the sample under post-tensioning force T_{BC}.

We use point forces acting on the boundary particles T_{BC} to model the post-tensioning effect of the wires (Figure 4.2d). On top of that, we use massless springs connecting the face center of the side of each particle to the face center of the side of its neighbors (Figure 4.2c). The neutral position of the spring is at a distance $\bar{d} = 0$. The springs connecting neighboring particles can only exert tensile forces on the connected particles. When two neighboring particles are separated, the wire force T_{wire} is calculated as

$$T_{\text{wire}} = \bar{k}\bar{d}\,, \tag{4.1}$$

where $\bar{k}$ is the stiffness of the spring and is calibrated to match the experimental result of an uniaxial tension test carried out on a single woven wire.

4.4 Mechanical Characterizations

In order to experimentally investigate the macroscopic properties of the sample under various particle geometries and material properties, displacement-controlled three-point bending tests were performed with an Instron E3000 Mechanical Testing Machine (Figure 4.3a). The indenter had a set loading rate of 0.5 mm s^{-1}. To ensure

that the TIM systems deform within their components' elastic limits, we imposed a maximum indentation depth of 5 mm. This indentation depth was determined by performing three-point bending tests on 3D-printed slabs of the same material with the same fabric sample dimensions. Tests show no yielding behavior within 5 mm. This indentation depth also guarantees that the wire remains within its elastic limit, confirmed by independent tensile tests on the wire, aligning with the assumption made in Equation 4.1.

To compare the bending performance of the different fabrics, we define an apparent elastic bending modulus, E^*, as [170]:

$$E^* = \frac{KL^3}{4bh^3}. \tag{4.2}$$

Here, K is the stiffness of the initial linear regime of the force-displacement plot obtained from the test machine, L is the support span, b is the width of the sample, and h is the thickness of the sample before testing.

We study the role of friction and particle's shape on the overall fabric's behavior, comparing the apparent bending moduli values extracted from the experiments. Figure 4.3b shows an overview of the bending modulus calculated from Figures 4.3c–d using Equation 4.2. Both increasing surface irregularities (i.e., friction between particles) and geometric interlocking have a positive correlation with the bending modulus. Samples made with PA12, resulting in a higher surface friction coefficient ($\mu = 0.6$) than those made with Vero White (VW) ($\mu = 0.2$), exhibit almost twice as much bending modulus as VW samples of the same particle geometry. Figures 4.3c–d show the force-displacement plot for VW samples and PA12 samples accordingly. The force-displacement curves obtained from the three-point bending tests show an initially linear regime at small indentation depths, primarily due to the elastic response of the wire while the particles spread out. However, as the displacement increases, a nonlinear response is observed, most likely because of frictional sliding and local rearrangement of the particles within the system. Comparing the force-displacement plot within samples of the same material (Figures 4.3c–d), we see that particles with smaller dihedral angle θ, which result in higher interlocking upon post-tensioning, show higher stiffness. If we compare samples of same particle geometry but made with different materials, samples with higher surface friction show higher stiffness.

To construct the numerical model, we first construct the particles using level set functions and surface nodes (Figures 4.2a–b). We then arrange and post-tension

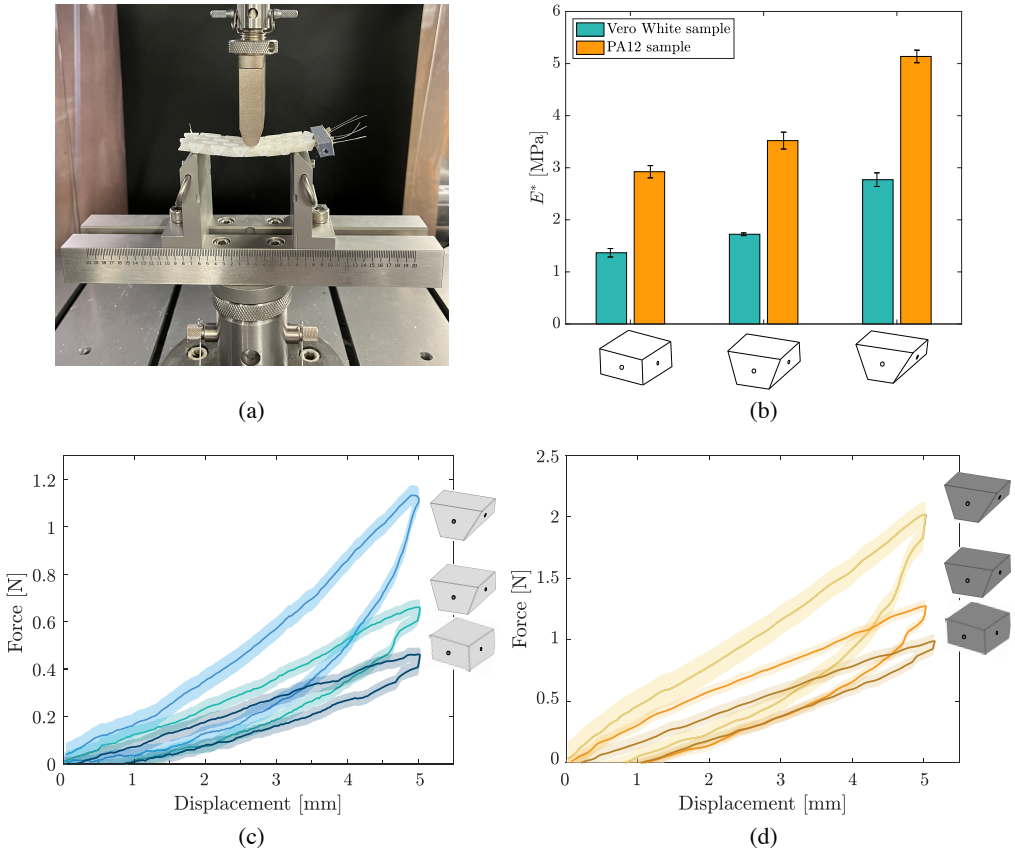

Figure 4.3: Experiment setup and results. (a) The three-point bending test setup with sample; (b) Apparent bending modulus of the different samples, fabricated with 2 different constitutive materials (Vero White and PA12) and three different dihedral angles (θ = 60°, 70° and 90°); (c) Force-displacement plots of the Vero White samples; (d) Force-displacement plot of the PA12 samples. In (c) and (d), for each sample, a total of five experiments are performed. The solid lines represent the average force-displacement behavior, and the shaded regions show the standard deviation over five experiments.

the particles (Figures 4.2c–d), as described in Chapter 4.3. To simulate the testing setup, we construct a 1:1 model of the experiment apparatus using the same level set technique (see Supplementary Information). We then move the indenter downward at a constant loading rate. In the experiments, though the fabrics samples are prepared and post-tensioned according to the same procedure, there is no way to explicitly measure the slack of wires introduced during fabrication, and consequently it is not possible to know the exact tensile forces, T_{BC}, exerted by the wires on all particles. Therefore, we adjust the boundary force T_{BC} in the bending simulation of the 70° VW sample until the simulated apparent bending modulus E^* matches

with that of the corresponding experiment. To ensure consistency and uniformity, we then apply the same calibrated boundary force to the remaining five simulations (60° and 90° VW samples, as well as 60°, 70° and 90° PA12 samples).

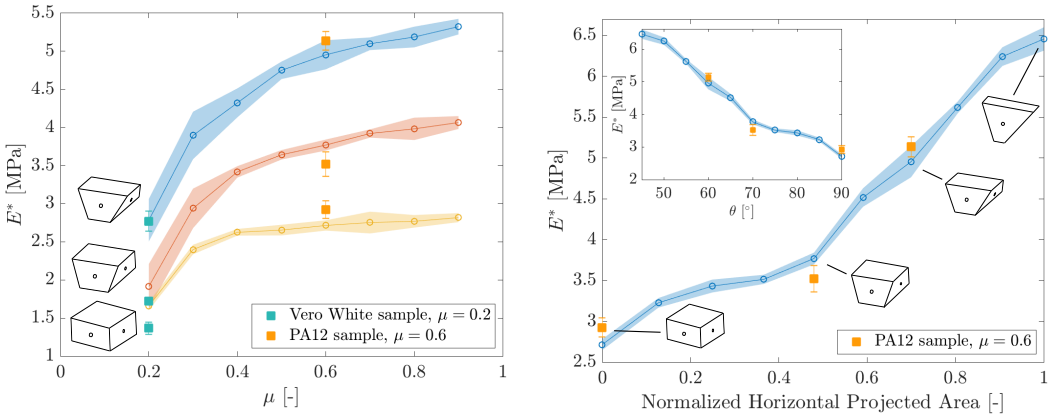

(a) (b)

Figure 4.4: Comparison of experiments and simulations. (a) Simulated bending modulus of samples consisted of particles with $\theta = 60°, 70°$ and $90°$ across different friction coefficient, from 0.2 to 0.9. For each particle shape at each friction coefficient, five simulations are run. For each run, noise is introduced to the initial particle position, particle orientation and boundary force T_{BC}. The solid line represents the average modulus, while the shaded regions show the standard deviation across five runs. Experiment results obtained from VW ($\mu = 0.2$) and PA12 ($\mu = 0.6$) samples are marked by green and orange, respectively; (b) Simulated bending modulus vs. normalized contact area in horizontal projection with particles from $\theta = 45°$ to $\theta = 90°$ with 5° increments. The projected contact area is calculated based on the initial configuration of the particle orientation, and is normalized by the area of the 45° particle. Inset: simulated bending modulus vs. θ. Similar to (a), five simulations are run for each particle shape and noise is introduced in the initial state of each simulation. Experiment results from PA12 are marked in orange.

As depicted in Figure 4.4, the resulting calibrated numerical model exhibits good agreement with experimental data regarding the apparent bending modulus E^*. In Figure 4.4a, we show that as the friction coefficient reaches larger values (>~0.3), the bending modulus of the samples does not increase as much, particularly for the samples with the least geometric interlocking (rectangular prism particles). As expected, in samples with more interlocked particles, the modulus increases more rapidly with increasing friction coefficient. For the 90° prism particles, the interwoven wire and friction between neighboring particles are the main factors that counteract out-of-plane deflection. With more interlocked particles (60° prism

particles), however, not only friction and the wire, but also geometric constraints are collectively counteracting the out-of-plane deflection.

In order to analyze how geometry affects the modulus, we simulate the bending tests of samples made by 7 other particles of different degrees of geometric interlocking. Wang et al. [170] reported a quadratic law relating average particle contact number to the apparent bending modulus. In this work, since all particles are generated with surface nodes of uniform discretization size, the contact number per particle upon contact directly translates to contact area between the contacting neighboring particles. Since we are assuming a small indentation depth, we estimate the contact area to be the maximum area of the side surface of a truncated tetrahedron in contact with its neighbor at initial configuration before indentation, which is one trapezoid overlapped with a flipped trapezoid, or a hexagon. We plot the bending modulus against the normalized contact area projected onto the horizontal plane. Since the horizontal plane is directly perpendicular to the indenting direction, the projected horizontal contact area acts as the effective contact area for the solid material to counteract the indentation force. From Figure 4.4b, we see that the bending modulus scales almost linearly with the horizontally projected contact area. The dihedral angle θ scales inverse-linearly with the bending modulus, due to the fact that particles with larger θ have smaller horizontal projected contact areas. From Figure 4.4b and the additional inset figure, we see that particle geometry is a crucial factor in contributing to the bending modulus.

In contrast to [170], which exhibited a power law relationship, we find an approximately linear scaling between the projected horizontal contact area and the bending stiffness in our samples. We attribute this difference to the presence of the woven wires, which make the samples with less geometric interlocking rely more on elastic wire forces. During indentation, the wires in samples made from the rectangular prism particles are expected to be stretched more compared to samples made from the 45°-particles. This indicates that the wires may exert increased anti-separation forces within the 90°-particle TIMs in contrast to the other particles that can rely on greater geometric interlocking.

4.5 Conclusion

In this chapter, we study the role of particles' geometry and inter-particle friction in the bending response of TIM systems consisting of truncated tetrahedron particles woven together with nylon wires. We fabricate samples with particles of varying

interlocking contact angles and surface friction. In post-tensioned state, we find that both high friction and large horizontally projected contact area between the neighboring particles contribute positively to the resulting sample bending resistance. The positive effect of friction to bending stiffness diminishes as friction coefficient increases. The projected horizontal contact area positively contributes to the bending modulus at a linear rate.

The TIM is a complex system with many factors at play. Besides the friction and geometric interlocking, sample thickness and external post-stress also have profound effects on bending response. In order to isolate the effect of friction and geometry, we keep the sample thickness and post-stress consistent throughout all experiments and simulations. More comprehensive study on the combined effect of all factors should be investigated in future work.

4.6 Supplementary Information

Numerical Model Setup

Truncated tetrahedron particles are characterized by a level set grid of 2 mm/voxel. The surface nodes are discretized with a surface density of 230 points/cm^2. The contact mechanism of a pair of penetrating neighboring particles are estimated by visco-elastic models composed of linear springs and viscous dampers. The linear springs have normal and shear stiffnesses k_n and k_s. The choice of these parameters takes into account factors considering material modulus and TIM arrangements, ensuring no excessive overlap between contacting particles [42]. We assume the stiffnesses of the particles made of two materials are comparable. The viscous dampers have normal damping coefficient γ_n estimated based on coefficient of restitution C_res [155] by

$$\gamma_n = 2\sqrt{m k_\mathrm{n}} \frac{-\ln C_\mathrm{res}}{\sqrt{\pi^2 + \ln {C_\mathrm{res}}^2}}, \tag{4.3}$$

where m is the mass of the particles. LS-DEM uses an explicit time integration scheme. The critical time-step is estimated by [156]

$$\Delta t = 0.4\sqrt{\frac{2m}{5k_\mathrm{s}}}. \tag{4.4}$$

The wire stiffness $\bar{k}$ is calibrated to match the experimental result of a single woven wire in an uniaxial tension test. The set of parameters used in this work is documented in Table 4.1.

Table 4.1: Model parameters.

Parameter	Value	Units
Normal particle stiffness k_n	2	MN/m
Shear particle stiffness k_s	2	MN/m
Wire stiffness $\bar{k}$	720	N/m
Friction coefficient μ	$\{0.2,0.3,\ldots,0.9\}$	-
Time-step Δt	5.6e-7	s
Coefficient of restitution C_{res}	0.5	-

We construct a 1:1 numerical model for the testing apparatus (Figure 4.5) with the same level set grid density and surface discretization density. The indenter and the two supports have the same dimension as the actual experimental test machine. The two supports are placed 6 cm apart, same as the experiment. After the numerical TIM sample has been post-tensioned, we allow the sample to settle onto the supports by gravity. We then move the indenter downward at a constant speed. Since we have a small time-step of $\Delta t = 5.6 \times 10^{-7}$ s for numerical stability, we apply a global damping parameter of $1 \times 10^{-4}/\Delta t$ s^{-1} to ensure quasi-static conditions and to avoid excessive computation time [76].

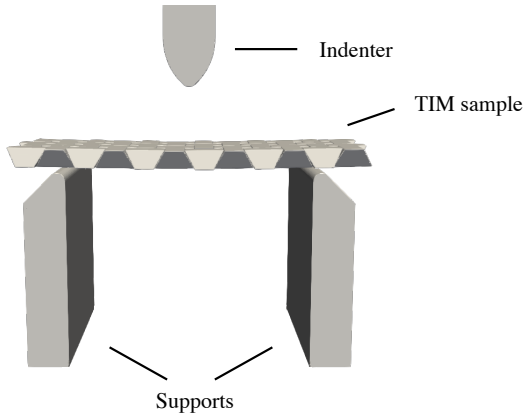

Figure 4.5: Numerical test apparatus.

Chapter 5

TENSEGRITY STRUCTURES AND DATA-DRIVEN ANALYSIS FOR 3D CELL MECHANICS

Z. Zhou, J. Ulloa, G. Ravichandran, and J. E. Andrade. Tensegrity structures and data-driven analysis for 3D cell mechanics. Submitted to: *Computer Methods in Applied Mechanics and Engineering*.

5.1 Introduction

Living cells constantly experience complex interactions of mechanical forces [173]. The ability of cells to sense and respond to such mechanical stimuli along with other biochemical cues is critical to cellular functionality [36, 52, 181]. These functions are mediated through changes in the cytoskeleton (CSK), which provides a structural basis for the mechanical and morphological behavior of cells [58, 62, 63, 149, 167]. The CSK comprises a dynamic network of proteins, mainly consisting of microtubules, intermediate filaments, and microfilaments. Through receptor proteins, the CSK senses and transmits forces to interact with the adjacent cells and microenvironment, in turn orchestrating cell shape changes, polarity, and motility [7]. An equilibrium in forces is maintained at the cellular level, balancing internal mechanical forces exerted by the contractile actin filaments, resisting microtubules in compression, and external forces from the extracellular matrix (ECM) [128]. This state of pre-existing stress in the CSK is referred to as prestress. Multiple studies have reported the central role of prestress in cellular mechanotransduction and mechanobiology [20, 59, 60, 143]. Altogether, changes to the mechanical properties of the CSK can lead to both cell development and disease [47].

Traditional computational efforts for simulating cell mechanics using the continuum approach describe the cell as an elastic, viscous, or viscoelastic medium, assuming the cell is composed of materials with certain continuum material properties. For example, the cortical shell–liquid core model assumes single or several layers of cortex with surface tension, with the cell interior modeled as Newtonian fluid with certain viscosity [69, 176]. Other continuum models simulate the whole cell as a homogeneous solid [103, 132]. For a complete review, readers are referred to [89]. Such continuum models are good approximations for a range of experimental

observations. However, as experimental conditions become complex, constitutive models require additional parameters that are essentially empirical and often lack physical meaning. Moreover, it is difficult to consider subcellular processes, such as protein level activities, into such frameworks, except in an averaged sense [45].

In individual cell-based approaches, most models can be grouped into two subsets: lattice-based models and off-lattice models [102]. The former tracks cells along rigid grids, with examples being the fixed-lattice Cellular Automata and the Cellular Potts model [45]. The latter has no grid restrictions and the cells are tracked via centers of mass, as in the off-lattice center dynamics model [117], or their boundaries, as in the vertex dynamics models [46]. In vertex dynamics models, additional biochemical rules can be employed to study more advanced cell behaviors such as cell rearrangements and oscillations [45, 90].

Most of the aforementioned modeling frameworks either cannot account for cellular prestress, despite its crucial role in determining cell behaviors, or lack physical insight in doing so. Models that account for the cell's internal structure or the CSK are still relatively scarce [117]. Moreover, it is difficult for the aforementioned models to directly link mechanical forces to specific load-bearing structures and molecules inside living cells, although such links are rather ubiquitous. For instance, Harris et al. [55] reported that depolymerizing actin CSK can result in a decrease in the stiffness of a monolayer by 50%. It is therefore crucial for a model to incorporate not only prestress but also subcellular processes, such as distributing changes to specific groups of cell members, in order to further understand the mechanics of cells.

Complementing these frameworks, computational models based on micro/nanostructural approaches offer a different perspective, focusing on the deformation of the CSK [120, 128, 144]. Among these, one category embraces the concept of tensegrity (tensional integrity), a structural principle originated in architecture by Buckminster Fuller [48]. Tensegrity is a self-stable assembly consisting of continuous tensile elements (tendons) and discontinuous compressive elements (bars). Tendons and bars are pin-connected in force equilibrium, setting the tensegrity structure in a tensile prestressed state, reminiscent of the force balance between contractile actin filaments and compression-supporting structures such as microtubules [63]. Furthermore, studies have shown that cell stiffness scales with the CSK prestress, as predicted by tensegrity models [168, 169]. These factors make the tensegrity model a conceptually simple idea for simulating cell mechanics.

In this context, Sun et al. [149] combined the CSK-based tensegrity model with a biochemical mechanism to simulate more realistic cellular-level processes. Their study, however, is largely focused on the biochemomechanical processes of a single cell. The collective response of tensegrity structures as an assembly of multiple cells is not investigated. Liu et al. [93] proposed a tensegrity model combined with the vertex dynamics method to explain the stiffness difference between a single cell and a monolayer. Moreover, Wang et al. [165] proposed a multiscale model to investigate the static and dynamic response of cell monolayers. Due to the presence of torsion components in most tensegrity structures, application of multicellular tensegrity in cell mechanics has mostly been limited to 2D [125]; see, for instance, [93] and [165].

In this chapter, we propose a 3D multicellular tensegrity model capable of simulating cells in one-, two-, and three-dimensions, and investigate the response of such structure under different loading conditions. The tensegrity modeling framework is based on the Finite Element Method (FEM) in the finite (large) deformation setting and allows controlling initial prestress [98, 99]. As with any FEM model, the computational cost becomes exceedingly expensive as the number of elements increases, especially for our proposed use in cell mechanics. Therefore, to reduce the computational cost, we further perform simulations using a multiscale data-driven (DD) approach in concert with homogenization techniques. DD enables calculations directly from a material dataset while satisfying pertinent constraints and conservation laws, thus bypassing the empirical material modeling step in the conventional FEM [81]. The material (training) dataset can be extracted from lower-scale computations or experimental observations.

The structure of this chapter is as follows. In Section 5.2 and 5.3, we present a brief overview of the tensegrity formulation, followed by simulations of a single cell, a monolayer, and a multicellular spheroid, each compared with published experimental work. In Section 5.4, we briefly outline the DD framework, followed by 2D monolayer simulations, employing material data extracted from representative volumes of tensegrity structures. The DD solutions are then benchmarked against the tensegrity-based direct numerical simulations.

5.2 Tensegrity Structures

Modeling Framework

The tensegrity model is composed of pin-connected tensile and compressive elements. In the present work, we mostly adopt the modeling framework of Ma et al. [99], briefly summarized below.

Representing the Cartesian coordinates of each node as $\boldsymbol{n}_i = [x_i \ y_i \ z_i]^{\mathrm{T}}$, with $i = 1, 2, \ldots, N$ indexing the node number, the global nodal coordinate matrix $\boldsymbol{N} \in \mathbb{R}^{3\times N}$ can be constructed as

$$\boldsymbol{N} = [\boldsymbol{n}_1 \ \boldsymbol{n}_2 \ \ldots \ \boldsymbol{n}_N] \, . \tag{5.1}$$

In a single-vector formulation, the nodal coordinate matrix can be represented as

$$\boldsymbol{n} = [\boldsymbol{n}_1^{\mathrm{T}} \ \boldsymbol{n}_2^{\mathrm{T}} \ \ldots \ \boldsymbol{n}_N^{\mathrm{T}}]^{\mathrm{T}} \, . \tag{5.2}$$

The connectivity matrix $\boldsymbol{C} \in \mathbb{R}^{M\times N}$ represents the topology of the entire tensegrity structure, which consists of M_{b} compressive bars and M_{s} tensile strings. For each element e_{ij}^k, ($k = 1, 2, \ldots, M$, $M = M_{\mathrm{b}} + M_{\mathrm{s}}$) connecting node $\boldsymbol{n}_i$ and $\boldsymbol{n}_j$, its corresponding kth row lth column entry C_{kl} satisfies

$$C_{kl} = \begin{cases} 1 & \text{if } l = i \, , \\ -1 & \text{if } l = j \, , \\ 0 & \text{otherwise} \, . \end{cases} \tag{5.3}$$

Each element e_{ij}^k has a length l_k, calculated as

$$l_k = \|\boldsymbol{n}_i - \boldsymbol{n}_j\| \, . \tag{5.4}$$

Accordingly, the global structure length vector $\boldsymbol{l} \in \mathbb{R}^M$ can be represented as

$$\boldsymbol{l} = \left[l_1 \ l_2 \ \ldots \ l_M\right]^{\mathrm{T}} \, . \tag{5.5}$$

Similarly, we define the global area vector $\boldsymbol{A} \in \mathbb{R}^M$ and modulus vector $\boldsymbol{E} \in \mathbb{R}^M$, given by

$$\boldsymbol{A} = [A_1 \ A_2 \ \ldots \ A_M]^{\mathrm{T}} \, , \tag{5.6}$$

$$\boldsymbol{E} = [E_1 \ E_2 \ \ldots \ E_M]^{\mathrm{T}} \, . \tag{5.7}$$

In each element k, the (axial) stress increment $\mathrm{d}\sigma_k$ can be calculated in terms of the (axial) strain increment $\mathrm{d}\epsilon_k$ as

$$\mathrm{d}\sigma_k = E_k \mathrm{d}\epsilon_k \, . \tag{5.8}$$

The general tensegrity framework is equipped to handle elastic or plastic materials. In this study, we assume members are elastic and have constant cross-sections. Hence, the internal force vector $\boldsymbol{t} \in \mathbb{R}^M$ can be calculated as

$$\boldsymbol{t} = [t_1\ t_2\ ...\ t_M]^{\mathrm{T}} = \mathrm{diag}(\boldsymbol{E})\ \mathrm{diag}(\boldsymbol{A})\ \mathrm{diag}(\boldsymbol{l}_0^{-1})\ (\boldsymbol{l} - \boldsymbol{l}_0)\,, \tag{5.9}$$

where $\boldsymbol{l}_0$ is the rest length vector before the application of prestress. Thus, by adjusting $\boldsymbol{l}_0$ and $\boldsymbol{l}$, we can achieve different levels of prestress in the structure. Finally, the force density vector $\boldsymbol{q} \in \mathbb{R}^M$ is assembled as

$$\boldsymbol{q} = [q_1\ q_2\ ...\ q_M]^{\mathrm{T}} = \mathrm{diag}(\boldsymbol{l}^{-1})\ \boldsymbol{t} = \mathrm{diag}(\boldsymbol{E})\ \mathrm{diag}(\boldsymbol{A})\ (\boldsymbol{l}_0^{-1} - \boldsymbol{l}^{-1})\,. \tag{5.10}$$

The tensegrity dynamics in the Lagrangian setting can be formulated as

$$\boldsymbol{M}\ddot{\boldsymbol{n}} + \boldsymbol{D}\dot{\boldsymbol{n}} + \boldsymbol{K}\boldsymbol{n} = \boldsymbol{f}_{\mathrm{ex}} - \boldsymbol{f}_{\mathrm{b}}\,, \tag{5.11}$$

where $\boldsymbol{M}$ is the global structure mass matrix, $\boldsymbol{D}$ is the damping matrix, $\boldsymbol{K}$ is the stiffness matrix, $\boldsymbol{f}_{\mathrm{ex}}$ is the external force vector, and $\boldsymbol{f}_{\mathrm{b}}$ is the body force vector (such as gravitational force). The stiffness matrix $\boldsymbol{K} \in \mathbb{R}^{3N \times 3N}$ can be constructed from the force density vector and the connectivity matrix as

$$\boldsymbol{K} = (\boldsymbol{C}^{\mathrm{T}}\ \mathrm{diag}(\boldsymbol{q})\ \boldsymbol{C}) \otimes \mathbb{1}\,, \tag{5.12}$$

where $\mathbb{1}$ is the identity matrix.

Due to the nature of the problems under study, we ignore the gravitational effects on the elements. We also focus on the static response, hence eliminating the mass and damping matrix. Equation 5.11 can then be simplified to

$$\boldsymbol{K}\boldsymbol{n} = \boldsymbol{f}_{\mathrm{ex}}\,. \tag{5.13}$$

Accordingly, the linearized dynamics can be written as

$$\mathrm{d}(\boldsymbol{K}\boldsymbol{n}) = \mathrm{d}\boldsymbol{f}_{\mathrm{ex}}\,. \tag{5.14}$$

Since $\boldsymbol{K}$ is dependent on nodal coordinates $\boldsymbol{n}$, Equation 5.14 can be rewritten using the chain rule as

$$(\boldsymbol{K}_{\mathrm{G}} + \boldsymbol{K}_{\mathrm{E}})\mathrm{d}\boldsymbol{n} = \mathrm{d}\boldsymbol{f}_{\mathrm{ex}}\,, \tag{5.15}$$

where

$$\boldsymbol{K}_{\mathrm{G}} = (\boldsymbol{C}^{\mathrm{T}}\mathrm{diag}(\boldsymbol{q})\ \boldsymbol{C}) \otimes \mathbb{1}\,, \tag{5.16}$$

$$\boldsymbol{K}_{\mathrm{E}} = \boldsymbol{A}_{\mathrm{eq}} \operatorname{diag}(\boldsymbol{E}) \operatorname{diag}(\boldsymbol{A}) \operatorname{diag}(\boldsymbol{l})^{-3} \boldsymbol{A}_{\mathrm{eq}}^{\mathrm{T}}\,, \tag{5.17}$$

$$\boldsymbol{A}_{\mathrm{eq}} = (\boldsymbol{C}^{\mathrm{T}} \otimes \mathbb{1}) \operatorname{blkdiag}(\boldsymbol{N}\boldsymbol{C}^{\mathrm{T}})\,. \tag{5.18}$$

Here, $\boldsymbol{K}_{\mathrm{G}}$ is the geometric stiffness matrix, governed by the structure's topology and member force density; $\boldsymbol{K}_{\mathrm{E}}$ is the material stiffness matrix, governed by the elements' axial stiffness; and $\boldsymbol{A}_{\mathrm{eq}} \in \mathbb{R}^{3N \times M}$ is the equilibrium matrix. For details of the general tensegrity FEM framework and derivations, readers are referred to [99].

Designing self-stress

Similar to Equation 5.13, the equilibrium equation can also be written as

$$\boldsymbol{A}_{\mathrm{eq}}\boldsymbol{q} = \boldsymbol{f}_{\mathrm{ex}}\,, \tag{5.19}$$

except that Equation 5.19 is a linear form with respect to force density $\boldsymbol{q}$. With equilibrium written in this form, one can design initial self-stress as follows. We first apply singular value decomposition (SVD) to $\boldsymbol{A}_{\mathrm{eq}}$:

$$\boldsymbol{A}_{\mathrm{eq}} = \boldsymbol{U}\boldsymbol{\Sigma}\boldsymbol{V}^{\mathrm{T}}\,. \tag{5.20}$$

From [122], we know the independent states of self-stress can be calculated from the null space of $\boldsymbol{A}_{\mathrm{eq}}$. For $\boldsymbol{A}_{\mathrm{eq}} \in \mathbb{R}^{3N \times M}$ with rank r, the number of independent self-stress modes s can be calculated as

$$s = M - r\,. \tag{5.21}$$

When $s = 0$, the structure is statically determinate and has a unique solution for any given load $\boldsymbol{f}_{\mathrm{ex}}$. When $s > 0$, there is an s-dimensional infinity of solutions. In this case, $\boldsymbol{V}$ in Equation 5.20 can be expressed as

$$\boldsymbol{V} = \left[\boldsymbol{v}_1\ \boldsymbol{v}_2\ \ldots\ \boldsymbol{v}_r \;\vdots\; \boldsymbol{w}_1\ \boldsymbol{w}_2\ \ldots\ \boldsymbol{w}_s\right], \tag{5.22}$$

where $\boldsymbol{w}_i$ $(i = 1, 2, \ldots, s)$ are s independent self-stress modes that satisfy Equation 5.19. Letting

$$\boldsymbol{V}_1 = [\boldsymbol{v}_1\ \boldsymbol{v}_2\ \ldots\ \boldsymbol{v}_r]\,, \tag{5.23}$$

$$\boldsymbol{V}_2 = [\boldsymbol{w}_1\ \boldsymbol{w}_2\ \ldots\ \boldsymbol{w}_s]\,, \tag{5.24}$$

we can calculate the self-stabilizing $\boldsymbol{q}_0$ given initial $\boldsymbol{f}_0$ as

$$\boldsymbol{q}_0 = \boldsymbol{A}_{\mathrm{eq}}^{+}\boldsymbol{f}_0 + \boldsymbol{V}_2\boldsymbol{z}\,, \tag{5.25}$$

where $\boldsymbol{A}_{\text{eq}}^{+}$ is the pseudo-inverse of $\boldsymbol{A}$ and $\boldsymbol{z} \in \mathbb{R}^{s}$ is the self-stress coefficient.

In Section 5.2, we will introduce a type of tensegrity structure based on truncated octahedrons. The given structure has only one self-stress mode, i.e., $s = 1$. In this case, $\boldsymbol{V}_2 \in \mathbb{R}^{M \times 1}$ and z is a scalar.

Suppose we wish to specify the member forces in bars as f_{b}. Then, the self-stress coefficient can be calculated as [98]

$$z = \frac{\frac{f_{\text{b}}}{l_{\text{b}}} \mathbb{1}_{M_{\text{b}}} - \boldsymbol{I}_{\text{b}} \boldsymbol{A}_{\text{eq}}^{+} \boldsymbol{f}_0}{\boldsymbol{I}_{\text{b}} \boldsymbol{V}_2}\,, \tag{5.26}$$

where l_{b} is the bar length, $\mathbb{1}_{M_{\text{b}}} \in \mathbb{R}^{M_{\text{b}} \times 1}$ is a vector of 1 with a size of the number of bar elements and $\boldsymbol{I}_{\text{b}} \in \mathbb{R}^{M_{\text{b}} \times M}$ is a matrix to select bar elements,

$$I_{kl} = \begin{cases} 1 & \text{if } e^{l} \text{ is a bar element}\,, \\ 0 & \text{otherwise}\,. \end{cases} \tag{5.27}$$

Accordingly, the self-stabilizing member forces can be calculated by plugging z into Equation 5.25:

$$\boldsymbol{t}_0 = \boldsymbol{q}_0 \,\text{diag}(\boldsymbol{l})\,. \tag{5.28}$$

3D tessellation

Tensegrity structures remain in self-equilibrium, which requires special arrangements of the elements. There is a vast literature on the form-finding of eligible self-stabilizing tensegrity configurations [87, 88, 151]. However, constructing 3-dimensional tensegrity lattices has been difficult due to the low symmetry in common elementary tensegrity cells [125]. For our purpose of modeling 3D cell mechanics, we adopt the 3-dimensional tensegrity lattices from truncated octahedron elementary cells [88, 125] due to their ability to achieve space-tiling translational symmetry.

Each elementary unit is constructed from 12 compressive elements (bars, in black) and 36 tensile elements (tendons, in red), shown in Figure 5.1. The unit as it is right now is not 3D-translational or even 2D-translational due to the presence of twisted truncated surfaces (outlined in Figure 5.1 right). For the structure to be translational in $\mathbb{R}^2$ and $\mathbb{R}^3$, the unit cell needs to be reflected with respect to any of the side surfaces for the twist to be aligned (Figure 5.2 left). Any elementary unit cell must be paired up with reflected cells to make a connection, and no single pair of neighboring cells is identical (Figure 5.2 right). By alternating reflected cells in x, y, and/or z directions, the 4-cell system forms a building block that is translational in 2D (Figure 5.3a), and an 8-cell system forms a building block that is translational in 3D (Figure 5.3b) [125].

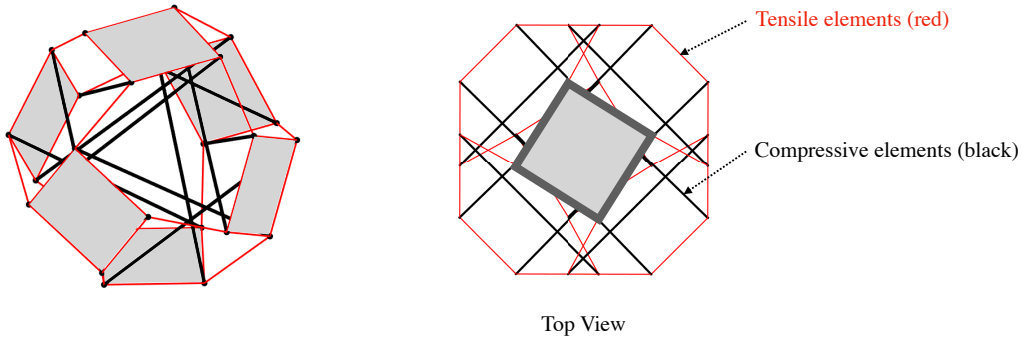

Figure 5.1: A tensegrity structure based on truncated octahedron elementary cell. Six side faces are filled with color for better viewing clarity. Side faces are twisted, as highlighted in darker contours in the top view.

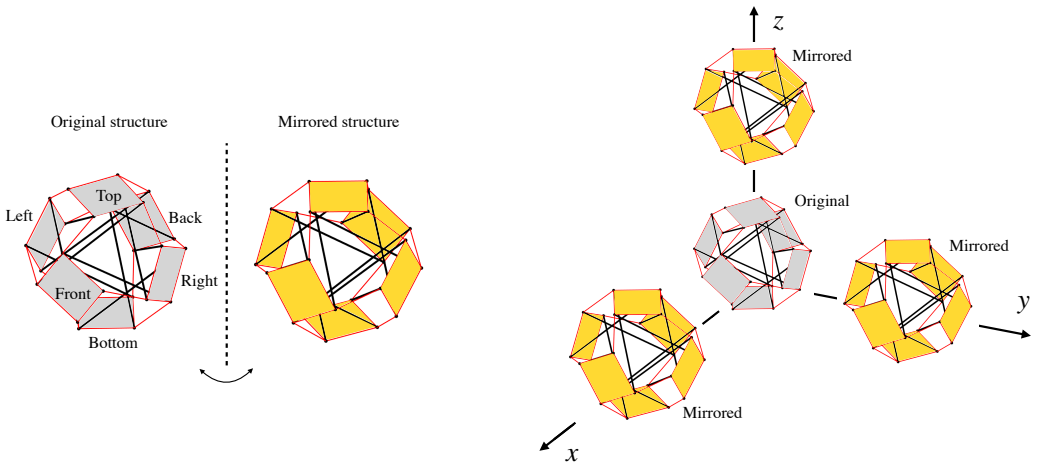

Figure 5.2: Schematic showing how to connect neighboring cells.

Extracting stresses and strains

We are primarily concerned with stress and strain information representative of the global tensegrity structures. Given a tensegrity assembly of volume V with a total number of elements M, the average stress tensor can be calculated using the Christophersen relation [21],

$$\bar{\boldsymbol{\sigma}} = \frac{1}{V} \sum_{e=1}^{M} \operatorname{sym} \left(\boldsymbol{t}_e \otimes \boldsymbol{l}_e \right), \tag{5.29}$$

where $\boldsymbol{t}_e$ is the internal force of element e and $\boldsymbol{l}_e$ is the corresponding length vector.

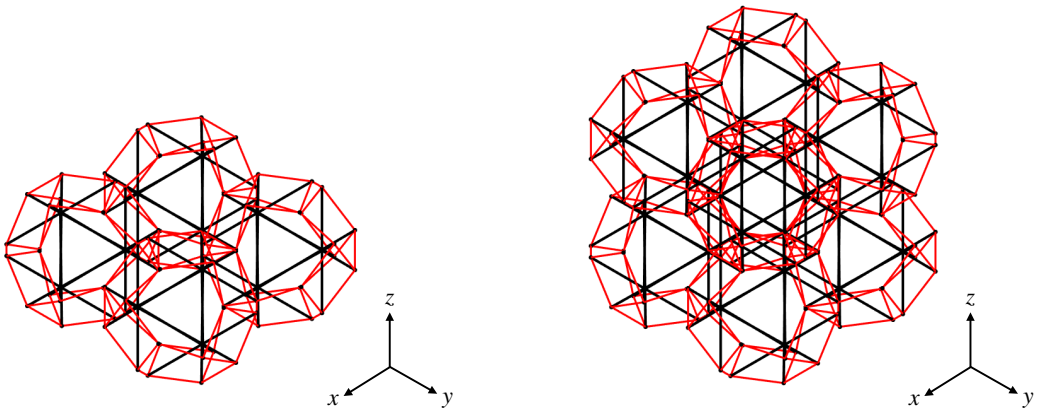

(a) (b)

Figure 5.3: Pseudo-2D (a) and 3D (b) translational building blocks.

Furthermore, the average strain can be calculated as [57]

$$\bar{\boldsymbol{\epsilon}} = \frac{1}{V} \sum_{i \in \partial J} \text{sym}\left(\boldsymbol{u}_i \otimes \hat{\boldsymbol{n}}_i\right), \tag{5.30}$$

where ∂J is the set of joint indices (node indices) on the boundary of the representative volume element (RVE), $\boldsymbol{u} = [u_x \; u_y \; u_z]^{\mathrm{T}}$ is the displacement of a node, and $\hat{\boldsymbol{n}}$ is the outward surface normal on the nodes contained in ∂J.

5.3 Modeling Cell Mechanics

In the cell CSK, the tensile actin filaments and compressive microtubules are reminiscent of tensegrity structures [62, 63]. In this section, we simulate and capture the mechanics of a single cell, a monolayer, and a multicellular spheroid using the proposed 3D tensegrity structure.

Single cell

Harris et al. [54] experimentally measured the force-displacement response of epithelial cells using combined AFM–confocal microscopy, which provides a good benchmark to calibrate the parameters used in our tensegrity model. We start by constructing a single elementary unit tensegrity cell, as depicted in Figure 5.1. The height of this elementary unit is set to match the height of a single epithelial cell used in the aforementioned experiment. The tendons are used as simplified representations of the actin cortex and stress fibers, and bars as representations of the microtubules and stiffened cross-linked actin bundles [149]. The bottom nodes

are fixed to mimic the experimental environment. Model parameters are listed in Table 5.1.

An indentation force of up to 3 nN is applied to the top nodes, as shown in Figure 5.5. From the resulting force-displacement plot shown in Figure 5.4, we see that a single elementary unit using the proposed tensegrity structure captures the force-displacement profile of an epithelial cell in an indentation test. As the indentation force increases, the rate of change in indentation displacement slows down, demonstrating nonlinearity in the cell response. This benchmark also serves as a calibration for the model parameters, which will be consistently used in subsequent multi-cellular tests.

Table 5.1: Parameters used in indentation simulation.

Parameter	Value	Units	Reference
Axial stiffness in bars E_b	1.2	GPa	[50]
Axial stiffness in tendons E_s	10	MPa	Assumed
Diameter of bars	0.1	μm	Assumed
Diameter of tendons	1	μm	[63]
Applied force F	3	nN	[54]
Cell height h	10	μm	[54]

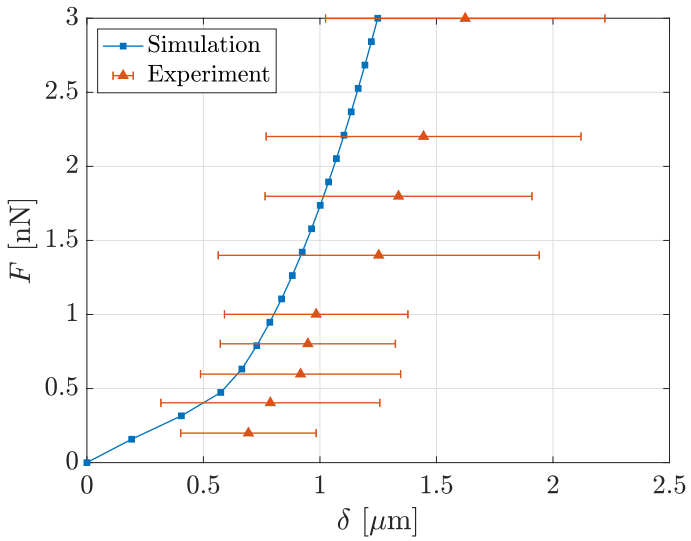

Figure 5.4: Force-displacement plot of a simulated single-cell indentation test. Experimental data is adapted from [54].

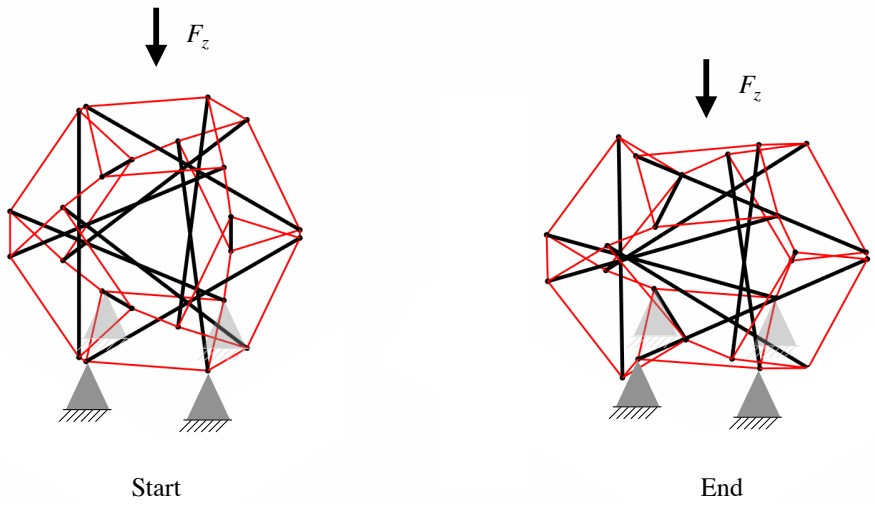

Figure 5.5: Single cell before and after the indentation test.

Monolayer

Harris et al. [55] reported the mechanical behavior of a freely suspended epithelial cell monolayer under uniaxial stretch and observed that the modulus of a monolayer is about two orders of magnitude larger than that of an isolated cell reported in [54]. To capture this distinction, we construct a tensegrity monolayer made of 60×30 2D building blocks (Figure 5.3a) with the same model parameters as Section 5.3 (Table 5.1). A monolayer of 60×30 in size is tested to be large enough to reach a representative response under uniaxial stretch. To replicate the experimental condition, we fix all the nodes on the bottom side of the monolayer and prescribe a 25% strain on the top side.

The resulting stress-strain plot is shown in Figure 5.6. We see that the simulated response of 25% stretch matches well with the reported experimental data. Up to 25% strain, we observe a nonlinear region where the rate of change of stress increases slowly. Since we assume the bars and tendons are linear elastic, this onset of nonlinearity below 25% can only come from the geometric stiffness of the structure. Upon loading, members of the tensegrity structure geometrically realign in the loading direction, therefore kinematically stiffening the structural response [63].

The simulated response above 25% falls out of the experimental envelope (data not shown). Harris et al. [55] reported the region where stress increases linearly to be within a 25%-50% strain range. Mechanical failure of the monolayer is reported

to occur at a strain value over 70%. We suspect the reason behind the discrepancy between our simulation and the experiment above 25% strain could be related to the model's simplified geometry and assumptions, making it suboptimal to capture the complex cellular-level mechanics occurring at large strains, such as intercellular adhesion rupture.

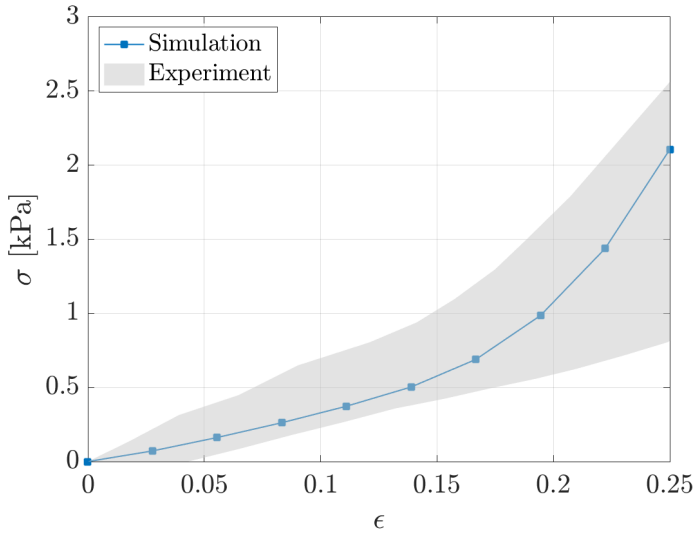

Figure 5.6: Stress-strain plot of the simulated monolayer uniaxial stretch up to 25% strain. Experimental data is adapted from [55]. The envelope shows the maximum and minimum stress values taken from the experiment at a given strain.

Using our model, we can easily extract the stress and strain field information from the tensegrity monolayer. In Figure 5.8, we plot the ϵ_{xx}, ϵ_{yy}, and ϵ_{xy} strain components of the tensegrity monolayer at the end of the 25% stretch. From the histograms, we see that the normal strain ϵ_{yy} is centered around 0.25, showing a quasi-uniform strain field in the y direction. On the other hand, the shear strain ϵ_{xy} is centered around 0. Most of the ϵ_{xx} strain is centered around 0, with a few values around -0.1. From the visualization (Figure 5.7), we see that the tensegrity cells near the left and right edge of the monolayer curve inwards, which is often the case for the geometry of this shape. These results have also been reported in [55], showing an overall good agreement between our simulation and the published experimental data.

So far, we have demonstrated that our proposed tensegrity model can capture the nonlinear behavior of a single cell in an indentation test and of a monolayer in a uniaxial tension test at low (but not necessarily infinitesimal) strain. In the next subsection, we will show that our model can also be constructed to capture 3D cell

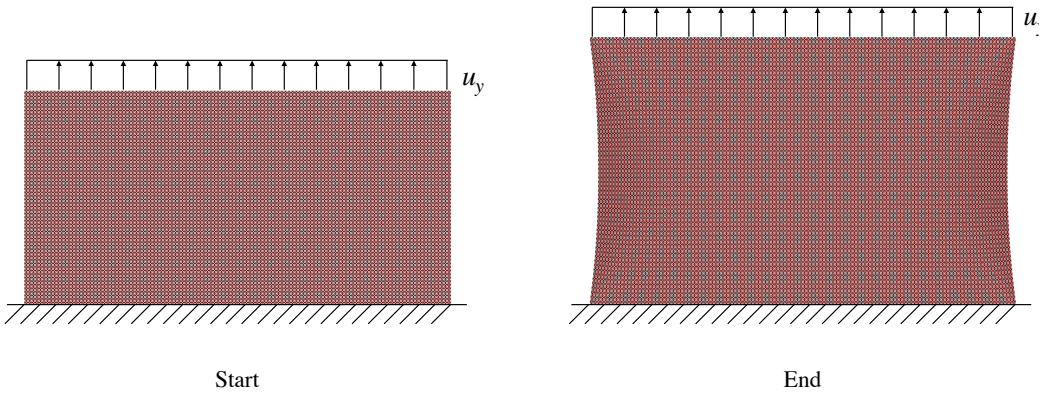

Figure 5.7: Monolayer before and after the tensegrity monolayer uniaxial stretch.

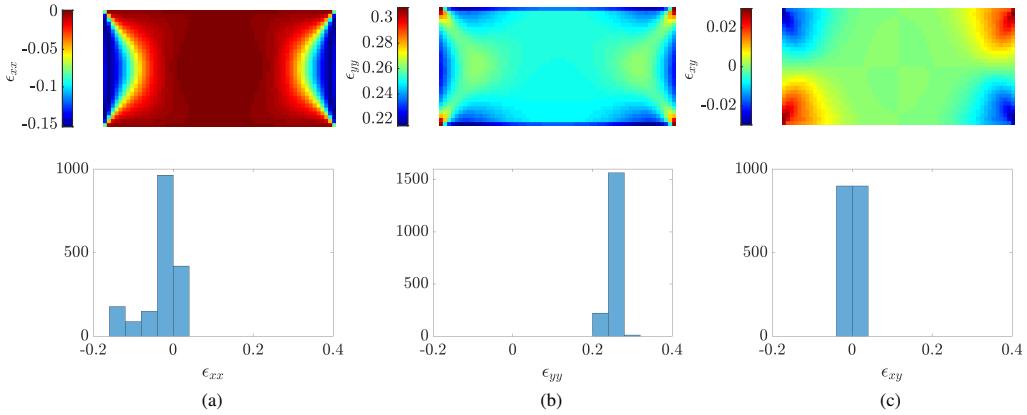

Figure 5.8: Visualization of the strain fields and histogram plots of ϵ_{xx}, ϵ_{yy}, and ϵ_{xy} at 25% strain of the monolayer stretch test.

structures, a capability not previously documented in the literature for applications in cell mechanics simulations. We will provide an example illustrating how this 3D structure can be used to capture the mechanics of a multicellular spheroid.

Multicellular spheroid

Studies show that tumor growth under constrained conditions decreases cell proliferation and induces apoptosis in a non-uniform manner [18, 24, 56]. Spherical

aggregates of cells mimicking a tumor, or multicellular spheroids (MCSs), are reported to exhibit a two- to six-fold increase in cell density near their geometric center [160]. This heightened crowding in the subcellular environment can result in a decrease in cellular rearrangement liberty, which in turn correlates to hampered proliferation [27].

To understand such cellular phenotypic heterogeneity, Dolega et al. [27] experimentally studied the stress distribution inside MCSs of malignant murine colon cancer cells under osmotic pressure, mimicking a growth-constrained environment. Their study shows non-trivial stress patterns within the MCS, with a pressure rise towards the core, thus suggesting a direct link to the lack of proliferation near the spheroid's center.

To capture such a heterogeneous stress distribution, we construct a 3D tensegrity model with non-uniform prestress to replicate the results observed in [27], and to relate to the non-uniform cell proliferation reported in [108]. In our 3D tensegrity model, we prescribe cellular prestress to mimic the crowding-induced stiffening effect [179] near the MCS core.

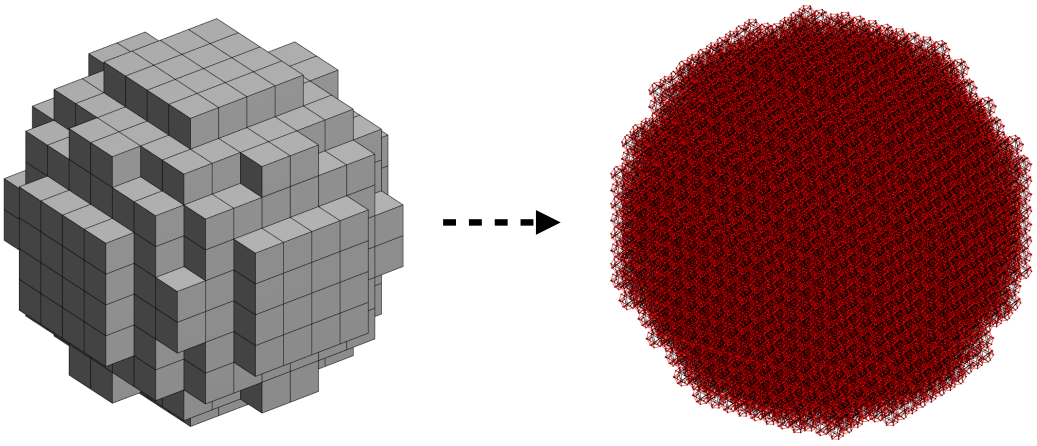

Figure 5.9: A spheroid constructed using 3D tensegrity building blocks. The left image shows a gray voxelated sphere. This representation illustrates how the spheroid is initially constructed. Each individual block in this voxelated sphere is then replaced with a 3D tensegrity building block to create the final structure shown on the right.

We initiate a voxelated sphere-like aggregate as shown in Figure 5.9. Each cube from the left blocky sphere represents a 3D translational building block in Figure 5.3b. To simulate more cellular stiffening towards the core, we assume increasing com-

pressive forces in bar elements for each building block as a function of the radial position of the block within the MCS (Figure 5.10). The balancing forces in the rest of the elements are calculated via procedures explained in Section 5.2. This non-uniform assignment of initial forcing in each building block consequently changes the stiffness across the MCS according to Equations 5.15 and 5.16.

We then prescribe an isotropic stress to the MCS and plot the normalized radial stress profile $\hat{\sigma}_{rr}$ with respect to the normalized radial position $\hat{r}$. As seen in Figure 5.11a, upon an assumed initial bar force specification f_{b} and corresponding member forces calculated using Equations 5.28 and 5.34, the resulting rate of change of $\hat{\sigma}_{rr}$ is in good alignment with the experimental result. In Figure 5.11b, we visualize the normalized radial stress of the middle slice of the MCS and overlay it with an experimental image from [108], where Ki-67 (a proliferation marker) is immunostained. We observe that the regions of high radial stress near the center of the numerical MCS overlap well with the low proliferation regions within the experimentally tested cell, visually highlighting the clear correlation between stress and cell proliferation. This result suggests that our model can be used to simulate the stress distribution within a 3D MCS, showcasing its potential as a tool for studying the correlative effects of mechanical behavior on cellular functionalities.

Discussion

Overall, we observe good agreement between our simulated results and published experimental data using the proposed tensegrity model, particularly at low (but not infinitesimal) strain values. However, at high strain values, such as those exceeding 25% in the uniaxial tension test, the simulated results fall out of the experimental envelope. There could be multiple factors contributing to this discrepancy. One factor is that our model could be oversimplified and based on limiting assumptions. For example, we assume the bars and tendons are linearly elastic, whereas, in reality, actin filaments and microtubules are reported to exhibit nonlinear material behaviors [63]. Additionally, the present model cannot simulate the complex cellular-level mechanics occurring at high strain values, such as detachment of focal adhesion, cell rupture etc.

Since we use pin-pin connections between neighboring tensegrity cells, our model must be constructed in an orderly manner, which prevents anisotropic orientation in the initiation of the cells. Additionally, the shape of the elementary tensegrity unit needs to be carefully designed to ensure that its members reach equilibrium. This is

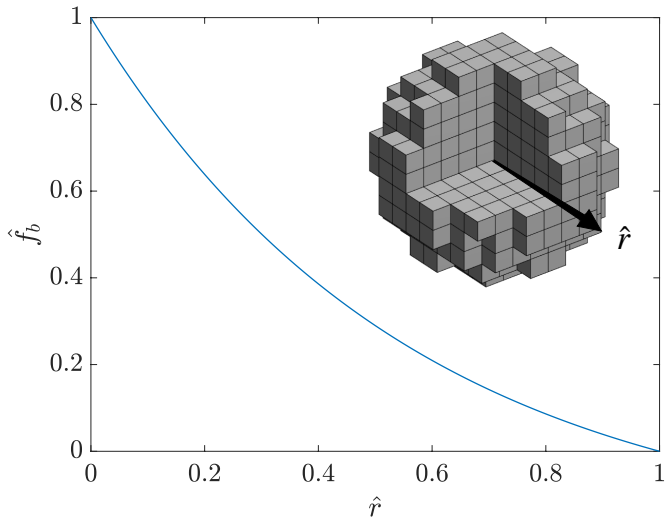

Figure 5.10: Normalized initial bar force vs. normalized radial position. Bar forces are normalized with respect to the maximal bar force, which is at the center of the MCS. Radial positions are normalized by the radius of the MCS. We assume an exponential relation of the initial bar force, based on the exponential decay of distribution of cells within spheroids [160].

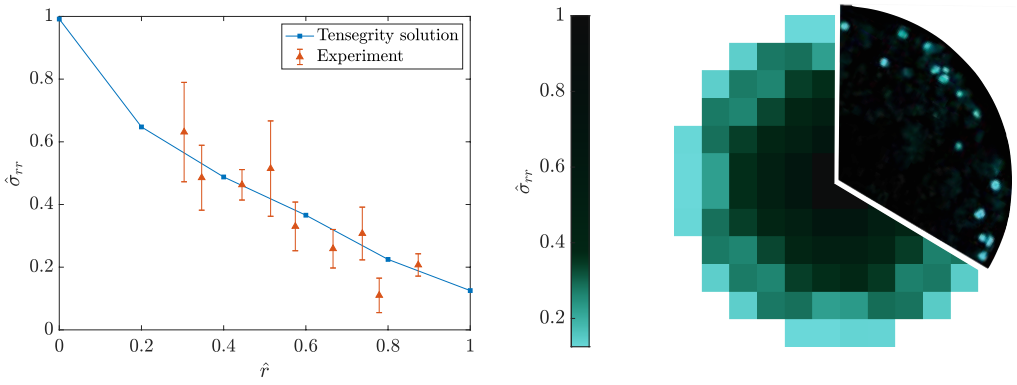

(a) (b)

Figure 5.11: Comparison of simulated results with experimental data. (a) Normalized radial stress vs. normalized radial position. σ_{rr} is normalized with respect to the maximum value. Experimental data is adapted from [27] and scaled to match with the simulated data. (b) Visualization of the normalized radial stress at the middle slice of the MCS. The top right image shows cellular proliferation along the radius in a spheroid grown under constraint, with Ki-67 immunostained [108].

a disadvantage shared by all tensegrity-based cell models. However, by relating the cell CSK to bars and tendons, we can individually assign different stiffnesses, cross-sectional areas, or even prestress levels to each tensegrity cell. This approach allows us to study the overall response of tissues while locally modulating the properties of the cell CSK.

5.4 Multiscale Data-Driven Computing with Tensegrity

Living organisms are made of millions of cells [35]. Even the monolayer used in [55] was cultured using 25000 cells. If we were to represent each cell using any abstract discrete model, be it tensegrity or others, the computational cost would increase exponentially as we increase the scale of the problem. Direct numerical simulations at full resolution can potentially pose a significant computational burden, especially considering (large) nonlinear stiffness matrices, often requiring many iterations to converge. Such limitation sets back the simplicity in simulating cell mechanics using abstract models such as the proposed tensegrity structures.

Aiming to address this problem, we adopt the data-driven (DD) computing paradigm proposed by Kirchdoerfer and Ortiz [81], which serves as a multiscale analysis tool [74] in the general context of solid mechanics. This paradigm bypasses the definition of a constitutive relation, for instance, relating stress to strain given empirical material properties. Given existing material datasets, the DD problem is formulated as a minimal distance search subject to the fundamental equilibrium and compatibility constraints. The material data can come from either simulation or experiments, rendering the DD framework free of constitutive relations, efficient in computation, and versatile in application.

In order to tackle the heavy computational burden of simulating large-scale cell mechanics using tensegrity structures, we perform a multiscale DD analysis on a monolayer with data extracted from lower-scale simulations of discrete tensegrity FEM models. Due to the limited capacity of the tensegrity model to accurately capture large deformations in cells, as discussed in Section 5.3, the present section is restricted to small deformations.

Modeling framework

We briefly summarize the infinitesimal deformation DD framework as follows. Given a body in $\mathbb{R}^{\mathrm{d}}$ discretized into N nodes and M material points, subject to external nodal forces $\boldsymbol{f}_i \in \mathbb{R}^{\mathrm{d}}$ $(i = 1, 2, \ldots, N)$, and exhibiting nodal displacements $\boldsymbol{u}_i \in \mathbb{R}^{\mathrm{d}}$ $(i = 1, 2, \ldots, N)$, the internal state is characterized by stress-strain pairs

$(\boldsymbol{\sigma}_e, \boldsymbol{\epsilon}_e)$ at each material point $e,\ e = 1, 2, \ldots, M$. Each stress-strain pair is referred to as a local phase-space coordinate $\boldsymbol{z}_e \in Z_e$, where the global phase space reads $Z = Z_1 \times Z_2 \times \cdots \times Z_M$.

Within the FEM setting, the internal state at any specific time t_k is constrained by the following equilibrium and compatibility equations:

$$\boldsymbol{\epsilon}_e^k = \boldsymbol{B}_e \boldsymbol{u}^k,\ e = 1, 2, \ldots, M\,, \tag{5.31}$$

$$\sum_{e=1}^{M} w_e \boldsymbol{B}_e^{\mathrm{T}} \boldsymbol{\sigma}_e^k = \boldsymbol{f}^k\,, \tag{5.32}$$

which define the constrain set E_k containing the *mechanical solution* at t_k:

$$E_k = \{\boldsymbol{z} \in Z \mid (5.31) \text{ and } (5.32)\}\,. \tag{5.33}$$

Instead of relating $\boldsymbol{\sigma}_e$ to $\boldsymbol{\epsilon}_e$ locally using a constitutive relation, DD introduces the global minimization problem between the constraint set E and an existing material dataset $D \subset Z$ containing the *material solution*. The distance metric can be written as

$$\|\boldsymbol{z}\| = \left(\sum_{e=1}^{M} w_e \|\boldsymbol{z}_e\|^2 \right)^{\frac{1}{2}}\,, \tag{5.34}$$

with the local distance

$$\|\boldsymbol{z}_e\| = \left(\frac{1}{2} \boldsymbol{\epsilon}_e : \mathbb{C}_e : \boldsymbol{\epsilon}_e + \frac{1}{2} \boldsymbol{\sigma}_e : \mathbb{C}_e^{-1} : \boldsymbol{\sigma}_e \right)^{\frac{1}{2}}\,. \tag{5.35}$$

Here, w_e is the weight associated with each material point, and $\mathbb{C}_e$ is a symmetric matrix serving as a purely numerical operator. The time-discrete DD problem can then be written as

$$\inf_{\boldsymbol{y} \in D_k} \inf_{\boldsymbol{z} \in E_k} \|\boldsymbol{y} - \boldsymbol{z}\|^2 = \inf_{\boldsymbol{z} \in E_k} \inf_{\boldsymbol{y} \in D_k} \|\boldsymbol{y} - \boldsymbol{z}\|^2\,. \tag{5.36}$$

This problem can be solved using fixed-point iterations, i.e., by iteratively finding the closest point projection $(\boldsymbol{\sigma}_e, \boldsymbol{\epsilon}_e)$ onto the hyperplane that satisfies Equations 5.31 and 5.32, and then finding the closest material data point $(\boldsymbol{\sigma}_e^*, \boldsymbol{\epsilon}_e^*)$. The closest point projection can be resolved using a nodal set of Lagrange multipliers $\boldsymbol{\eta}$. Then, the FEM equations of the DD problem take the form

$$\left(\sum_{e=1}^{M} w_e \boldsymbol{B}_e^{\mathrm{T}} \mathbb{C}_e \boldsymbol{B}_e \right) \boldsymbol{u} = \sum_{e=1}^{M} w_e \boldsymbol{B}_e^{\mathrm{T}} \mathbb{C}_e \boldsymbol{\epsilon}_e^*\,, \tag{5.37}$$

$$\left(\sum_{e=1}^{M} w_e \boldsymbol{B}_e^{\mathrm{T}} \mathbb{C}_e \boldsymbol{B}_e\right) \boldsymbol{\eta} = \boldsymbol{f} - \sum_{e=1}^{M} w_e \boldsymbol{B}_e^{\mathrm{T}} \boldsymbol{\sigma}_e^{*}\,, \tag{5.38}$$

$$\boldsymbol{\sigma}_e = \boldsymbol{\sigma}_e^{*} + \mathbb{C}_e \sum_{i=1}^{N} \boldsymbol{B}_{ei} \boldsymbol{\eta}_i\,. \tag{5.39}$$

Readers are referred to, e.g., [74, 81] for further details.

Monolayer tests

We proceed to use the DD framework explained above to capture the monolayer cell mechanics from Section 5.3. Noting the small-deformation scale, we consider in this section the monolayer tests up to 5% strain.

To generate a dataset, we first determine the size of the pseudo-2D RVE at which energy convergence is observed. Since the tensegrity system has a finite length along the out-of-plane (z) direction, the response of a single unit cell does not suffice. Therefore, we construct 2D models up to 6×6 cells and measure the strain energy vs. the cell size in log-log scale to test the convergence. We then select a pseudo-2D RVE of size 3×3 and perform several p-q loading paths to generate a material dataset D (Figures 5.12a–b) from the homogenized response, considering periodic boundary conditions.

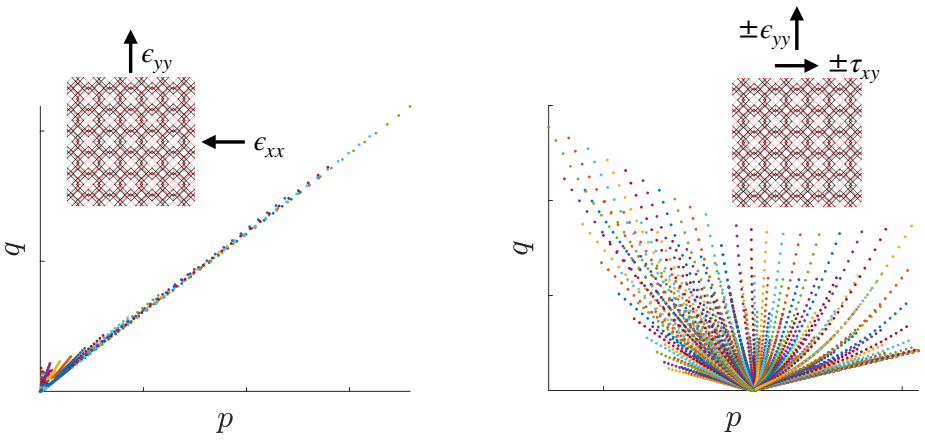

(a) (b)

Figure 5.12: p–q paths performed on the RVE.

We conduct a monolayer uniaxial stretch of 5% (Figure 5.13a) and compare the hydrostatic pressure $p = -(1/3)\mathrm{tr}(\boldsymbol{\sigma})$ predicted by the DD framework, considering

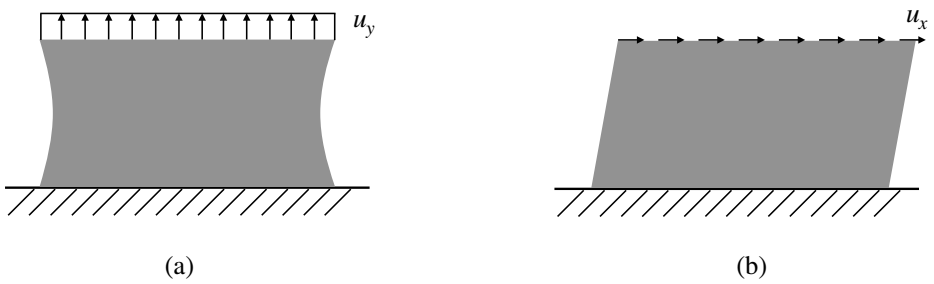

Figure 5.13: Schematic of tests performed on the tensegrity monolayer. (a) 5% strain tension test; (b) 5% strain shear test.

both the material solution and the mechanical solution, to the actual tensegrity response from the direct numerical simulation. In the tensegrity assembly, in order to be consistent with the selection of the RVE size, we take a window size of 3×3 to compute a moving average hydrostatic stress in the monolayer. The stress is then visualized with respect to the original nodal positions of the tensegrity cells. In the DD solutions, we employ a mesh with 10×20 elements, each with four nodes and four Gauss integration points.

Figure 5.14 shows a comparison of the DD material solution, the DD mechanical solution, the tensegrity solution, and the percent error map between the DD mechanical solution and the tensegrity solution. We see that the DD solutions qualitatively capture the hydrostatic pressure of the monolayer. From the error map, we see a higher percent error around the edge of the map. This is attributed to the fact that the data employed in the DD calculations was generated from RVEs with periodic boundary conditions, not fully representative of the actual boundary condition used in the direct tensegrity simulation. Other than the errors around the edges, we see an overall good agreement between the DD solution and the tensegrity solution. Figure 5.15 further shows the corresponding force-displacement curves, which reveals that the global non-linear response is captured well.

To assess the dependence of the DD simulations on the number of data points, we plot, for different dataset sizes, the relative error between the hydrostatic pressure from the DD solution and the reference hydrostatic pressure from the direct numerical simulation. The outermost boundary cells are excluded from this calculation. To obtain different dataset sizes, we shuffle and randomly sample varying numbers

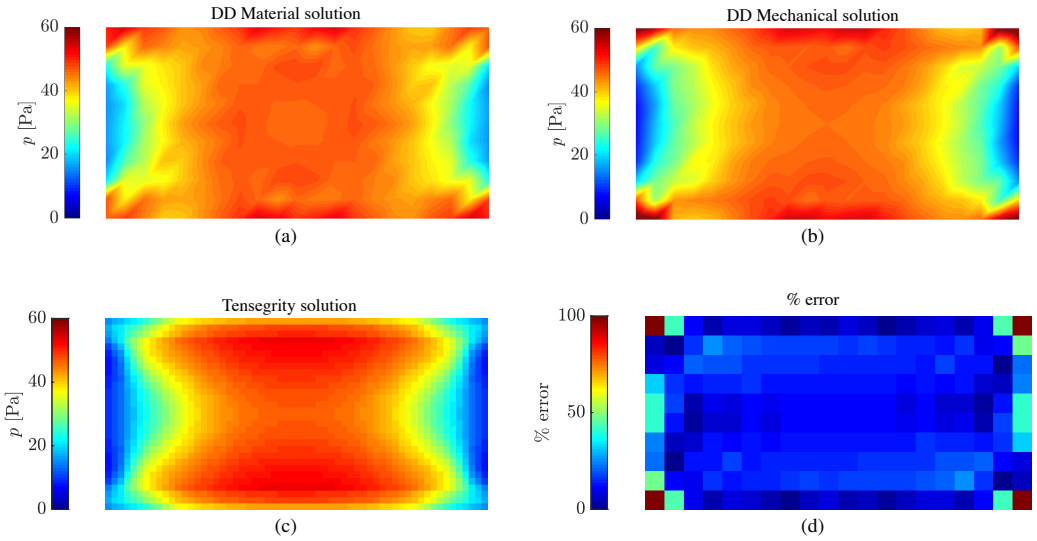

Figure 5.14: Hydrostatic pressure field of (a) DD material solution, (b) DD mechanical solution, (c) tensegrity solution, and (d) relative error.

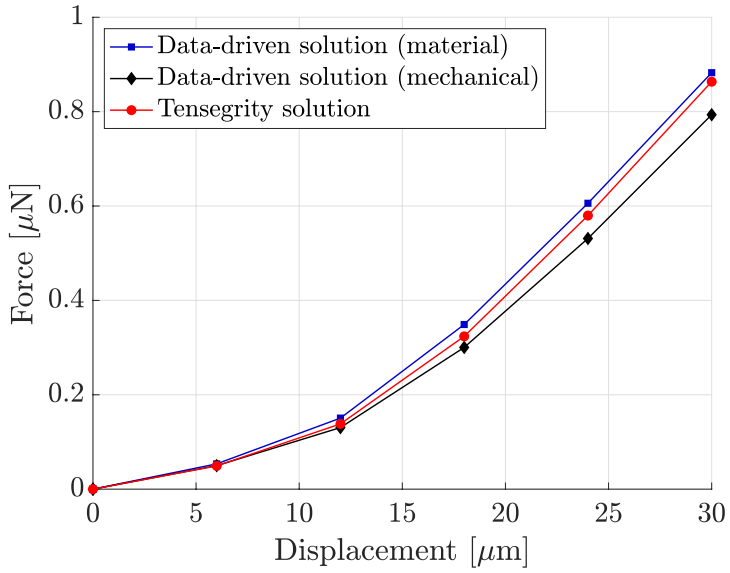

Figure 5.15: Force vs. displacement obtained on the top edge of the monolayer.

of data points. For each dataset size, we compute the average error over five trials. In Figure 5.16a, we observe that the accuracy increases with dataset size, with the final relative errors below 15% for both material and mechanical solutions.

We also calculate the distance between the material solution $\boldsymbol{y}_{\text{mat}}$ and the mechan-

ical solution $\boldsymbol{y}_{\text{mec}}$ using Equations 5.34 and 5.35, normalized with the norm of mechanical solution. We then take the average among five trials and plot the result for different dataset sizes in Figure 5.16b. We observe that as the dataset size increases, the normalized distance between the DD solutions decreases to a final value of ~0.07. As a reference, we also plot the normalized distance obtained using self-consistent DD, where we sample directly from the reference tensegrity response (direct numerical simulation) at the same location. The general DD solution yields an error value only 2% higher than this benchmark, highlighting the reliability of the data sampled from the RVEs.

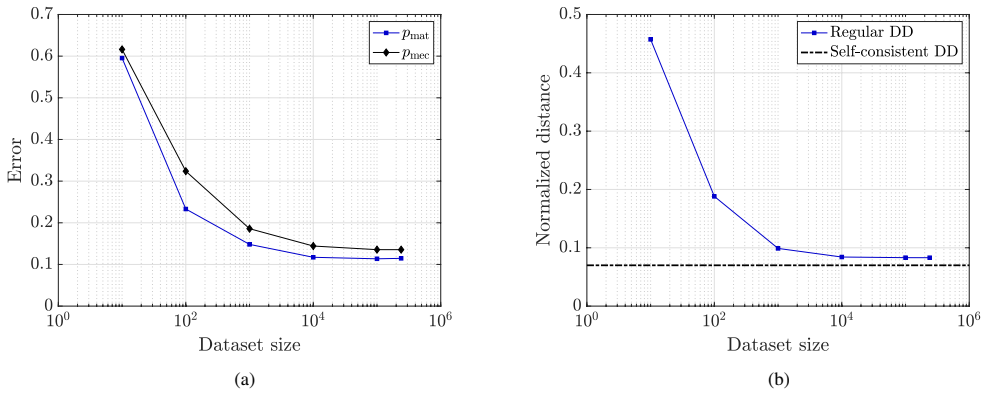

Figure 5.16: Effect of dataset size on resulting error in tension test. (a) Relative error between $p_{\square}$ and p_{tsg} vs. dataset size. The relative error is calculated as $(p_{\square} - p_{\text{tsg}})/p_{\text{tsg}}$. The $\square$ subscript represents either the DD material or mechanical solution. The value is averaged among five trials. Boundary cells are excluded from the calculation. (b) Normalized distance vs. dataset size. The normalized distance is calculated as $(\|\mathbf{y}_{\text{mat}} - \mathbf{y}_{\text{mec}}\|)/\|\mathbf{y}_{\text{mec}}\|$. The error values are averaged among five trials. The dotted line shows the benchmark distance calculated using self-consistent DD.

Similarly, we conduct a monolayer simple shear test of 5% strain (Figure 5.13b) and compute the average effective stress $q = \sqrt{(3/2)\boldsymbol{s} : \boldsymbol{s}}$, with the stress deviator, $\boldsymbol{s} = \boldsymbol{\sigma} + p\boldsymbol{I}$. The results of the DD simulation are shown in Figure 5.17 and compared to the reference tensegrity response. Other than the large error along the edges, again due to the discrepancy in the periodic boundary conditions applied to the RVEs, the DD solutions show good agreement with the tensegrity response from the direct numerical simulation.

Furthermore, Figure 5.18a shows the relative error between the DD solutions and

the direct numerical simulation in terms of q, for different dataset sizes, while Figure 5.18b shows the normalized distance between $\boldsymbol{y}_{\text{mat}}$ and $\boldsymbol{y}_{\text{mec}}$. Again, we observe that both the relative error and the normalized distance decrease as the dataset size increases. The normalized distance is 6% higher than the benchmark calculated using self-consistent DD, indicating that the material data sampled from the RVEs covers most of the phase-space region spanned by the tensegrity structure, although less accurately than in the stretch test.

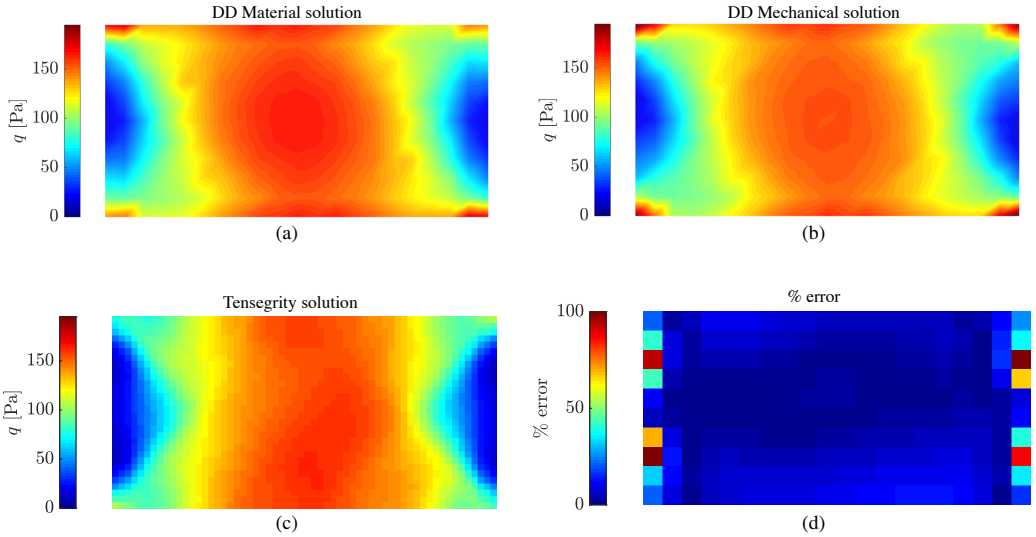

Figure 5.17: Deviatoric stress field of (a) DD material solution, (b) DD mechanical solution, (c) tensegrity solution, and (d) relative error.

Discussion

The accuracy of the DD algorithm depends on how well the sampled material data spans the desired phase-space region. We suspect several reasons for the observed differences between the DD mechanical solution, the DD material solution, and the direct tensegrity response.

First, we consider the potential mismatch introduced by the boundary conditions and the dimensionality of the problem. In the DD framework, we use a simplified 2D plane-stress formulation. However, the proposed tensegrity structure is 3D. Although the thickness of the tensegrity monolayer is less than 4% compared to the width of the sample, this discrepancy could still introduce some error. Additionally, the material dataset is sampled from RVEs under periodic boundary conditions, which do not accurately represent the boundary conditions of the tensegrity mono-

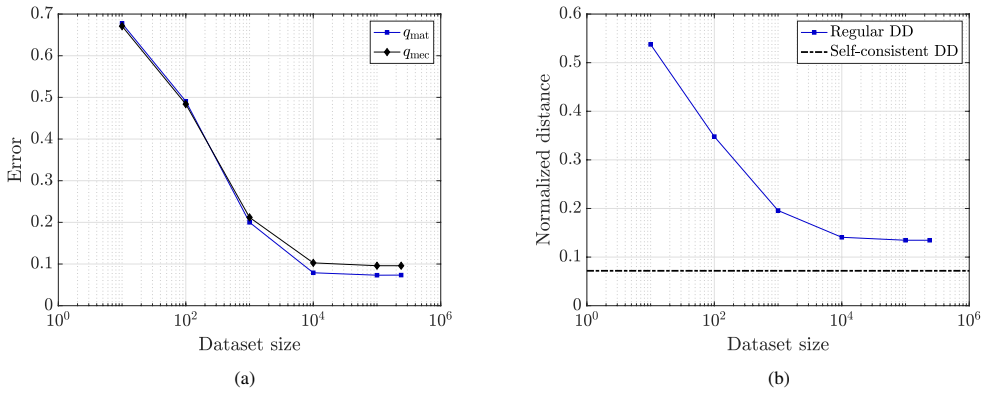

Figure 5.18: Effect of dataset size on resulting error in shear test. (a) Averaged relative error between $q_{\square}$ and q_{tsg} vs. dataset size. (b) Normalized distance vs. dataset size. Benchmark norm distance calculated using self-consistent DD is shown in dotted line.

layer. Although we exclude the outermost boundary cells when calculating the errors, the boundary effect cannot be entirely eliminated.

Second, we suspect that non-simple mechanisms, such as those described by micromorphic or micropolar theories [37], are significant in the proposed tensegrity structure. As the structure deforms, the angle of the twisted side faces varies, which cannot be captured by the 2D, isotropic, Cauchy continua-based data-driven framework. In fact, in Figure 5.16b and Figure 5.18b, we observe around a 10% normalized distance between $\boldsymbol{y}_{\text{mat}}$ and $\boldsymbol{y}_{\text{mec}}$ in the stretch and shear tests using self-consistent DD. This indicates that even when sampling directly from the actual tensegrity response, the material solution still presents a 10% difference from the mechanical solution based on an equilibrated Cauchy stress. This result suggests that the proposed tensegrity structure exhibits nontrivial kinematics and kinetics, not captured by standard Cauchy continua.

5.5 Conclusion

In this chapter, we propose a 3D multicellular tensegrity structure for simulating cell mechanics. We demonstrate that this model can capture the response of single cells and multicellular monolayers. Moreover, we describe the 3D heterogeneous stress distribution within an MCS by assigning non-uniform initial prestress to the tensegrity building blocks. This capability positions the model as a potential tool for studying more advanced cellular processes, such as mechanotransduction [59, 153].

The synergistic interplay of the CSK is indispensable for cellular functionalities. The ability of the tensegrity model to link mechanical forces to specific load-bearing members in 3D can potentially shed new light on the CSK rearrangements and their effects on cellular physiological functions, potentially bridging an important step toward understanding tissue mechanics and its fundamental role in health and disease [7, 36].

We also introduce a DD framework for continuum cell mechanics simulations in small deformations. Overall, DD solutions are in good agreement with the tensegrity solution. In general, the material dataset D can be populated using lower-scale simulations as shown in Section 5.4, or even extracted from existing numerical solutions or experimental data. In this way, DD bypasses the need for a parameter-based continuum model, directly formulating the macroscopic cell mechanics problem based on material data. Combined with homogenization techniques, DD computing may yield accurate results from multiscale analysis while ensuring computational efficiency. However, given the non-standard mechanics suspected to be present in the tensegrity structures, recent extensions of the DD framework to generalized continua [73, 159] could be applied in future work. This new DD-based framework could pave the path for studying the mechanobiology of large scale cellular structures, including organs.

Chapter 6

CONCLUSION AND FUTURE OUTLOOK

6.1 Conclusion

This thesis developed accurate and efficient computational models for three distinct case studies, advancing the role of computational modeling from a validation tool to an exploratory framework.

In Chapter 3, LS-DEM and LMGC90 demonstrated good agreement in capturing the kinematic profiles of discrete multiblock structures when compared with experimental results. Among the four tested concrete configurations, taller and more complex configurations, such as Configurations 3 and 4, exhibited more pronounced rocking and/or sliding behaviors, consistent with experimental observations. This study introduced an efficient framework for running Monte Carlo simulations on discrete systems, yielding stable estimates with low variability. The proposed framework enables researchers to benchmark known behaviors of discrete structures and predict the responses of configurations beyond the practical limits of experimental testing.

In Chapter 4, an actuatable TIM system composed of woven truncated tetrahedron particles was introduced. Experimental and numerical investigations revealed that both high friction and large contact area between neighboring particles positively influence the system's bending resistance. The effect of friction on bending stiffness diminishes as the friction coefficient increases, whereas the projected horizontal contact area enhances the bending modulus in a linear manner. By employing validated computational models, this study bridged micro-scale mechanics to macro-scale structural responses.

In Chapter 5, a 3D multicellular tensegrity structure was developed to simulate cell mechanics. This structure effectively captured the deformation responses of single cells in indentation tests, monolayers in stretch tests, and the heterogeneous stress distribution of MCSs under osmotic pressure. Additionally, a DD framework with multiscale analysis was implemented for efficient simulations at small deformations. The DD framework produced accurate results while circumventing the need for parameter-dependent continuum models, directly formulating macroscopic cell mechanics problems based on material data. By integrating the tensegrity model and the DD framework, this study leveraged predictive modeling to elucidate the

complex behaviors of biological systems.

Collectively, these case studies highlight the power of predictive modeling in expanding our understanding of architected solids beyond experimental constraints. The models developed in this thesis have demonstrated their ability to overcome experimental limitations by simulating configurations and design spaces that are impractical or impossible to test physically. Whether predicting the seismic response of multiblock structures, capturing the mechanics of TIMs, or modeling multicellular tensegrity systems, these models provide critical insights where physical experimentation alone is insufficient.

Beyond replicating known behaviors, these computational models have also played a crucial role in uncovering fundamental structure-property relationships. By analyzing geometry, material properties, and macroscopic responses, this work has revealed key mechanisms governing mechanical behavior that were not readily accessible through experiments alone. In particular, simulations of woven TIMs identified how friction and contact area influence bending stiffness, while tensegrity-based cell mechanics models provided insights into cell proliferation through simulating stress distributions across biological structures. These findings offer valuable guidance for designing and understanding materials and systems.

Spanning multiple length scales, the predictive models developed in this thesis offer a robust foundation for studying architected solids and can be further applied across a broad spectrum of engineering and scientific applications.

6.2 Outlook

The research presented in this thesis paves the way for numerous opportunities to deepen our understanding and control of architected solids. These studies demonstrated remarkable capabilities of numerical modeling to accurately capture the behaviors of discrete multiblock structures, TIMs, and complex biological systems. With these predictive tools, novel shapes and arrangements of architected structures can be designed and systematically explored to understand how variations in geometry and constituent configurations influence macroscopic properties.

For instance, the numerical models developed in Chapter 3 could offer insights into how the shapes and arrangements of individual concrete blocks impact the structure's resistance to seismic perturbations. In Chapter 4, computational tools could guide the design of TIM systems to achieve specific performance objectives, such as enhancing bending stiffness or optimizing energy dissipation. The models in

Chapter 5 could be extended to large-scale biological systems, leveraging tensegrity structures to investigate how internal properties — such as polymer stiffness — affect cellular processes in mechanotransduction and mechanobiology.

Additionally, advances in machine learning and data-driven computing offer new avenues to accelerate and enhance physics-based modeling. Thus far, our modeling framework has primarily been one-directional: given a particular structure or material, we can simulate its properties and responses, but using these results to inform design remains challenging. By integrating machine learning approaches with physics-based models, we can transition from a purely predictive framework to a more iterative and exploratory design process. Key features within the design space can be identified and leveraged to automate the generation of novel shapes and arrangements.

For instance, with a sufficiently large dataset of TIM designs, a Variational Autoencoder (VAE) could extract critical design features through latent space encoding. These features could then be decoded to reconstruct existing shapes or generate entirely new designs. Additionally, neural networks (NN) could learn from this encoded information to uncover hidden relationships, directly linking design features to macroscopic mechanical properties.

Overall, these advancements underscore the transformative potential of computational modeling as a cornerstone for the design, analysis, and discovery of architected solids across diverse engineering and scientific fields.

Bibliography

[1] P. Aejmelaeus-Lindström, J. Willmann, S. Tibbits, F. Gramazio, and M. Kohler. Jammed architectural structures: Towards large-scale reversible construction. *Granular Matter*, 18, 04 2016.

[2] N. Ambraseys, P. Smit, R. Sigbjornsson, P. Suhadolc, and B. Margaris. *Internet-Site for European Strong-Motion Data*. European Commission, Research-Directorate General, Environment and Climate Programme, 2002.

[3] J. E. Andrade, A. J. Rosakis, J. P. Conte, J. I. Restrepo, V. Gabuchian, J. M. Harmon, A. Rodriguez, A. Nema, and A. R. Pedretti. A framework to assess the seismic performance of multiblock tower structures as gravity energy storage systems. *Journal of Engineering Mechanics*, 149(1):04022085, 2023.

[4] M. Aslam, W. G. Godden, and D. Theodore Scalise. Earthquake rocking response of rigid bodies. *Journal of the Structural Division*, 106(2):377–392, 1980.

[5] Sinopoli A. Augusti, G. Modelling the dynamics of large block structures. *Meccanica*, 27:195–211, 1992.

[6] F. Barthelat. Architectured materials in engineering and biology: Fabrication, structure, mechanics and performance. *International Materials Reviews*, 60 (8):413–430, 2015.

[7] Y. Bashirzadeh and A. P. Liu. Encapsulation of the cytoskeleton: Towards mimicking the mechanics of a cell. *Soft Matter*, 15:8425–8436, 2019.

[8] A. Bejarano and C. Hoffmann. A generalized framework for designing topological interlocking configurations. *International Journal of Architectural Computing*, 17(1):53–73, 2019.

[9] L. Berto, A. Saetta, R. Scotta, and R. Vitaliani. An orthotropic damage model for masonry structures. *International Journal for Numerical Methods in Engineering*, 55(2):127–157, 2002.

[10] J. G. Betts, K. A. Young, J. A. Wise, E. Johnson, B. Poe, D. H. Kruse, O. Korol, J. E. Johnson, M. Womble, and P. DeSaix. *Anatomy and Physiology*. OpenStax, 2013.

[11] C. Brugger, Y. Bréchet, and M. Fivel. Experiments and numerical simulations of interlocked materials. *Advanced Materials Research*, 47:125–128, 2008.

[12] C. Brugger, M. C. Fivel, and Y. Brechet. Numerical simulations of topologically interlocked materials coupling dem methods and fem calculations: Comparison with indentation experiments. *MRS Online Proceedings Library*, 1188(1):106–111, 2009.

[13] K. Caluwaerts, J. Despraz, A. Işçen, A. P. Sabelhaus, J. Bruce, B. Schrauwen, and V. SunSpiral. Design and control of compliant tensegrity robots through simulation and hardware validation. *Journal of the Royal Society Interface*, 11(98):20140520, 2014.

[14] M. Carlesso, R. Giacomelli, T. Krause, A. Molotnikov, D. Koch, S. Kroll, K. Tushtev, Y. Estrin, and K. Rezwan. Improvement of sound absorption and flexural compliance of porous alumina-mullite ceramics by engineering the microstructure and segmentation into topologically interlocked blocks. *Journal of the European Ceramic Society*, 33(13-14):2549–2558, 2013.

[15] P. Carrara, L. De Lorenzis, L. Stainier, and M. Ortiz. Data-driven fracture mechanics. *Computer Methods in Applied Mechanics and Engineering*, 372: 113390, 2020.

[16] M. N. Chatzis and A. W. Smyth. Modeling of the 3d rocking problem. *International Journal of Non-Linear Mechanics*, 47(4):85–98, 2012.

[17] T. Chen, C. Wu, and F. Su. Mechanical models of the cellular cytoskeletal network for the analysis of intracellular mechanical properties and force distributions: A review. *Medical Engineering Physics*, 34(10):1375–1386, 2012.

[18] G. Cheng, J. Tse, R. K. Jain, and L. L. Munn. Micro-environmental mechanical stress controls tumor spheroid size and morphology by suppressing proliferation and inducing apoptosis in cancer cells. *PLoS ONE*, 4, 2009.

[19] B. Chetouane, F. Dubois, M. Vinches, and C. Bohatier. Nscd discrete element method for modelling masonry structures. *International Journal for Numerical Methods in Engineering*, 64(1):65–94, 2005.

[20] F. Chowdhury, B. Huang, and N. Wang. Cytoskeletal prestress: The cellular hallmark in mechanobiology and mechanomedicine. *Cytoskeleton*, 78(6): 249–276, 2021.

[21] J. Christoffersen, M. M. Mehrabadi, and S. Nemat-Nasser. A micromechanical description of granular material behavior. *Journal of Applied Mechanics*, 48(2):339–344, 06 1981.

[22] P. A. Cundall. Formulation of a three-dimensional distinct element model—Part I. A scheme to detect and represent contacts in a system composed of many polyhedral blocks. *International Journal of Rock Mechanics and Mining Sciences & Geomechanics Abstracts*, 25(3):107–116, 1988.

[23] A. S. Dalaq and F. Barthelat. Manipulating the geometry of architectured beams for maximum toughness and strength. *Materials Design*, 194:108889, 2020.

[24] M. Delarue, F. Montel, D. Vignjevic, J. Prost, J. Joanny, and G. Cappello. Compressive stress inhibits proliferation in tumor spheroids through a volume limitation. *Biophysical Journal*, 107(8):1821–1828, 2014.

[25] E. G. Dimitrakopoulos and M. J. DeJong. Revisiting the rocking block: Closed-form solutions and similarity laws. *Proceedings of the Royal Society A: Mathematical, Physical and Engineering Sciences*, 468(2144):2294–2318, 2012.

[26] L. Djumas, G. P. Simon, Y. Estrin, and A. Molotnikov. Deformation mechanics of non-planar topologically interlocked assemblies with structural hierarchy and varying geometry. *Scientific Reports*, 7(1):11844, 2017.

[27] M. E. Dolega, M. Delarue, F. Ingremeau, J. Prost, A. Delon, and G. Cappello. Cell-like pressure sensors reveal increase of mechanical stress towards the core of multicellular spheroids under compression. *Nature Communications*, 8, 2017.

[28] F. Donze, V. Richefeu, and S. Magnier. Advances in discrete element method applied to soil, rock and concrete mechanics. *Electronic Journal of Geotechnical Engineering*, 8, 01 2009.

[29] F. Dubois, V. Acary, and M. Jean. The contact dynamics method: A nonsmooth story. *Comptes Rendus Mécanique*, 346(3):247–262, 2018.

[30] M. Dugue, M. Fivel, Y. Bréchet, and R. Dendievel. Indentation of interlocked assemblies: 3D discrete simulations and experiments. *Computational Materials Science*, 79:591–598, 2013.

[31] A. V. Dyskin, Y. Estrin, A. J. Kanel-Belov, and E. Pasternak. A new concept in design of materials and structures: Assemblies of interlocked tetrahedron-shaped elements. *Scripta Materialia*, 44(12):2689–2694, 2001.

[32] A. V. Dyskin, Y. Estrin, A. J. Kanel-Belov, and E. Pasternak. Toughening by fragmentation—How topology helps. *Advanced Engineering Materials*, 3(11):885–888, 2001.

[33] A. V. Dyskin, Y. Estrin, A. J. Kanel-Belov, and E. Pasternak. Topological interlocking of platonic solids: A way to new materials and structures. *Philosophical Magazine Letters*, 83(3):197–203, 2003.

[34] A. V. Dyskin, Y. Estrin, E. Pasternak, H. C. Khor, and A. J. Kanel-Belov. The principle of topological interlocking in extraterrestrial construction. *Acta Astronautica*, 57(1):10–21, 2005.

[35] F. Facchin A. Beraudi R. Casadei F. Frabetti L. Vitale M. C. Pelleri S. Tassani F. Piva S. Perez-Amodio P. Strippoli E. Bianconi, A. Piovesan and S. Canaider. An estimation of the number of cells in the human body. *Annals of Human Biology*, 40(6):463–471, 2013.

[36] Y. M. Efremov, I. M. Zurina, V. S. Presniakova, N. V. Kosheleva, D. V. Butnaru, A. A. Svistunov, Y. A. Rochev, and P. S. Timashev. Mechanical properties of cell sheets and spheroids: The link between single cells and complex tissues. *Biophysical Reviews*, 13(4), 2021.

[37] A. C. Eringen and E. S. Suhubi. Nonlinear theory of simple micro-elastic solids—I. *International Journal of Engineering Science*, 2:189–203, 1964.

[38] Y. Estrin, A. V. Dyskin, and E. Pasternak. Topological interlocking as a material design concept. *Materials Science and Engineering: C*, 31(6): 1189–1194, 2011.

[39] Y. Estrin, Y. Beygelzimer, R. Kulagin, P. Gumbsch, P. Fratzl, Y. Zhu, and H. Hahn. Architecturing materials at mesoscale: Some current trends. *Materials Research Letters*, 9(10):399–421, 2021.

[40] Y. Estrin, V. R. Krishnamurthy, and E. Akleman. Design of architectured materials based on topological and geometrical interlocking. *Journal of Materials Research and Technology*, 15:1165–1178, 2021.

[41] S. Feldfogel, K. Karapiperis, J. E. Andrade, and D. S. Kammer. Scaling, saturation, and upper bounds in the failure of topologically interlocked structures. *International Journal of Solids and Structures*, 269:112228, 2023.

[42] S. Feldfogel, K. Karapiperis, J. E. Andrade, and D. S. Kammer. Failure of topologically interlocked structures—A level-set-dem approach. *European Journal of Mechanics - A/Solids*, 103:105156, 2024.

[43] Y. Feng, T. Siegmund, E. Habtour, and J. Riddick. Impact mechanics of topologically interlocked material assemblies. *International Journal of Impact Engineering*, 75:140–149, 2015.

[44] Y. Feng, X. Yuan, and A. Samy. Analysis of new wave-curved tensegrity dome. *Engineering Structures*, 250:113408, 2022.

[45] A. G. Fletcher, J. M. Osborne, P. K. Maini, and D. J. Gavaghan. Implementing vertex dynamics models of cell populations in biology within a consistent computational framework. *Progress in Biophysics and Molecular Biology*, 113(2):299–326, 2013.

[46] A. G. Fletcher, M. Osterfield, R. E. Baker, and S. Y. Shvartsman. Vertex models of epithelial morphogenesis. *Biophysical Journal*, 106(11):2291–2304, 2014.

[47] D. Fletcher and R. Mullins. Cell mechanics and the cytoskeleton. *Nature*, 463:485–492, 2010.

[48] B. Fuller. Tensegrity. *Portfolio Artnews Annual*, 4, 1961.

[49] W. Gilewski, J. Kłosowska, and P. Obara. Applications of tensegrity structures in civil engineering. *Procedia Engineering*, 111:242–248, 2015.

[50] F. Gittes, B. Mickey, J. Nettleton, and J. Howard. Flexural rigidity of microtubules and actin filaments measured from thermal fluctuations in shape. *Journal of Cell Biology*, 120(4):923–934, 02 1993.

[51] J. R. Greer and V. S. Deshpande. Three-dimensional architected materials and structures: Design, fabrication, and mechanical behavior. *MRS Bulletin*, 44:750–757, 2019.

[52] M. Gómez-González, E. Latorre, M. Arroyo, and X. Trepat. Measuring mechanical stress in living tissues. *Nature Reviews Physics*, 2:300–317, 2020.

[53] J. M. Harmon, V. Gabuchian, A. J. Rosakis, J. P. Conte, J. I. Restrepo, A. Rodriguez, A. Nema, A. R. Pedretti, and J. E. Andrade. Predicting the seismic behavior of multiblock tower structures using the level set discrete element method. *Earthquake Engineering & Structural Dynamics*, 52(9): 2577–2596, 2023.

[54] A. R. Harris and G. T. Charras. Experimental validation of atomic force microscopy-based cell elasticity measurements. *Nanotechnology*, 22(34): 345102, 2011.

[55] A. R. Harris, L. Peter, J. Bellis, B. Baum, A. J. Kabla, and G. T. Charras. Characterizing the mechanics of cultured cell monolayers. *Proceedings of the National Academy of Sciences*, 109(41):16449–16454, 2012.

[56] G. Helmlinger, P. A. Netti, H. C. Lichtenbeld, R. J. Melder, and R. K. Jain. Solid stress inhibits the growth of multicellular tumor spheroids. *Nature Biotechnology*, 15, 1997.

[57] J. Hohe and W. Becker. Effective stress-strain relations for two-dimensional cellular sandwich cores: Homogenization, material models, and properties. *Applied Mechanics Reviews*, 55(1):61–87, 08 2001.

[58] T. Hohmann and F. Dehghani. The cytoskeleton—A complex interacting meshwork. *Cells*, 8, 2019.

[59] S. Hu, J. Chen, B. Fabry, Y. Numaguchi, A. Gouldstone, D. E. Ingber, J. J. Fredberg, J. P. Butler, and N. Wang. Intracellular stress tomography reveals stress focusing and structural anisotropy in cytoskeleton of living cells. *American Journal of Physiology-Cell Physiology*, 285(5):C1082–C1090, 2003.

[60] S. Huang, C. S. Chen, and D. E. Ingber. Control of cyclin d1, p27kip1, and cell cycle progression in human capillary endothelial cells by cell shape and cytoskeletal tension. *Molecular Biology of the Cell*, 9(11):3179–3193, 1998.

[61] Y. Hurmuzlu and D. B. Marghitu. Rigid body collisions of planar kinematic chains with multiple contact points. *The International Journal of Robotics Research*, 13(1):82–92, 1994.

[62] D. E. Ingber. From tensegrity to human organs-on-chips: Implications for mechanobiology and mechanotherapeutics. *Biochemical Journal*, 480: 243–257, 2023.

[63] D. E. Ingber, N. Wang, and D. Stamenović. Tensegrity, cellular biophysics, and the mechanics of living systems. *Reports on Progress in Physics*, 77(4): 046603, apr 2014.

[64] Y. Ishiyama. Motions of rigid bodies and criteria for overturning by earthquake excitations. *Earthquake Engineering & Structural Dynamics*, 10(5): 635–650, 1982.

[65] E. Jager, E. Smela, and O. Inganas. Microfabricating conjugated polymer actuators. *Science*, 290(5496):1540–1545, 2000.

[66] M. Jean. The non-smooth contact dynamics method. *Computer Methods in Applied Mechanics and Engineering*, 177(3):235–257, 1999.

[67] *JCSS Probabilistic Model Code Part 3: Material Properties*. Joint Committee on Structural Safety, 2000.

[68] *JCSS Probabilistic Model Code Part 2: Load Models*. Joint Committee on Structural Safety, 2001.

[69] H. Kan, H. S. Udaykumar, W. Shyy, and R. Tran-Son-Tay. Hydrodynamics of a compound drop with application to leukocyte modeling. *Physics of Fluids*, 10(4):760–774, 1998.

[70] M. F. Kaplan. *Concrete Radiation Shielding: Nuclear Physics, Concrete Properties, Design and Construction*. John Wiley & Sons, New York, 1989.

[71] A. Karabchevsky, A. Katiyi, A. S. Ang, and A. Hazan. On-chip nanophotonics and future challenges. *Nanophotonics*, 9(12):3733–3753, 2020.

[72] K. Karapiperis and J. E. Andrade. Nonlocality in granular complex networks: Linking topology, kinematics and forces. *Extreme Mechanics Letters*, 42: 101041, 2021.

[73] K. Karapiperis, M. Ortiz, and J. E. Andrade. Data-driven nonlocal mechanics: Discovering the internal length scales of materials. *Computer Methods in Applied Mechanics and Engineering*, 386:114039, 2021.

[74] K. Karapiperis, L. Stainier, M. Ortiz, and J. E. Andrade. Data-driven multiscale modeling in mechanics. *Journal of the Mechanics and Physics of Solids*, 147:104239, 2021.

[75] K. Karapiperis, S. Monfared, R. B. Macedo, S. Richardson, and J. E. Andrade. Stress transmission in entangled granular structures. *Granular Matter*, 24(3): 91, 2022.

[76] R. Kawamoto, E. Andò, G. Viggiani, and J. E. Andrade. Level set discrete element method for three-dimensional computations with triaxial case study. *Journal of the Mechanics and Physics of Solids*, 91:1–13, 2016.

[77] R. Kawamoto, J. E. Andrade, and T. Matsushima. A 3-d mechanics-based particle shape index for granular materials. *Mechanics Research Communications*, 92:67–73, 2018.

[78] S. Khandelwal, T. Siegmund, R. J. Cipra, and J. S. Bolton. Transverse loading of cellular topologically interlocked materials. *International Journal of Solids and Structures*, 49(18):2394–2403, 2012.

[79] S. Khandelwal, T. Siegmund, R. J. Cipra, and J. S. Bolton. Adaptive mechanical properties of topologically interlocking material systems. *Smart Materials and Structures*, 24(4):045037, mar 2015.

[80] D. Y. Kim and T. Siegmund. Mechanics and design of topologically interlocked irregular quadrilateral tessellations. *Materials Design*, 212:110155, 2021.

[81] T. Kirchdoerfer and M. Ortiz. Data-driven computational mechanics. *Computer Methods in Applied Mechanics and Engineering*, 304:81–101, 2016.

[82] T. Kirchdoerfer and M. Ortiz. Data-driven computing in dynamics. *International Journal for Numerical Methods in Engineering*, 113(11):1697–1710, 2018.

[83] A. N. Kounadis, G. J. Papadopoulos, and D. M. Cotsovos. Overturning instability of a two-rigid block system under ground excitation. *ZAMM - Journal of Applied Mathematics and Mechanics / Zeitschrift für Angewandte Mathematik und Mechanik*, 92(7):536–557, 2012.

[84] T. Krause, A. Molotnikov, M. Carlesso, J. Rente, K. Rezwan, Y. Estrin, and D. Koch. Mechanical properties of topologically interlocked structures with elements produced by freeze gelation of ceramic slurries. *Advanced Engineering Materials*, 14(5):335–341, 2012.

[85] J. V. Lemos. Discrete element modelling of the seismic behaviour of stone masonry arches. *Computer Methods in Structural Masonry*, 4:220–227, 1998.

[86] M. P. Levy. The Georgia dome and beyond: Achieving lightweight-longspan structures. In *Spatial, lattice and tension structures: Proceedings of the IASS-ASCE International Symposium 1994; held in conjunction with the ASCE Structures Congress XII, April 24-28, 1994*, pages 560–562, 1994.

[87] Y. Li, X. Feng, Y. Cao, and H. Gao. A Monte Carlo form-finding method for large scale regular and irregular tensegrity structures. *International Journal of Solids and Structures*, 47(14):1888–1898, 2010.

[88] Y. Li, X. Feng, Y. Cao, and H. Gao. Constructing tensegrity structures from one-bar elementary cells. *Proceedings of the Royal Society A*, 46645–61, 2010.

[89] C. T. Lim, E. H. Zhou, and S. T. Quek. Mechanical models for living cells—A review. *Journal of Biomechanics*, 39(2):195–216, 2006.

[90] S. Lin, S. Xue, B. Li, and X. Feng. An oscillating dynamic model of collective cells in a monolayer. *Journal of the Mechanics and Physics of Solids*, 112: 650–666, 2018.

[91] P. R. Lipscombe and S. Pellegrino. Free rocking of prismatic blocks. *Journal of Engineering Mechanics*, 119(7):1387–1410, 1993.

[92] M. Liu, Q. Li, S. Huang, F. Shi, and F. Chen. Evaluation of wind effects on a large span retractable roof stadium by wind tunnel experiment and numerical simulation. *Journal of Wind Engineering and Industrial Aerodynamics*, 179: 39–57, 2018.

[93] Y. Liu, L. Zhang, B. Wang, G. Xu, and X. Feng. Why are isolated and collective cells greatly different in stiffness? *Journal of the Mechanics and Physics of Solids*, 147:104280, 2021.

[94] Y. Liu, Q. Bi, X. Yue, J. Wu, B. Yang, and Y. Li. A review on tensegrity structures-based robots. *Mechanism and Machine Theory*, 168:104571, 2022.

[95] P. B. Lourenço. Recent advances in masonry modelling: Micromodelling and homogenisation. *Multiscale Modeling in Solid Mechanics: Computational Approaches*, pages 251–294, 2010.

[96] P. B. Lourenço, J. G. Rots, and J. Blaauwendraad. Continuum model for masonry: Parameter estimation and validation. *Journal of Structural Engineering*, 124(6):642–652, 1998.

[97] T. Lu, Z. Zhou, P. Bordeenithikasem, N. Chung, D. F. Franco, J. E. Andrade, and C. Daraio. Role of friction and geometry in tuning the bending stiffness of topologically interlocking materials. *Extreme Mechanics Letters*, 71:102212, 2024.

[98] S. Ma, X. Yuan, and A. Samy. Shape optimization of a new tensegrity torus. *Mechanics Research Communications*, 100:103396, 2019.

[99] S. Ma, M. Chen, and R. E. Skelton. Tensegrity system dynamics based on finite element method. *Composite Structures*, 280:114838, 2022.

[100] R. B. Macedo, E. Andò, S. Joy, G. Viggiani, R. K. Pal, J. Parker, and J. E. Andrade. Unearthing real-time 3d ant tunneling mechanics. *Proceedings of the National Academy of Sciences*, 118(36):e2102267118, 2021.

[101] J. M. McCracken, B. R. Donovan, and T. J. White. Materials as machines. *Advanced Materials*, 32(20):1906564, 2020.

[102] J. Metzcar, Y. Wang, R. Heiland, and P. Macklin. A review of cell-based computational modeling in cancer biology. *JCO Clinical Cancer Informatics*, (3):1–13, 2019.

[103] S. M. Mijailovich, M. Kojic, M. Zivkovic, B. Fabry, and J. J. Fredberg. A finite element model of cell deformation during magnetic bead twisting. *Journal of Applied Physiology*, 93(4):1429–1436, 2002.

[104] M. Mirkhalaf, T. Zhou, and F. Barthelat. Simultaneous improvements of strength and toughness in topologically interlocked ceramics. *Proceedings of the National Academy of Sciences*, 115(37):9128–9133, 2018.

[105] A. Molotnikov, R. Gerbrand, O. Bouaziz, and Y. Estrin. Sandwich panels with a core segmented into topologically interlocked elements. *Advanced Engineering Materials*, 15(8):728–731, 2013.

[106] A. Molotnikov, R. Gerbrand, Y. Qi, G. P. Simon, and Y. Estrin. Design of responsive materials using topologically interlocked elements. *Smart Materials and Structures*, 24(2):025034, jan 2015.

[107] S. Mondal. Phase change materials for smart textiles—An overview. *Applied Thermal Engineering*, 28(11):1536–1550, 2008.

[108] F. Montel, M. Delarue, J. Elgeti, D. Vignjevic, G. Cappello, and J. Prost. Isotropic stress reduces cell proliferation in tumor spheroids. *New Journal of Physics*, 14(5):055008, may 2012. doi: 10.1088/1367-2630/14/5/055008.

[109] F. Monticone and A. Alu. Metamaterial, plasmonic and nanophotonic devices. *Reports on Progress in Physics*, 80(3):036401, 2017.

[110] J. J. Moreau. Some numerical methods in multibody dynamics: Application to granular materials. In *European Journal of Mechanics. A. Solids*, 1994.

[111] A. Munjiza and N. W. M. John. Mesh size sensitivity of the combined fem/dem fracture and fragmentation algorithms. *Engineering Fracture Mechanics*, 69(2):281–295, 2002.

[112] A. A. Munjiza. *The Combined Finite-Discrete Element Method*. John Wiley & Sons, 2004.

[113] B. A. Newcomb. Processing, structure, and properties of carbon fibers. *Composites Part A: Applied Science and Manufacturing*, 91:262–282, 2016.

[114] L. T. K. Nguyen and M. Keip. A data-driven approach to nonlinear elasticity. *Computers Structures*, 194:97–115, 2018.

[115] R. O'Hegarty and O. Kinnane. Review of precast concrete sandwich panels and their innovations. *Construction and Building Materials*, 233:117145, 2020.

[116] J. Ou, L. Yao, D. Tauber, J. Steimle, R. Niiyama, and H. Ishii. Jamsheets: Thin interfaces with tunable stiffness enabled by layer jamming. In *Proceedings of the 8th International Conference on Tangible, Embedded and Embodied Interaction*, page 65–72. Association for Computing Machinery, 2014.

[117] N. Jagiella D. Drasdo. P. van Liedekerke, M. Palm. Simulating tissue mechanics with agent based models: Concepts and perspectives. *Computational Particle Mechanics*, 2, 2015.

[118] E. Papa. A unilateral damage model for masonry based on a homogenisation procedure. *Mechanics of Cohesive-frictional Materials: An International Journal on Experiments, Modelling and Computation of Materials and Structures*, 1(4):349–366, 1996.

[119] C. Paul, F. J. Valero-Cuevas, and H. Lipson. Design and control of tensegrity robots for locomotion. *IEEE Transactions on Robotics*, 22(5):944–957, 2006.

[120] A. F. Pegoraro, P. Janmey, and D. A. Weitz. Mechanical properties of the cytoskeleton and cells. *Cold Spring Harbor Perspectives in Biology*, 9, 2017.

[121] S. Pellegrino. A class of tensegrity domes. *International Journal of Space Structures*, 7(2):127–142, 1992.

[122] S. Pellegrino. Structural computations with the singular value decomposition of the equilibrium matrix. *International Journal of Solids and Structures*, 30 (21):3025–3035, 1993.

[123] A. R. Ploszajski, R. Jackson, M. Ransley, and M. Miodownik. 4D printing of magnetically functionalized chainmail for exoskeletal biomedical applications. *MRS Advances*, 4(23):1361–1366, 2019.

[124] Y. Rahali, I. Goda, and J. Ganghoffer. Numerical identification of classical and nonclassical moduli of 3D woven textiles and analysis of scale effects. *Composite Structures*, 135:122–139, 2016.

[125] J. J. Rimoli and R. K. Pal. Mechanical response of 3-dimensional tensegrity lattices. *Composites Part B: Engineering*, 115:30–42, 2017.

[126] A. Rodriguez-Burneo, J. I. Restrepo, J. P. Conte, J. E. Andrade, A. Rosakis, V. Gabuchian, J. Harmon, A. Nema, and A. Pedretti. Seismic-response assessment of multiblock tower structures for energy storage: 1/25 scale. *Journal of Structural Engineering*, 150(5):04024040, 2024.

[127] A. J. Rosakis, J. E. Andrade, V. Gabuchian, J. M. Harmon, J. P. Conte, J. I. Restrepo, A. Rodriguez, A. Nema, and A. R. Pedretti. Implications of Buckingham's Pi theorem to the study of similitude in discrete structures: Introduction of the R_F^N, μ^N, and S^N dimensionless numbers and the concept of structural speed. *Journal of Applied Mechanics*, 88(9):091008, 2021.

[128] P. Cañadas S. Wendling and P. Chabrand. Toward a generalised tensegrity model describing the mechanical behaviour of the cytoskeleton structure. *Computer Methods in Biomechanics and Biomedical Engineering*, 6(1):45–52, 2003.

[129] Hossein Salahshoor and Michael Ortiz. Application of data-driven computing to patient-specific prediction of the viscoelastic response of human brain under transcranial ultrasound stimulation. *Biomechanics and Modeling in Mechanobiology*, pages 1–17, 2024.

[130] S. Schaare, A. V. Dyskin, Y. Estrin, S. Arndt, E. Pasternak, and A. Kanel-Belov. Point loading of assemblies of interlocked cube-shaped elements. *International Journal of Engineering Science*, 46(12):1228–1238, 2008.

[131] M. Schiavoni, E. Giordano, F. Roscini, and F. Clementi. Numerical assessment of interacting structural units on the seismic damage: A comparative analysis with different modeling approaches. *Applied Sciences*, 13(2), 2023.

[132] G. W. Schmid-Schönbein, K. L. Sung, H. Tözeren, R. Skalak, and S. Chien. Passive mechanical properties of human leukocytes. *Biophysical Journal*, 36, 1981.

[133] D. S. Shah, E. J. Yang, M. C. Yuen, E. C. Huang, and R. Kramer-Bottiglio. Jamming skins that control system rigidity from the surface. *Advanced Functional Materials*, 31(1):2006915, 2021. doi: https://doi.org/10.1002/adfm.202006915.

[134] H. W. Shenton. Criteria for initiation of slide, rock, and slide-rock rigid-body modes. *Journal of Engineering Mechanics*, 122(7):690–693, 1996.

[135] T. Siegmund, F. Barthelat, R. Cipra, E. Habtour, and J. Riddick. Manufacture and mechanics of topologically interlocked material assemblies. *Applied Mechanics Reviews*, 68(4):040803, 07 2016.

[136] A. Sinopoli. Dynamics and impact in a system with unilateral constraints the relevance of dry friction. *Meccanica*, 22:210–215, 1987.

[137] A. Sinopoli. Kinematic approach in the impact problem of rigid bodies. *Applied Mechanics Reviews*, 42(11S):S233–S244, 11 1989.

[138] A. Sinopoli and V. Sepe. Coupled motion in the dynamic analysis of a three block structure. *Applied Mechanics Reviews*, 46(11S):S185–S197, 11 1993.

[139] L. Sironi, M. Andreini, C. Colloca, M. Poehler, D. Bolognini, F. Dacarro, P. Lestuzzi, F. Dubois, Z. Zhou, and J. E. Andrade. Shaking table tests for seismic stability of stacked concrete blocks used for radiation shielding. *Engineering Structures*, 283:115895, 2023.

[140] R. E. Skelton and M. C. De Oliveira. *Tensegrity Systems*, volume 1. Springer, 2009.

[141] H. Smoljanović, N. Živaljić, and Ž. Nikolić. A combined finite-discrete element analysis of dry stone masonry structures. *Engineering Structures*, 52:89–100, 2013.

[142] P. D. Spanos and A. Koh. Rocking of rigid blocks due to harmonic shaking. *Journal of Engineering Mechanics*, 110(11):1627–1642, 1984.

[143] D. Stamenović. Effects of cytoskeletal prestress on cell rheological behavior. *Acta Biomaterialia*, 1(3):255–262, 2005.

[144] D. Stamenović and D. E. Ingber. Models of cytoskeletal mechanics of adherent cells. *Biomechanics and Modeling in Mechanobiology*, 1:95–108, 2002.

[145] S. C. Stiros. Monumental articulated ancient Greek and Roman columns and temples and earthquakes: Archaeological, historical, and engineering approaches. *Journal of Seismology*, 24(4):853–881, August 2020.

[146] M. Stoppa and A. Chiolerio. Wearable electronics and smart textiles: A critical review. *Sensors*, 14(7):11957–11992, 2014.

[147] W. J. Stronge. Rigid body collisions with friction. *Proceedings of the Royal Society of London. Series A: Mathematical and Physical Sciences*, 431(1881): 169–181, 1990.

[148] W. J. Stronge. Unraveling paradoxical theories for rigid body collisions. *Journal of Applied Mechanics*, 58(4):1049–1055, 12 1991.

[149] S. Sun, L. Zhang, X. Chen, and X. Feng. Biochemomechanical tensegrity model of cytoskeletons. *Journal of the Mechanics and Physics of Solids*, 175: 105288, 2023.

[150] *SIA 261 - Actions sur les structures porteuses*. Swiss Society of Engineers and Architects, 2020.

[151] A. G. Tibert and S. Pellegrino. Review of form-finding methods for tensegrity structures. *International Journal of Space Structures*, 18(4):209–223, 2003.

[152] G. Tibert. *Deployable tensegrity structures for space applications*. PhD thesis, KTH, 2002.

[153] I. M. Tolić-Nørrelykke, J. P. Butler, J. Chen, and N. Wang. Spatial and temporal traction response in human airway smooth muscle cells. *American Journal of Physiology-Cell Physiology*, 283(4):C1254–C1266, 2002.

[154] W. K. Tso and C. M. Wong. Steady state rocking response of rigid blocks part 1: Analysis. *Earthquake Engineering & Structural Dynamics*, 18(1): 89–106, 1989.

[155] Y. Tsuji, T. Kawaguchi, and T. Tanaka. Discrete particle simulation of two-dimensional fluidized bed. *Powder Technology*, 77(1):79–87, 1993.

[156] X. Tu and J. E. Andrade. Criteria for static equilibrium in particulate mechanics computations. *International Journal for Numerical Methods in Engineering*, 75(13):1581–1606, 2008. doi: https://doi.org/10.1002/nme.2322.

[157] S. Ullmann, D. S. Kammer, and S. Feldfogel. The deflection limit of slab-like topologically interlocked structures. *Journal of Applied Mechanics*, 91(2): 021004, 10 2023.

[158] J. Ulloa, A. Gorgogianni, K. Karapiperis, M. Ortiz, and J. E. Andrade. Data-driven breakage mechanics: Predicting the evolution of particle-size distribution in granular media. *Journal of the Mechanics and Physics of Solids*, 178:105328, 2023.

[159] J. Ulloa, L. Stainier, M. Ortiz, and J. E. Andrade. Data-driven micromorphic mechanics for materials with strain localization. *Computer Methods in Applied Mechanics and Engineering*, 429:117180, 2024.

[160] A. M. J. Valencia, P. Wu, O. N. Yogurtcu, P. Rao, J. DiGiacomo, I. Godet, L. He, M. Lee, D. Gilkes, S. X. Sun, and D. Wirtz. Collective cancer cell invasion induced by coordinated contractile stresses. *Oncotarget*, 6(41): 43438–43451, 2015.

[161] V. Venzal, S. Morel, T. Parent, and F. Dubois. Frictional cohesive zone model for quasi-brittle fracture: Mixed-mode and coupling between cohesive and frictional behaviors. *International Journal of Solids and Structures*, 198: 17–30, 2020.

[162] N. Veuve, A. C. Sychterz, and I. Smith. Adaptive control of a deployable tensegrity structure. *Engineering Structures*, 152:14–23, 2017.

[163] M. Vořechovský and D. Novák. Correlation control in small-sample monte carlo type simulations I: A simulated annealing approach. *Probabilistic Engineering Mechanics*, 24(3):452–462, 2009.

[164] B. Wang, J. Zhu, S. Zhong, W. Liang, and C. Guan. Space deployable mechanics: A review of structures and smart driving. *Materials Design*, 237:112557, 2024.

[165] H. Wang, J. T. Hang, Z. Chang, and G Xu. Static and dynamic mechanics of cell monolayers: A multi-scale structural model. *Acta Mechanica Sinica*, 38, 2022.

[166] L. Wang, Y. Yang, Y. Chen, C. Majidi, F. Iida, E. Askounis, and Q. Pei. Controllable and reversible tuning of material rigidity for robot applications. *Materials Today*, 21(5):563–576, 2018.

[167] N. Wang, J. P. Butler, and D. E. Ingber. Mechanotransduction across the cell surface and through the cytoskeleton. *Science*, 260(5111):1124–1127, 1993.

[168] N. Wang, K. Naruse, D. Stamenović, J. J. Fredberg, S. M. Mijailovich, I. M. Tolić-Nørrelykke, T. Polte, R. Mannix, and D. E. Ingber. Mechanical behavior in living cells consistent with the tensegrity model. *Proceedings of the National Academy of Sciences*, 98(14):7765–7770, 2001.

[169] N. Wang, I. M. Tolić-Nørrelykke, J. Chen, S. M. Mijailovich, J. P. Butler, J. J. Fredberg, and D. Stamenović. Cell prestress. I. Stiffness and prestress

are closely associated in adherent contractile cells. *American Journal of Physiology-Cell Physiology*, 282(3):C606–C616, 2002.

[170] Y. Wang, L. Li, D. Hofmann, J. E. Andrade, and C. Daraio. Structured fabrics with tunable mechanical properties. *Nature*, 596(7871):238–243, 2021.

[171] M. Weizmann, O. Amir, and Y. J. Grobman. Topological interlocking in buildings: A case for the design and construction of floors. *Automation in Construction*, 72:18–25, 2016.

[172] A. Williams and T. Siegmund. Mechanics of topologically interlocked material systems under point load: Archimedean and laves tiling. *International Journal of Mechanical Sciences*, 190:106016, 2021.

[173] W. Xi, T. B. Saw, D. Delacour, C. T. Lim, and B. Ladoux. Material approaches to active tissue mechanics. *Nature Reviews Materials*, 4:23–44, 2019.

[174] X. Xia, A. Afshar, H. Yang, C. M. Portela, D. M. Kochmann, C. V. Di Leo, and J. R. Greer. Electrochemically reconfigurable architected materials. *Nature*, 573(7773):205–213, 2019.

[175] X. Yang, Z. Wang, B. Zhang, T. Chen, C. Linghu, K. Wu, G. Wang, H. Wang, and Y. Wang. Self-sensing robotic structures from architectured particle assemblies. *Advanced Intelligent Systems*, 5(1):2200250, 2023.

[176] A. Yeung and E. Evans. Cortical shell-liquid core model for passive flow of liquid-like spherical cells into micropipets. *Biophysical Journal*, 56, 1989.

[177] J. Zhang and M. Ohsaki. *Tensegrity Structures: Form, Stability, and Symmetry*, volume 7. Springer, 2015.

[178] L. Zhang, M. K. Lu, H. W. Zhang, and B. Yan. Geometrically nonlinear elastoplastic analysis of clustered tensegrity based on the co-rotational approach. *International Journal of Mechanical Sciences*, 93:154–165, 2015.

[179] E. H. Zhou, X. Trepat, C. Y. Park, G. Lenormand, M. N. Oliver, S. M. Mijailovich, C. Hardin, D. A. Weitz, J. P. Butler, and J. J. Fredberg. Universal behavior of the osmotically compressed cell and its analogy to the colloidal glass transition. *Proceedings of the National Academy of Sciences*, 106(26): 10632–10637, 2009.

[180] Z. Zhou, M. Andreini, L. Sironi, P. Lestuzzi, E. Andò, F. Dubois, D. Bolognini, F. Dacarro, and J. E. Andrade. Discrete structural systems modeling: Benchmarking of ls-dem and lmgc90 with seismic experiments. *Journal of Engineering Mechanics*, 149(12):04023097, 2023.

[181] C. Zhu, G. Bao, and N. Wang. Cell mechanics: Mechanical response, cell adhesion, and molecular deformation. *Annual Review of Biomedical Engineering*, 2:189–226, 2000.